EXCESS THERMODYNAMIC PROPERTIES
AND SIZE-DEPENDENT SEGREGATION PHENOMENA
IN ULTRAFINE-GRAINED TITANIUM DIOXIDE

by

Chrysanthe D. Terwilliger

B.S. Mechanical Engineering, Worcester Polytechnic Institute
(1988)

Submitted to the Department of Materials Science and Engineering
in Partial Fulfillment of the Requirements for the Degree of

DOCTOR OF PHILOSOPHY
in Ceramics

at the

Massachusetts Institute of Technology

September 1993

©1993 Massachusetts Institute of Technology

Signature of Author _____

Department of Materials Science and Engineering
August 6, 1993

Certified by _____

Yet-Ming Chiang
Kyocera Associate Professor of Ceramics
Thesis Supervisor

Accepted by _____

Carl V. Thompson II
Professor of Electronic Materials
Chair, Departmental Committee on Graduate Students

EXCESS THERMODYNAMIC PROPERTIES
AND SIZE-DEPENDENT SEGREGATION PHENOMENA
IN ULTRAFINE-GRAINED TITANIUM DIOXIDE

by

CHRYSANTHE D. TERWILLIGER

Submitted to the Department of Materials Science and Engineering
on August 6, 1993 in partial fulfillment of the requirements
for the Degree of Doctor of Philosophy in Ceramics

ABSTRACT

This work has two primary goals. The first is to advance our fundamental understanding of grain boundaries by making direct measurements of grain boundary thermodynamic properties using ultrafine-grained materials. The second is to explore possible deviations from conventional behavior at ultrafine grain sizes, specifically in regards to grain boundary thermodynamic properties and solute segregation to grain boundaries.

The first direct measurements of grain boundary thermodynamic properties in an oxide have been made. The excess enthalpy and excess heat capacity of grain boundaries in TiO_2 were measured by the calorimetric monitoring of grain growth in samples with an initial mean grain size of 30-70 nm. These samples contain a sufficiently large amount of grain boundary area such that the heat release upon grain growth can be measured accurately by commercial calorimeters. High density, fully oxygenated, phase-pure rutile (TiO_2) with a mean grain size <50 nm was prepared by a chemical method and was found to be more appropriate for these measurements than highly defective fine-grained TiO_{2-x} prepared by the inert gas condensation process.

Results show a clear temperature and/or grain size dependence of the excess grain boundary enthalpy of TiO_2. The specific grain boundary enthalpy, H_{gb}, increases from ~ 0.5-1 J/m^2 at low temperatures and very fine grain sizes (600-780°C, ~ 30-200 nm) to a value of ~ 1.3-1.7 J/m^2 averaged over a much larger temperature and size range (600-1300°C, 30 nm-2μm). Size and temperature effects on H_{gb} are inextricable. Additional evidence of a temperature- or size-dependent H_{gb} is obtained from measurements of the excess heat capacity of ultrafine-grained samples. The trend in H_{gb} is not due to experimental artifacts; extraneous contributions from heat-dissipating processes other than grain growth, including the anatase-rutile phase transformation, sintering, and relief of lattice strain, are shown to be negligible.

It is proposed that the most plausible explanation for a specific grain boundary enthalpy that increases with temperature or grain size is a size-dependent nonstoichiometry of rutile due to the impingement of space charge layers in the grain size and temperature range of the experiments. Debye lengths of 165 nm and 33 nm are estimated for intrinsic, slightly reduced TiO_2 at 800° and 1000°C, respectively.

Direct measurements have been made of size-dependent solute segregation at fine grain sizes. TiO_2 powder was doped with 0.34 mole% Ca, and samples ranging in grain size from 50 nm to ~0.75 μm were prepared. Using a STEM microanalysis technique to quantify the grain boundary coverage of calcium, segregation below grain sizes of 200-400 nm was found to deviate from conventional segregation isotherms, exhibiting a clear size dependence. Below this threshold grain size, there is an excess of boundary sites relative to the supply of solute, and the lattice is almost entirely depopulated of solute. In the present material system, boundaries were found to become saturated with calcium when the coverage reached approximately one half of an equivalent monolayer.

These experimental results are modeled with a statistical thermodynamical treatment of segregation which takes into account the large density of grain boundary sites in this size range (Colbourn et al, 1983). The threshold grain size, below which segregation is size-dependent, is calculated as a function of the heat of segregation, temperature, doping level, and saturation coverage.

The measurements of Ca segregation, along with observations of $CaTiO_3$ precipitates upon coarsening, support a mechanism of equilibrium enhancement of total solid solubility due to grain boundary segregation. A weakly temperature-dependent total solid solubility of ~1 mole% Ca in TiO_2 with a mean grain size of 50 nm is estimated using the observed segregation behavior.

Calcium was observed to be an effective grain growth inhibitor in ultrafine-grained TiO_2. The present samples, both with and without calcium additions, show more resistance to grain growth than other ultrafine-grained TiO_2 reported to date. The effective activation energy for grain growth indicated by a Kissinger analysis of grain growth exotherms is 1.3-1.5 eV in both Ca-doped and Ca-free samples. The observed effect of calcium on grain growth exotherms is discussed in light of the size-dependent segregation behavior in these samples.

Thesis Supervisor: Professor Yet-Ming Chiang
                Title: Kyocera Associate Professor of Ceramics

3

TABLE OF CONTENTS

LIST OF FIGURES

7

LIST OF TABLES

ACKNOWLEDGEMENTS

Only partially due to the euphoria of finishing, I look upon my thesis and my time at MIT as a very positive experience that would not have been possible without the support of many people.

First I thank my advisor, Professor Yet-Ming Chiang, for his guidance and enthusiasm throughout this work, for many useful discussions, and for aiding my professional development. I have learned a tremendous amount from him about scientific inquiry and communication that will surely benefit me in my future career. I would also like to acknowledge Professors Robert Balluffi, Carl Thompson, and John Vander Sande, all of whom served on my thesis committee and gave valuable suggestions on improving the final document.

Many thanks to Fred Wilson and Pat Kearney for their help in solving problems around the lab and for their perpetual good nature. I am especially grateful to Mike Frongillo for his advice on transmission electron microscopy, for being a willing and able ion mill maintenance consultant, and for many animated and humorous conversations.

Special thanks to Drs. Sharon Furcone, Jeri Ikeda, Trish Smyth, and Bob Messner, former graduate students in our research group who sacrificed a lot of their time getting me started in the lab early in my graduate career and with whom I've had many useful discussions. More recently, Dr. Leszek Hozer has been so helpful in assisting me with stubborn equipment and software and for keeping a smile on my face most of the time. I am also grateful to Toni Centorino for her help in dealing with all the red tape at MIT. Thanks also to Beth Opila and Hal Kahn, friends and rotisserie baseball aficionados, for sharing with me that wonderful diversion from science during the last several years.

I thank Professor Jackie Ying and Ken Bryden in Chemical Engineering for use of their TGA, and Dr. Jeffrey Eastman at Argonne National Laboratory who supplied us with some nanocrystalline TiO_2 powder in the early stages of this project. I am most grateful to Dr. Howard Jacobsen of E.I. DuPont de Nemours, whose suggestion to use Sn to promote formation of rutile was the critical experimental breakthrough in this work.

I would also like to acknowledge the Materials Processing Center and its Summer Research Scholar program which enabled me to spend a summer at MIT after my junior year as an undergraduate. Thanks especially to Dr. Wendell Rhine who made that first experience at MIT and with ceramics research so rewarding.

Most of all, I thank my family. I cannot express fully my gratitude for the love, friendship, and incredible patience of my husband Peter. He made many sacrifices during our first four years of marriage that allowed me to complete this Ph.D. to the best of my abilities. I owe so much to my parents, Sally and Jim Demetry, who provided me with a stable and loving home and, by their own example, instilled in me a pride in achievement. I somehow inherited both of their loves for teaching, and my father continues to be my #1 mentor in engineering education. My sisters Athena and Sara have always been supportive, and our family gatherings were a primary source of joy and sustenance during the last five years. Thanks also to Ed, and of course, to Sasha.

12

Written and dedicated in loving memory of my mother

Sally Ann Weidlein Demetry

June 11, 1938 - January 26, 1993

Make the moment vital and worth living.

Do not let it slip away unnoticed and unused.

-- Martha Graham

ORGANIZATION OF THESIS

This research divides rather readily into subtopics, and as such, this document is a combination of three manuscripts that have been prepared for publication in refereed journals. Chapters 2 and 3 describe the measurements of excess thermodynamic properties of grain boundaries in TiO_2. Chapter 4 describes the investigation of size-dependent solute segregation phenomena, and Chapter 5 contains results and discussion of grain growth inhibition in ultrafine-grained TiO_2 due to solute additions. Each of these chapters contains its own introduction and summary. Wherever possible, redundancies between the chapters have been eliminated. Sample preparation and TEM characterization of grain size and grain boundary area are described fully only in Chapter 2, and a full description of the STEM microanalysis technique is contained only in Chapter 4. An overall introduction, conclusions, and suggestions for future work are contained in Chapters 1, 6, and 7 and encompass all topics.

CHAPTER 1

BACKGROUND AND RESEARCH OBJECTIVES

This work is based on the proposition that by studying ultrafine-grained materials we can advance our understanding of the fundamental properties of grain boundaries. The measurement of grain boundary properties has traditionally been limited by the need for extremely high resolution methods. But as grain size decreases and the volume fraction of interfaces increases, grain boundary properties begin to contribute significantly to the macroscopic properties of a material and reach a magnitude that is within the sensitivity of many experimental techniques. In particular, a primary objective of this work was to exploit the high density of grain boundary area in an ultrafine-grained material to make measurements of grain boundary thermodynamic properties.

Among the fundamental properties of grain boundaries, excess thermodynamic properties are less studied than chemistry and structure, and are difficult to measure experimentally. Furthermore, while experimental and theoretical studies have provided some insight into structure-energy relations of special, short-period grain boundaries in metals and oxides,[1-11] knowledge about the general, high angle boundaries that are more relevant to most technological applications is decidedly lacking.[12,13] Particularly for oxides, the computational task of modeling a general high angle grain boundary at finite temperatures is exceedingly difficult, and experimental work has focused almost exclusively on the measurement of dihedral angles, which are only an indirect indication of grain boundary tension relative to that of a free surface.

In contrast with dihedral angle measurements, the calorimetric measurement of grain boundary properties is direct and absolute; since the driving force for grain growth is the elimination of grain boundary area, the heat released during grain

growth is a direct measure of the enthalpy of the average grain boundary. While the enthalpy release upon grain growth of a coarse polycrystal is so small that its measurement is impracticable, for ultrafine-grained materials the total heat release is within the sensitivity of commercial calorimeters. In addition, an excess heat capacity of ultrafine-grained materials can be measured which, in concept, enables calculation of grain boundary entropy and the temperature dependence of the grain boundary enthalpy. Thus, a unique feature of the calorimetric measurement of grain boundary thermodynamic properties is the ability to measure independently the enthalpic and entropic contributions to the grain boundary free energy.

The accuracy of calorimetric measurements of grain boundary thermodynamic properties is entirely dependent on the appropriateness of the material for these measurements. Many other heat-dissipating processes can occur simultaneously with grain growth and are thus a potential source of artifacts in the measurements. For example, measurements of the excess enthalpy and excess heat capacity of grain boundaries in ultrafine-grained metals have been complicated by large lattice strain energies, sintering, and adsorbed gases. Therefore, this work was initially centered on an iterative process of sample preparation and characterization, until it could be shown that contributions from extraneous heat-dissipating processes were negligible relative to the excess heat from grain boundaries.

TiO_2 (rutile) was the material used throughout this work, and a brief note about the reasons for and the implications of its selection is appropriate. Initially, preparation of fine-grained Si and MgO thick films was attempted using electron beam evaporation. These are more simple, model material systems, but they were not pursued because of processing difficulties and very small DSC signals due to

low sample mass. In comparison, synthesis of appropriate ultrafine-grained TiO_2 samples was more readily accomplished, but TiO_2 is a more complex model system. For example, in any ionic system there exists the possibility of space charge formation at grain boundaries.[14,15] If the formation energies of oppositely charged defects at grain boundaries are not equal, grain boundaries have a net charge which is compensated by the formation of a space charge layer adjacent to the boundary, enriched in oppositely charged defects from the bulk to maintain overall electroneutrality. Another dimension of complexity in TiO_2 is due to its intrinsic nonstoichiometry (TiO_{2-x}),[16] most pronounced at high temperatures and low oxygen partial pressures, the source of which is the dual valence states of the titanium ion (Ti^{4+}, Ti^{3+}). In addition, a long-standing controversy in studies of the defect chemistry of rutile has been whether Schottky or Frenkel defect pairs predominate;[16,17] which of the two is energetically favored determines whether negatively charged defects are compensated by oxygen vacancies ($V_O^{\cdot\cdot}$) or titanium interstitials ($Ti_i^{\cdot\cdot\cdot\cdot}$). The introduction of aliovalent solutes further complicates the defect equilibria, and mixed ionic and electronic compensation of defects may occur. Thus, the complexity of grain boundaries in TiO_2 is clear; this is both a challenge during interpretation of our grain boundary thermodynamic property measurements and an opportunity to use these measurements to learn more about grain boundaries in this complicated yet technologically important ionic system.

Associated with the use of ultrafine-grained materials to study grain boundary properties is the possibility that these properties are distinct from those in conventional coarse-grained materials. Such claims have been common in the recent flurry of activity in nanocrystalline materials research. Thus, an additional objective of this work was to explore possible deviations from conventional behavior

at ultrafine grain sizes. Specifically, the effect on the grain boundary enthalpy of impinging space charge layers at fine grain sizes is hypothesized, and solute segregation at fine grain sizes is investigated.

Several theoretical studies have predicted a deviation from conventional solute segregation isotherms[18,19] and an enhanced total solid solubility[20] as grain size decreases. This departure from conventional behavior can be attributed simply to the very large number of grain boundary sites at ultrafine grain sizes rather than to a unique "nanocrystalline" behavior. To the best of our knowledge, these predictions had never been quantified experimentally, and preparation of Ca-doped fine-grained TiO_2 along with the use of a recently de.eloped, highly quantitative STEM microanalysis technique has allowed us to do so.

A secondary objective of this work was to evaluate the effectiveness of solute segregation as a means of inhibiting grain growth at very fine grain sizes; extending the stability of nanostructures to higher temperatures is believed to be critical if these materials are to be used in widespread technological applications.[21,22] The grain growth exotherms of ultrafine-grained Ca-doped and Ca-free TiO_2 are compared and analyzed using methods developed by Chen and Spaepen[23] to give some information about the kinetics of grain growth. We then seek to make correlations between the characteristics of the grain growth exotherms and the size-dependent segregation behavior that was observed by STEM.

The final import of this research is twofold. The first direct measurements of the excess thermodynamic properties of general, high angle grain boundaries in a complex, nonstoichiometric oxide have been made and should be of interest to those studying the fundamental science of grain boundaries. In addition, these measurements of grain boundary thermodynamic properties and characterization of

solute segregation and resulting grain growth inhibition at ultrafine grain sizes are of paramount importance to researchers working on the control of thermal stability, microstructural development, and properties of nanocrystalline materials.

CHAPTER 2

MEASUREMENTS OF THE EXCESS ENTHALPY OF
GRAIN BOUNDARIES USING ULTRAFINE-GRAINED TiO$_2$

2.1 INTRODUCTION

The direct calorimetric measurement of specific grain boundary enthalpy appears to have been first attempted in the 1950's by Åström,[1] who used metals with grain sizes of 100 μm or more. The accuracy of this technique is greatly improved by the use of ultrafine-grained materials (10-100 nm), which have a grain boundary area per unit volume that is three to four orders of magnitude larger than Åström's. The tremendous amount of grain boundary area also makes these measurements feasible using commercial calorimeters. Chen and Spaepen seemed to revive interest in this technique several years ago when they used calorimetry as a means of differentiating between nucleation and growth and grain growth processes[2] and demonstrated that the grain growth exotherm can be analyzed to give information about the kinetics of grain growth.[3]

Despite the apparent simplicity and elegance of this approach, in practice the calorimetric measurement of grain boundary thermodynamic properties is not trivial, in large part due to heat release from processes that occur simultaneously with grain growth. Most calorimetric studies of nanocrystalline metals and alloys have measured a combination of grain boundary energy and lattice strain energy[4-6] or have been complicated by the presence of multiple phases.[7] Furthermore, many of these studies have used samples that are less that 90% of bulk theoretical density, and thus the excess enthalpy is likely to be a combination of grain boundary and surface energies. After attempting to subtract contributions from lattice strain, researchers have reported specific grain boundary energies that are sometimes typical of[4,6] and in other cases much greater than[5] their coarse-grained counterparts.

20

Although these studies have provided useful information about total excess properties and the thermal stability of nanocrystalline metals and alloys, most "grain boundary" enthalpies derived from them cannot be interpreted unambiguously because of the likelihood of other contributions. In order to make absolute measurements of grain boundary properties, these artifacts must be eliminated.

Compared with the calorimetric studies of metals just cited, the work on ultrafine-grained TiO_2 described herein more closely approaches unadulterated grain growth and thus is a more accurate measurement of specific grain boundary enthalpy, the first such measurement in an oxide. Special attention has been given to sample preparation and thorough characterization to eliminate potential artifacts. It is shown that extraneous heat dissipation from the anatase-rutile phase transformation, sintering, and relief of lattice strain is negligible relative to the excess heat of grain boundaries. The measurements clearly indicate a temperature or grain size dependence of the specific grain boundary enthalpy (H_{gb}, J/m^2). Possible origins of this trend are discussed, including solute segregation, an intrinsic dependence of boundary structure and energy on temperature or grain size, and grain boundary triple junctions. However, the most plausible explanation is shown to be a size-dependent nonstoichiometry of TiO_2 due to impinging space charge layers in high purity materials at very fine grain sizes.

2.2 EXPERIMENTAL METHODS

2.2.1 Sample Preparation

Nanocrystalline TiO_2 powder made by the inert gas condensation process was provided to us by J.A. Eastman at Argonne National Laboratory, and some was also obtained from a commercial source.[*] Details of this process are best described

---

[*] Nanophase Technologies Corporation, Darien, IL

by others,[8,9] but a brief outline will be given here. Titanium metal is evaporated, using either Joule-heating or an electron beam, into a high vacuum chamber backfilled with an inert gas, usually helium, to a pressure of several hundred Pa. Titanium clusters collide with gas molecules, condense, and are carried either by natural convection or forced gas flow to a collection point, typically a rotating liquid nitrogen cold finger. The chamber is then evacuated and oxygen is introduced. The oxidized clusters are then scraped off the cold finger and collected. Subsequent anneals in oxygen are sometimes used to oxidize the powder further.

Ultrafine TiO_2 powder was also synthesized in our own laboratory using a solution-chemical process. High purity (99.999%) $TiCl_4$ and $SnCl_4$* were added in the desired proportions to deionized water initially at 0°C. The addition of tin at a level equivalent to ~1.1 mole% SnO_2 accelerates the anatase-to-rutile phase transformation such that phase-pure rutile is obtained while retaining a primary crystallite size on the order of 20 nm. (Details about the effect of dopants and processing methodology on the anatase-rutile phase transformation are contained in Appendix B.) The aqueous solutions of chlorides were co-precipitated by adding 7.4 M reagent-grade ammonium hydroxide under rapid stirring. The precipitate/water mixture was given at least five washing cycles consisting of stirring, sedimentation, decantation of supernatant, and dilution with deionized water. The mixture was then sprayed into liquid nitrogen and freeze-dried.** Powders were calcined in air on platinum foil for one hour at temperatures between 550-600°C. Chemical analysis of calcined powders was accomplished using inductively-coupled plasma emission spectroscopy (ICP),*** the results of which are shown in Table II-1. The starting titanium tetrachloride and titanium metal are

---

* All chemicals from Johnson-Matthey, Alfa Chemicals, Ward Hill, MA
** Virtis Co., Gardiner, NY
*** Union Carbide Corp., Tarrytown, NY

TABLE II-1. Chemical analysis of chemically-derived and inert gas- condensed ultrafine TiO_2 powders, as measured by inductively-coupled plasma emission spectroscopy.

Powder Batch	Mole% Sn	Si	Cl[†]	Other (ppm)
S1	0.56	0.10	N.A.	B(370)
S2	1.15	0.38	32 ppm	--
S3	1.07	0.37	258 ppm	--
ANL	54 ppm	0.58	N.A.	Al(888), Fe(153), Ca(54)

†Measured by ion chromatography.
N.A.=not analyzed
ANL=inert gas-condensed powder produced at Argonne National Laboratory

probably the sources of minor silicon impurity that is present; alternatively, it could be an artifact of the ICP measurement. The only other impurity detected in the chemically-derived powders was <260 ppm of residual chlorine and a small amount of boron in one of the batches.

Powders were hot pressed in air inside a WC/Co die[*] into ~5 mm diameter pellets. The temperature outside the die was maintained at 700°C; inside the die the temperature was estimated to be 600-625°C at steady state. To achieve bulk densities ≥95% of the theoretical value, a pressure of ~400-700 MPa and pressing times of 2-4 hours were sufficient for chemically-derived powders; inert gas-condensed powders required 1.1-1.3 GPa and 6-10 hours to reach a similar density. Following removal from the die, pellet surfaces were ground to remove a thin discolored layer from die contamination. Pellets were then annealed in air for 24 hours at 500°C. The mean grain size after this treatment was generally on the order of 35-50 nm, and samples were phase-pure rutile by x-ray diffraction.

---

* Southern Carbide Die Co., Oak Park, MI

2.2.2 Differential Scanning Calorimetry

All of the calorimetry was conducted using a Netzsch DSC 404,[*] which operates up to 1400°C with a stable baseline due to the temperature uniformity of its platinum-wound furnace. This instrument measures the temperature difference between a sample and a reference (given by a voltage difference, ΔV, between thermocouples), which upon calibration can be converted to heat flow (mW), thus enabling quantitative measurements of enthalpy and heat capacity. A calibration begins with measurement of the baseline, which is the temperature difference between the sample and reference platforms, each containing an empty platinum crucible with lid. A synthetic sapphire disk of known heat capacity[**] is then placed in the sample crucible, and the run is repeated under identical conditions of heating rate and atmosphere, which in all cases was compressed air flowing at 20 cc/min. The heat flow $\dot{H}$ (mW) into this inert sample of known heat capacity at temperature T is calculated as:

$$\dot{H}(T) = C_P(T) \cdot \text{mass} \cdot \alpha \qquad (2\text{-}1)$$

where α is the heating rate (Ks^{-1}). The ΔV signal of the baseline run is subtracted from that of the sapphire run, and a "sensitivity" (a calibration constant) in $\mu V/mW$ is computed as a continuous function of temperature. (A more common but less accurate calibration procedure is to compare measured and known heats of fusion of two or three different metals, and then assume a linear interpolation and/or extrapolation over the entire temperature range of interest.) The sensitivity of the instrument decreases non-linearly from a value slightly less than 1 $\mu V/mW$ at room temperature to ~0.3 $\mu V/mW$ at 1300°C; the sensitivity-temperature function is highly reproducible and is independent of heating rate. The temperature difference

---

[*] Netzsch, Inc., Pickering, PA
[**] National Institute of Standards and Technology, Standard Reference Material 720.

in μV between an unknown sample and the reference can then be converted to heat flow in mW by dividing by the sensitivity at each increment in temperature.

Each measurement of the heat flow during grain growth of an ultrafine-grained TiO_2 sample proceeded as follows. A piece of the pellet was cut and reserved for TEM observation of the as-prepared microstructure. The remaining sample was rinsed successively in acetone, methanol, and deionized water, then dried and weighed on a microbalance which was regularly calibrated. A typical sample mass for calorimetry was 50-100 mg. After a calibration of the DSC was completed, the sample was given a "cleaning run" to 500°C to remove any surface residue. (There is insignificant grain coarsening during this step since samples were previously annealed at 500°C for 24 hrs. following hot pressing.) To measure the enthalpy release during grain growth, both "scanning" and "isothermal" runs were conducted. Scanning runs were conducted at heating rates of 10-40°/min to 1300°C, and thus result in a specific enthalpy (J/m^2) averaged over that temperature and grain size range. "Isothermal" experiments were accomplished by scanning at 20°/min to the temperature of interest (generally 650-800°C) and holding for 30 minutes. These measurements thus give an excess enthalpy averaged over a much smaller temperature and grain size range. After completion of the first run (either scanning or isothermal) a second run was made under identical conditions, without lifting the furnace or disturbing the sample, to serve as a baseline. Selected experiments showed no detectable change in baseline upon conducting a third run, indicating that no detectable thermal changes occurred after the first measurement. The calorimetric signal in mW of the second run (coarsened, inert sample) was subtracted from that of the first run (nanocrystalline sample undergoing grain growth), and the resulting exotherm was integrated to give a total enthalpy release, ΔH_{tot}, in J/g. The specific grain boundary enthalpy (J/m^2) is then $H_{gb} = \Delta H_{tot}/\Delta S_V$

where ΔS_V is the change in grain boundary area, the measurement of which is discussed in the next section.

2.2.3 Determination of Grain Size and Grain Boundary Area by TEM

An accurate determination of the change in grain boundary area upon coarsening is critical to the conversion of total excess enthalpy (J/g) to specific grain boundary enthalpy (J/m^2). Since the grain boundary area per unit volume (S_V) decreases by almost two orders of magnitude during some of our DSC measurements, the accurate measurement of S_V for the as-prepared ultrafine-grained structure is particularly important. One means of measuring S_V is the well-known "linear intercept method," $S_V = 2 \cdot P_L$, where P_L is the number of grain boundary intersections per unit length of test line.[10,11] This method is attractive in that no assumptions about grain shape or size distribution are necessary, but it is applicable only to a two-dimensional surface, which is quite difficult to prepare and observe for a sample with grain size < 100 nm. When the grain size is less than the TEM foil thickness, TEM images are projections of a volume of material, and the linear intercept method would overestimate S_V since the true length of the test line would be greater than assumed. (The test line in reality would zig-zag through the foil thickness.) Thus, an alternative method for determining S_V which uses the mean value of maximum grain dimensions was applied since it is more accurate at very fine grain sizes.

The average grain size and total grain boundary area of as-prepared and coarsened samples were obtained directly from TEM micrographs. Samples were prepared by mechanically thinning a small piece of the pellet to a thickness of $\sim 25 \mu m$, followed by cold-stage ion thinning using Ar^+ ions with a 5-6 kV accelerating voltage. The microscopy was conducted in bright-field mode using a JEOL 200CX, and fifteen to twenty micrographs were taken at random from the

26

thinned area of each sample. TEM negatives were enlarged onto a point grid, and the maximum projected dimension of the grain at each grid point was measured; at least five hundred grains in each sample were measured.

Two criteria must be satisfied in order to equate the maximum projected dimension of a grain with its maximum dimension. First, the grains must be equiaxed; we found this to be the case from TEM observations. Second, the grains must be contained in their entirety within the TEM foil. This assumption is reasonable when the grain size is much less than the foil thickness and a number of grains can be seen overlapping through the foil, as was the case in our as-prepared samples. (At the finest grain sizes, three grains were often seen through the cross section of the foil, decreasing to two in coarser-grained samples, which suggests a foil thickness range of $\sim$120-500 nm.) In the post-scan (1300°C) microstructures, the maximum projected dimension of grains is typically 1-4 μm, larger than the foil thickness, in which case the grains are truncated and the maximum projected dimension underestimates the maximum grain dimension. However, since the change in grain boundary area is insensitive to the final grain size, no further corrections were made. (For example, a final grain size of 10μm rather than 1μm causes <2.5% difference in the change in boundary area when the initial grain size is 35 nm.) The grain size range between 100-500 nm is an awkward area in which neither the use of projected dimensions or the linear intercept method is entirely appropriate; both tend to underestimate grain size and overestimate S_V when the critical assumptions begin to fail. As a test, both methods were used on a sample with a mean grain size of $\sim$500 nm, and the linear intercept method indicated an S_V $\sim$30% greater than that calculated using projected dimensions. Thus, even at this larger grain size the projected dimension method appears to overestimate S_V by less than the linear intercept method.

The calculation of grain boundary area using the mean maximum dimension, $\overline{D}$, requires knowledge of the grain shape. We have assumed regular tetrakaidecahedra, for which the surface-to-volume ratio is $S_V = 2.3675/L$, where L is the edge length.[11] If one examines possible projections of a tetrakaidecahedron, the largest projected dimension lies in the range 2.8L-3.2L. Indeed, the statistical average for randomly-oriented tetrakaidecahedra is 3.0L.[11] Therefore, the surface-to-volume ratio of a single tetrakaidecahedron expressed in terms of its largest projected dimension, D, is 7.1025/D. For identical contiguous tetrakaidecahedral grains, the grain boundary area per unit volume is $S_V = 3.5513/D$ since each interface is shared by two grains.

This estimation of grain boundary area can be made more accurate if one accounts for a size distribution about the mean. By plotting cumulative probability versus normalized grain size on a log scale (see Fig. 2.3), our samples were found to have lognormal grain size distributions. A correction in surface-to-volume ratios to account for a lognormal distribution rather than identical-sized grains has been evaluated previously[12] to be $\exp\left[-2.5(\ln \sigma)^2\right]$, where $\ln \sigma$ is the standard deviation of normalized grain sizes $\ln(D / \overline{D})$. Thus, the grain boundary area per unit volume was calculated from the expression:

$$S_V = \frac{\text{grain boundary area}}{\text{total volume}} = \frac{3.5513}{\overline{D}} \exp\left[-2.5(\ln \sigma)^2\right]. \qquad (2\text{-}2)$$

It should be noted that the approach just outlined is not entirely self-consistent in that it assumes all grains to have a single geometrical shape yet allows a size distribution, which strictly speaking would preclude space-filling. In a recent review,[13] Atkinson has pointed out that this paradox is implicit in most theories of normal grain growth (for example, those due to Feltham, Wagner-Hillert, Louat.)

28

Despite the topological inconsistency, inclusion of a correction for size distribution about the mean was judged to be important for accurate determination of S_V.

In their analysis of grain growth exotherms, Chen and Spaepen[3] defined a geometric variable, g, by which grain boundary area per unit volume can be expressed in terms of mean grain radius, $\bar{r}$:

$$S_V = \frac{g}{\bar{r}}. \tag{2-3}$$

Chen and Spaepen estimated g to be 1.3 ± 0.2, depending on grain shape (spherical, cubic, tetrakaidecahedral) and size distribution (i.e. identical grains, lognormal distribution, Wagner-Hillert or Louat distributions). Several studies in the literature[4,6,14,15] have thus assumed the value $g=1.3$. Since in the present work we measure directly the grain size distribution, before and after grain growth, a more accurate determination of the change in grain boundary area is possible. For comparison, however, a g can be computed from our grain size distribution data (comparing Eqs. 2-2 and 2-3):

$$g = \frac{3.5513}{2} \exp\left[-2.5(\ln\sigma)^2\right] \tag{2-4}$$

Values of g in our samples vary from 1.05 to 1.54, in line with Chen and Spaepen's 1.3 ± 0.2 estimation. The g value for as-prepared samples was 1.42-1.54, indicating narrow size distributions. Size distributions broaden somewhat as grain growth progresses ($g=1.3$-1.43 in coarsened chemically-derived samples, 1.05-1.35 in inert gas-condensed samples), indicating that a departure from normal grain growth occurs in some of the samples studied.

2.3 EXCLUSION OF POSSIBLE ARTIFACTS IN THE DSC MEASUREMENTS

In many prior measurements of excess thermodynamic quantities of nanocrystalline materials,[4-6] a variety of thermal contributions are included. The possibility needs to be considered that extraneous heat-dissipating processes are the source of trends observed in the present measurements. Here we discuss the anatase-rutile phase transformation, relief of lattice strain, sintering, oxidation, and gas desorption. Table II-2 contains a summary of these potential artifacts in the DSC measurements of our chemically-derived TiO_2 and how they were addressed. The effect of residual anatase on the grain growth exotherm is illustrated by

TABLE II-2. Identification and resolution of potential artifacts in the calorimetric measurement of grain boundary thermodynamic properties in chemically-derived ultrafine-grained TiO_2.

Material Process	Contribution	Resolution
Anatase→rutile phase transformation	exothermic	Dope with Sn to stabilize rutile phase. No anatase by XRD (<5%).
Relief of lattice strain	exothermic	<0.04% rms strain indicated by XRD. Lattice strain energy < 1 J/mole.
Sintering (energy of free surfaces)	exothermic	High density samples.
Oxidation due to initial nonstoichiometry	exothermic	Oxidized prior to experiments. Yellow/white samples. No CSP's observed by TEM. No change in color or excess enthalpy after 500°C x 24h anneal in >2000 psi of pure oxygen. Weight gain during DSC run is below the detection limit of standard TGA.
Reduction	endothermic	Intrinsic reduction in air at 600-1100°C is negligible.[16]
Desorption of gaseous species	endothermic	Low residual chlorine (30-300 ppm). Dense, pre-annealed samples. No desorption observed by TGA.

30

curve (a) in Figure 2.1. X-ray diffraction indicated that this sample, doped with 0.56 mole% SnO_2, contained ~ 10% residual anatase, and dual peaks were resolved using differential scanning calorimetry. Increasing the doping level to ~ 1.1 mole% was effective in accelerating the formation of the rutile phase during calcination such that consolidated pellets were phase-pure rutile by x-ray diffraction. These samples always showed a single exotherm. A total enthalpy release (for combined phase transformation and grain growth) of -4.2 kJ/mole was measured upon transformation of dense, nanocrystalline, phase-pure anatase (no Sn dopant) to coarse-grained, phase-pure rutile.* Taking the detection limit of x-ray diffraction to be ~5%, the heat of phase transformation should be negligible in comparison to that for grain coarsening. Furthermore, all of the powders doped with ~ 1.1 mole% SnO_2 were hot pressed at a higher temperature and for a longer time than that at which they were calcined. Since the phase transformation is temperature-dependent and is aided by pressure (rutile having a smaller molar volume than anatase), the hot-pressed samples should be very close to 100% rutile. Thus, for samples showing a singular exotherm and no detectable anatase by XRD, we believe the contribution from the heat of transformation to be negligible.

The effects of using tin as a dopant must of course be considered. Tin and titanium ions are isovalent and TiO_2 (rutile) and SnO_2 are not only isostructural but have similar nonstoichiometry and lattice defect chemistry. Furthermore, STEM measurements showed no detectable segregation or depletion of Sn at grain boundaries, which will be discussed further in a subsequent section. For these reasons, we do not believe Sn doping influences the current measurements.

---

* The heat of transformation in the nanocrystalline anatase sample was less than that measured by Navrotsky and Kleppa (-6.57 kJ/mole) for coarse anatase,[17] for reasons which are presently unclear.

31
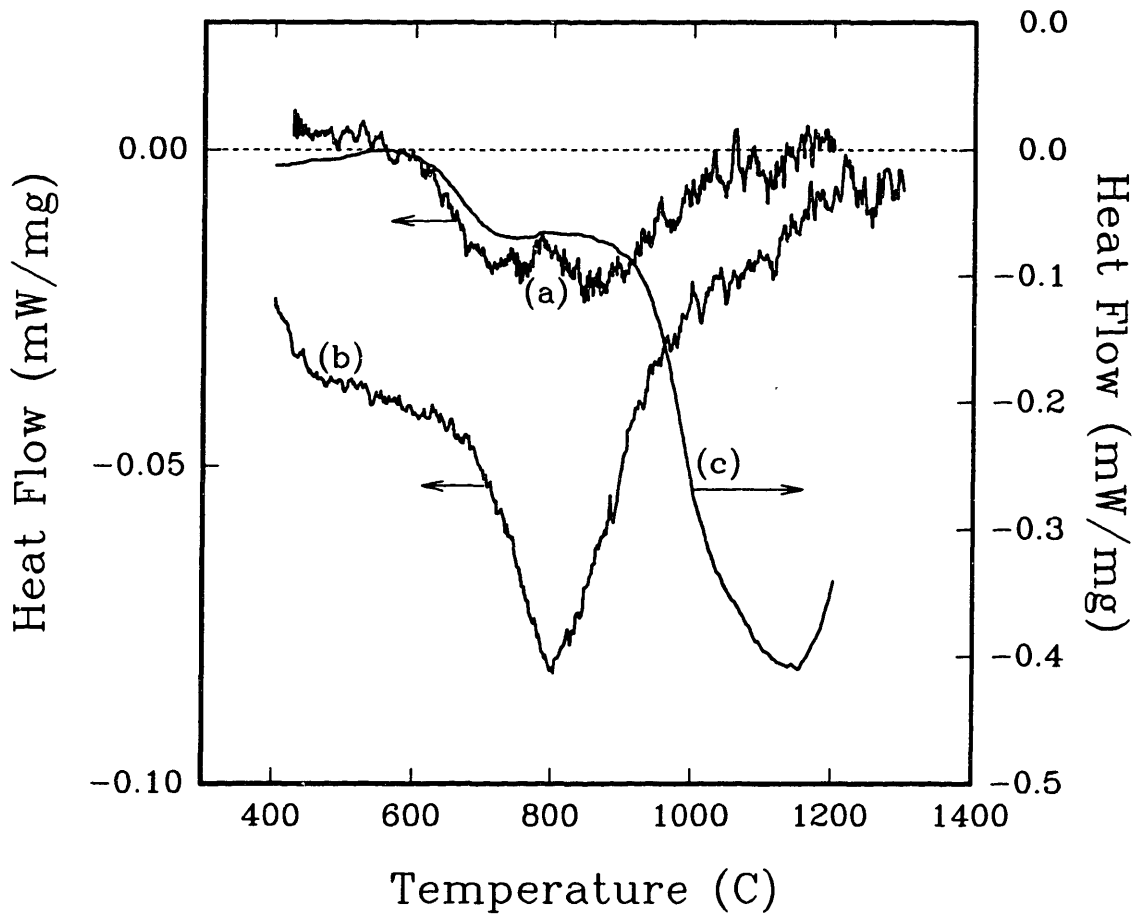
Figure 2.1. Effects of several different experimental artifacts on the "grain growth" exotherm measured by differential scanning calorimetry. The right side heat flow scale is for curve (c) only. (a) ~ 10% residual anatase, (b) Combined sintering and grain growth of a cold-pressed green pellet, (c) Combined oxidation and grain growth of some inert gas-condensed TiO_2. All exotherms are normalized for sample mass and heating rate, but not for initial grain size.

Because the samples were consolidated using a very high pressure which was likely to be non-uniform due to wall friction, the possibility that the samples contained residual strain was addressed. An estimate of lattice strain in several as-prepared samples (after the 500°C x 24h anneal) was made by analyzing x-ray line broadening according to the method described by Klug and Alexander.[18] Step scans of the six most intense rutile reflections were made using a Rigaku RU300 diffractometer and monochromatic Cu Kα radiation. Each peak was corrected for Kα$_2$ broadening[19] and instrumental broadening prior to calculation of its integral breadth (integrated area/peak intensity). Methods for separating size and strain contributions to line broadening make use of the fact that strain broadening scales with the reciprocal space variable s ($s=2\sin\theta/\lambda$) while size broadening is independent of s. The equivalent of these relations on the (2θ) scale is that strain effects scale as $1/\tan\theta$ while size effects scale as $1/\cos\theta$.[18] Assuming a Gaussian distribution for the profile due to strain broadening and a Cauchy distribution for the profile due to size broadening, the convolution of the two effects is expressed by:[18]

$$\frac{(\delta 2\theta)^2}{\tan^2\theta_0} = \frac{K\lambda}{L} \cdot \frac{\delta 2\theta}{\tan\theta_0 \sin\theta_0} - 25\langle\varepsilon^2\rangle \qquad (2\text{-}5)$$

where ($\delta 2\theta$) is the integral breadth after correction for Kα$_2$ and instrumental broadening, θ_0 is the Bragg angle, K is a constant taken as unity, λ is the x-ray wavelength, L is the crystallite size, and $\langle\varepsilon^2\rangle^{1/2}$ is the root mean square strain. Thus the rms strain is found as the y-intercept of a plot of $(\delta 2\theta)^2/\tan^2\theta_0$ versus $(\delta 2\theta)/\tan\theta_0\sin\theta_0$. Using this method, annealed fine-grained samples were found to have zero strain, with an error limit of 0.04% considering the uncertainty in the linear regression analysis. (The rms strain of nanocrystalline metals and alloys can vary from 0.2-3%.[4-6,20,21]) Approximating the strain energy as $\frac{1}{2}E\varepsilon^2$ and using a calculated aggregate value for the Young's modulus, E, of rutile,[22] the maximum

contribution to the total excess enthalpy from relief of lattice strain is < 1 J/mole, certainly negligible in comparison to the total excess enthalpies that were measured.

In incompletely dense samples the heat of sintering may be an additional exothermic contribution since the specific enthalpy of a free surface is expected to be larger than that of a grain boundary. Curve (b) in Figure 2.1 shows the normalized heat flow upon the combined sintering and grain growth of a cold-pressed green compact of ultrafine rutile powder. This extraneous contribution from sintering was minimized by imposing the requirement that all samples be > 95% of theoretical density. In general, the change in density of the samples during the DSC runs was below the error of the Archimedes measurement technique.

Curve (c) in Figure 2.1 shows the heat flow obtained upon simultaneous oxidation and grain growth of a nanocrystalline TiO_{2-x} sample prepared by inert gas condensation. Note the much larger heat flow scale for curve (c) in comparison to the others. As described in section 2.2.1, inert gas-condensed nanocrystalline TiO_2 is prepared by the oxidation of titanium clusters, which is an inherently exothermic, rapid, and sometimes incomplete process. Unless oxidation is controlled, the resulting powder can be quite oxygen-deficient, as has been observed by several researchers.[23-25] The samples we prepared using inert gas-condensed powders were generally dark gray in color, which is a common manifestation of nonstoichiometric TiO_2. Oxygen anneals at temperatures below the onset of grain growth only partially oxidized the samples, and after the DSC runs they remained mottled with gray and black regions. Furthermore, areas with a high density of intragranular planar defects were observed by TEM,[26] some of which were identified as crystallographic shear planes (CSP's) known to accommodate nonstoichiometry in rutile.[27] Thus, the excess enthalpies of inert gas-condensed TiO_2 (reported in

34

Table II-3) are likely to include a significant contribution from oxidation and the removal of planar defects, and use of these materials for measurement of grain boundary properties was not pursued further.

Several observations suggest that our chemically-derived samples are fully oxygenated in the as-prepared condition. The samples are uniformly light yellow or off-white which is consistent with highly oxidized rutile, and no crystallographic shear planes were observed by TEM. A sample saturated with oxygen by annealing at 500°C for 24 hours in 2000-2500 psi of pure oxygen showed no change in color, and its grain boundary enthalpy was in line with that of samples annealed in air. Thus, we are confident that the as-prepared samples are in an "equilibrium" oxidation state. However, as discussed later in relation to the size/temperature dependence of H_{gb}, an intriguing possibility is that this equilibrium state is intrinsically off-stoichiometry due to the very fine grain size. The heat of oxidation of TiO_{2-x} is large enough such that a small amount of nonstoichiometry can contribute a non-negligible excess enthalpy.

Even though no endotherms were observed, two endothermic phenomena deserve mention. First is intrinsic reduction of TiO_2, which is negligible in coarse rutile crystals in the temperature range and oxygen partial pressure of our experiments.[16] Second, desorption of gaseous species is also endothermic, and the presence of adsorbed gaseous species would inflate the heat capacity of as-prepared samples. This artifact was likely to be a factor in the initial reports of excess heat capacities of 20-30% of the single crystal value (and resulting claims of large excess entropy) in low density nanocrystalline metals.[28,29] The desorption of these species at high temperatures was later observed using differential scanning calorimetry as an endotherm following the grain growth exotherm.[30] This extent of desorption is not likely in our samples, which are dense, pre-annealed, and have low levels of

35

residual chlorine (30-260 ppm). No endotherms were observed up to 1300°C, and no desorption was evident by thermal gravimetric analysis (Perkin-Elmer TGA7).

2.4 RESULTS

An example of a scanning DSC measurement of chemically-derived TiO_2 with an initial mean grain size of 34 nm is shown in Figure 2.2. The onset of grain growth occurs between 600-650°C, near the hot pressing temperature. In all cases the peak appears to be singular; using heating rates from 10-40°/min, no shoulders or inflection points were resolved that would suggest more than one thermally-activated process.

Figure 2.3 shows an example of an isothermal DSC measurement in which TiO_2 with an initial mean grain size of 39 nm was heated at 20°/min to 750°C and held isothermally for 30 minutes. Once the isothermal segment begins, the heat flow signal decays monotonically, which is characteristic of normal grain growth,[3] as well as any general relaxation process.[31,32] (Thus, this decaying signal is a necessary but not sufficient condition to identify the thermal event as grain growth.) Representative TEM images of the as-prepared and coarsened microstructures of this sample are shown in Figure 2.4, along with the grain size histograms and cumulative probability plots from which the change in grain boundary area was calculated. The linearity of the cumulative probability plot of the as-prepared sample indicates a lognormal distribution of grain sizes. In most cases, the cumulative probability plots before and after grain growth were superimposed, which is one indicator of a normal grain growth process in which the initial grain size distribution is maintained throughout. The example shown is one of several cases in which the upper end of the distribution changed slightly during coarsening due to a subpopulation of clustered, large grains such as those shown in Figure 2.5.

36
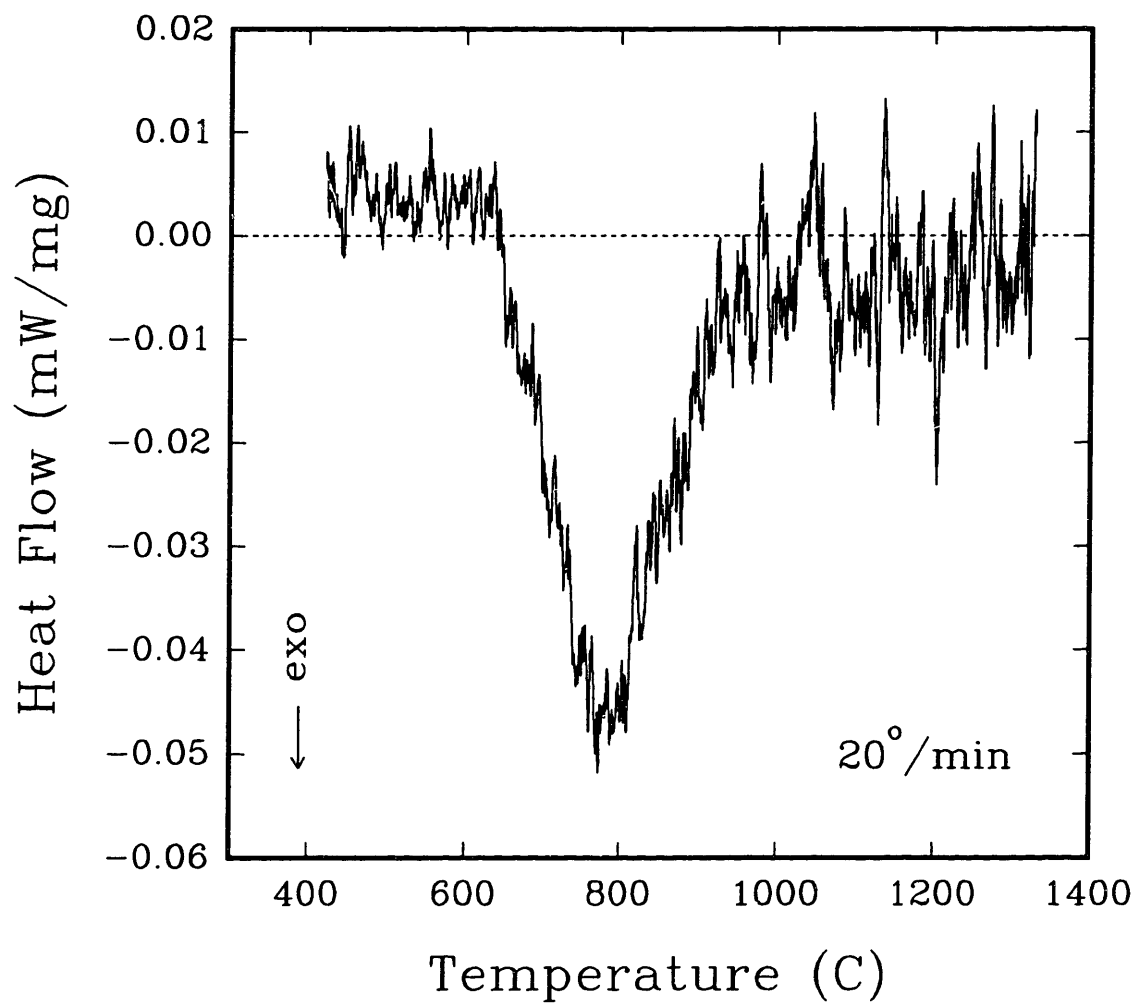
Figure 2.2. Heat flow measured during a scanning DSC run (20°/min) of TiO$_2$ with an initial mean grain size of 34 nm.
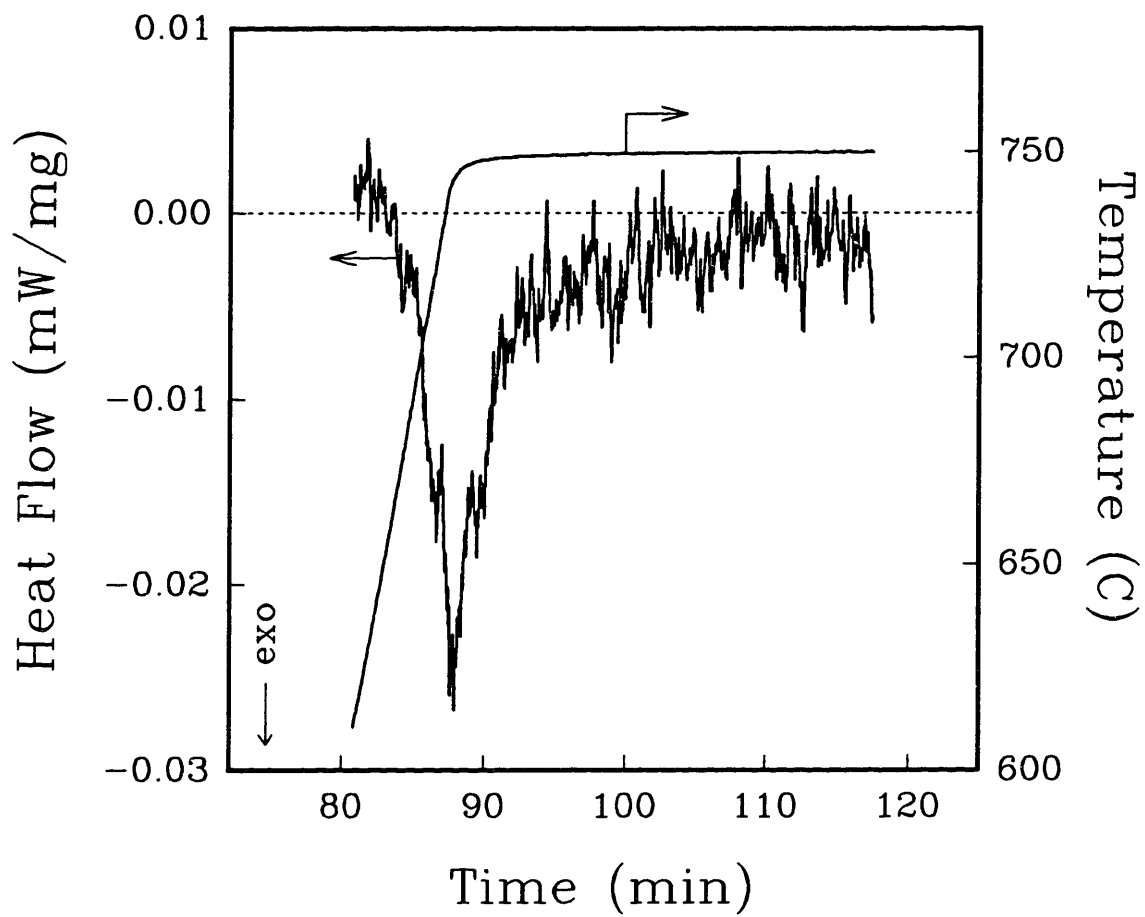
Figure 2.3. Heat flow measured during an isothermal DSC measurement of TiO_2 with an initial mean grain size of 39 nm. The sample was heated at 20°/min to 750°C and held isothermally for 30 minutes.
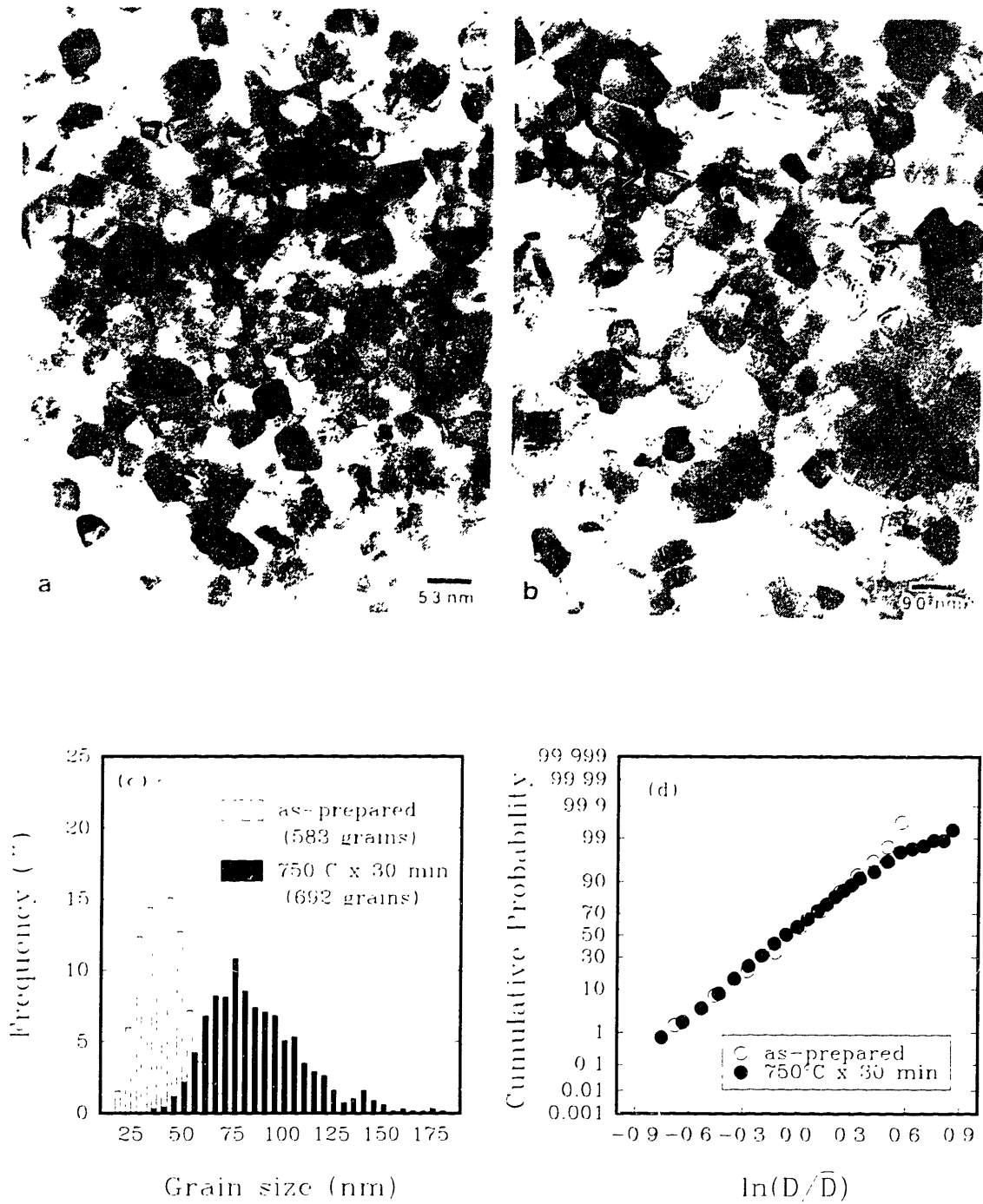
Figure 2.4. Bright field TEM images of the microstructure (a) before and (b) after the exotherm shown in Figure 2.2. (c) Grain size histograms and (d) cumulative probability plots of the as-prepared and post-isotherm microstructures.
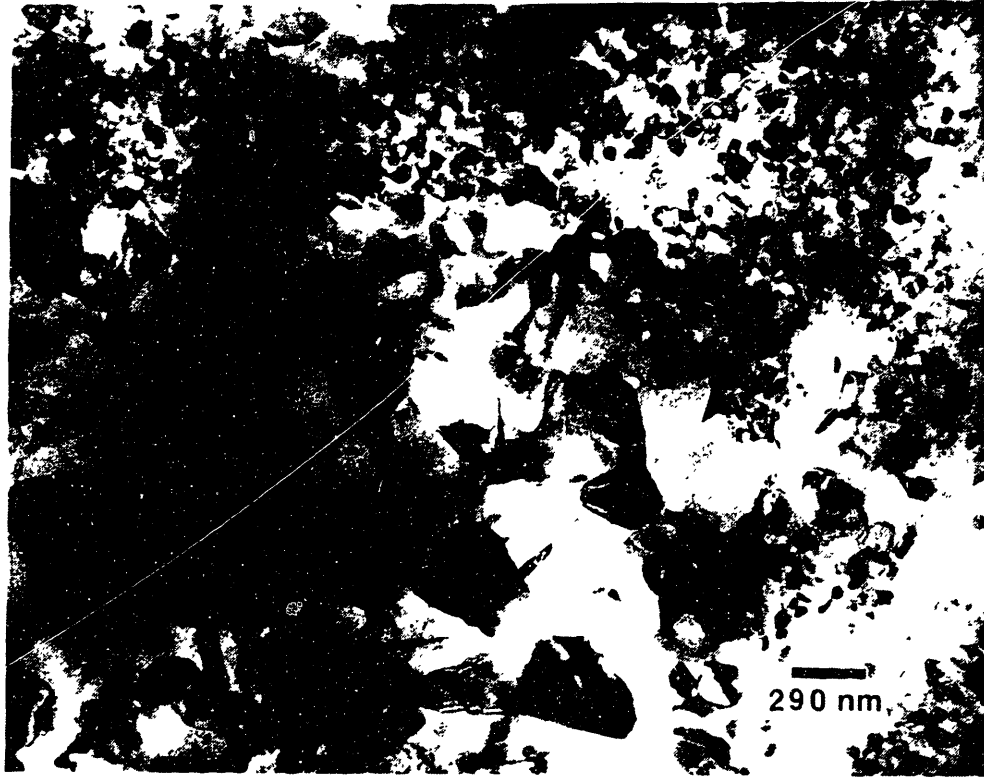
Figure 2.5. An example of a pocket of discontinuous grain growth that was observed occasionally in as-prepared and coarsened microstructures.

The source of these clusters could be topological or chemical (perhaps Si) inhomogeneities in the TiO_2 powders and consolidated samples. However, the subpopulations of these abnormal grains were so small ($< \sim 1\%$, Fig. 2.3(d)) that we can conclude that normal grain growth was predominant in all of the samples.

The measurements of grain boundary enthalpy for both chemically-derived and inert gas-condensed TiO_2 are summarized in Table II-3, from which four key observations can be made:

1. The apparent grain boundary enthalpies of the inert gas-condensed samples are about three to five times larger than those of chemically-derived samples measured by the isothermal technique in the same temperature range. The source of this excess is likely to be the large nonstoichiometry of the inert-gas condensed samples, as discussed in the preceding section.

2. The specific grain boundary enthalpies of the chemically-derived samples measured in scanning runs to 1300°C ($1.3 \sim 1.7$ J/m^2) are considerably larger than those measured in isothermal runs between 650°C and 780°C ($0.4 \sim 1.0$ J/m^2).

3. For isothermal measurements of the chemically-derived samples, H_{gb} increases as the isothermal temperature increases. Since the initial grain sizes of these samples are quite similar, this trend can also be thought of as an increasing H_{gb} with increasing final grain size.

4. The specific grain boundary enthalpy measured in scanning runs over the same temperature range (600-1300°C) increases as the initial grain size increases. Viewed another way, if a median temperature for scanning runs is defined as the temperature at which one half of the total excess enthalpy has been released, the specific grain boundary enthalpy measured by scanning runs tends to increase with the median temperature of the exotherm.

TABLE II-3. Summary of excess enthalpy measurements of ultrafine-grained TiO_2.					
Sample	Temperature of measurement[†]	ΔH (J/mole)	Mean grain size (nm) initial	final	H_{gb} (J/m^2)
Isothermal measurements:					
Chemically-derived samples:					
S3A	670°C	-391	39.6	75.3	0.50
S3G	700°C	-274	35.0	55.5	0.42
S3H	710°C	-484	35.0	63.3	0.64
S3J	750°C	-597	39.4	84.9	0.76
S3B	780°C	-1092	37.8	193	0.94
Inert gas-condensed samples:[‡]					
NT1	650°C	-717	33.8	65.4	1.29
ANL1	670°C	-2260	31.2	87.8	2.00
ANL0	689°C	-3250	32.4	75.7	3.22
Scanning measurements:					
Chemically-derived samples:					
S3D	796°C	-2190	33.6	↑	1.29
S2B	851°C	-1410	45.9		1.34
S2I*	886°C	-1425	53.8	~2μm	1.43
S2A	855°C	-1480	57.2		1.50
S2G	889°C	-1072	75.6		1.69
S1C	885°C	-1060	76.6	↓	1.55

† All scanning measurements occurred in the temperature range 600-1300°C. A median temperature is reported, at which one half of the excess enthalpy had been released.

‡ NT refers to powder from Nanophase Technologies Corporation (Darien, IL); ANL refers to powder from Argonne National Laboratory.

* This sample was annealed in 2000-2500 psi of pure oxygen at 500°C for 24 hr. prior to the DSC experiment. All other samples were annealed in air for the same period.

The trends in H_{gb} that are apparent in Table II-3 are illustrated graphically in Figures 2.6 and 2.7, both of which emphasize the apparent size and/or temperature dependence of the specific grain boundary enthalpy. Grain size and temperature effects cannot be separated because of the inextricable link between them. For example, comparison of two isothermal measurements conducted with an identical heating schedule but with different initial grain sizes might seem to allow separation of the two effects, but since the onset of grain growth is a function of grain size, the median temperature of the two measurements would vary as well.

Recalling previous discussion, at larger grain sizes the projected dimension method may tend to overestimate S_V. However, this would result in ΔS_V's that are too large and thus H_{gb}'s (J/m^2) that are too small. Therefore, the trend of increasing H_{gb} with increasing grain size cannot be explained by overestimates of S_V at larger grain sizes.

2.5 ORIGIN OF A SIZE OR TEMPERATURE DEPENDENCE OF THE GRAIN BOUNDARY ENTHALPY

2.5.1 Size-Dependent Nonstoichiometry

Theoretical studies have shown that defect formation energies at grain boundaries are lower than those within the bulk,[33-35] resulting in an enhanced equilibrium concentration of defects near grain boundaries. Hence, one expects the total defect concentration of any polycrystal (and thus the total heat of grain growth and oxidation) to increase with total grain boundary area. However, this effect is intrinsic to all grain boundaries and would be contained within the excess properties normalized to area; it would not appear as a size-dependent quantity unless the grain boundary defect formation energies also varied with size. Since our measurements of specific grain boundary enthalpy are normalized to the change in grain boundary

43
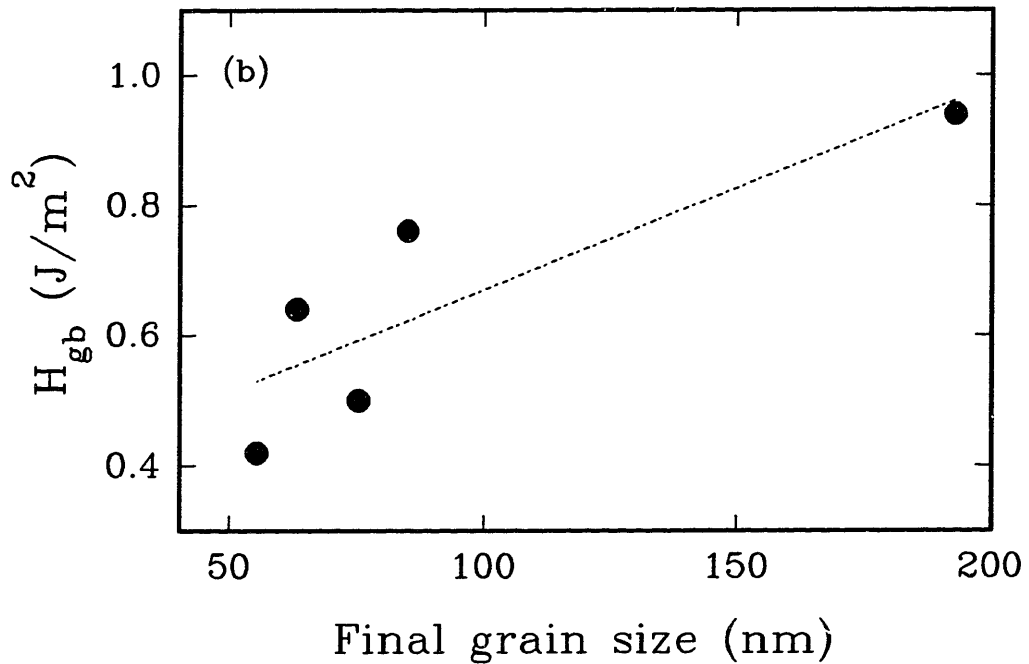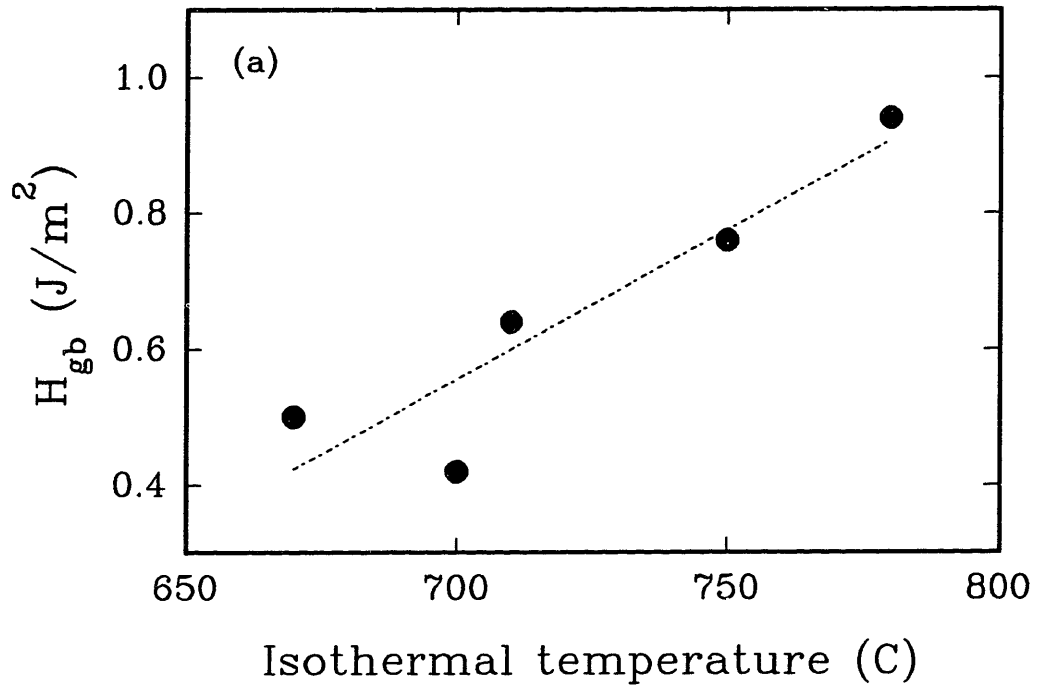
Figure 2.6. Isothermal measurements of the grain boundary enthalpy, H_{gb}, of chemically-derived samples as a function of either (a) isothermal temperature or (b) final grain size. These measurements indicate a size and/or temperature dependence of the grain boundary enthalpy.
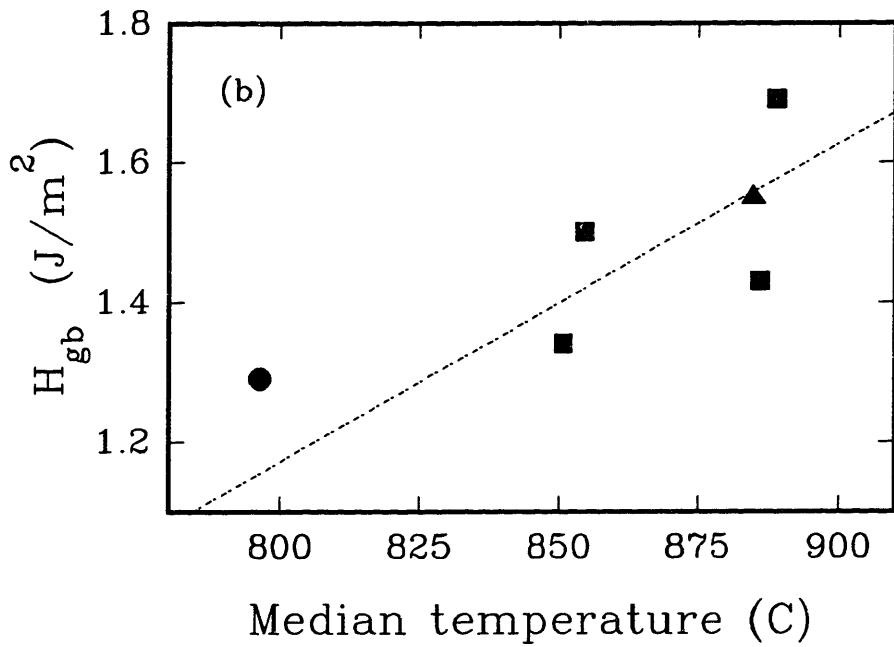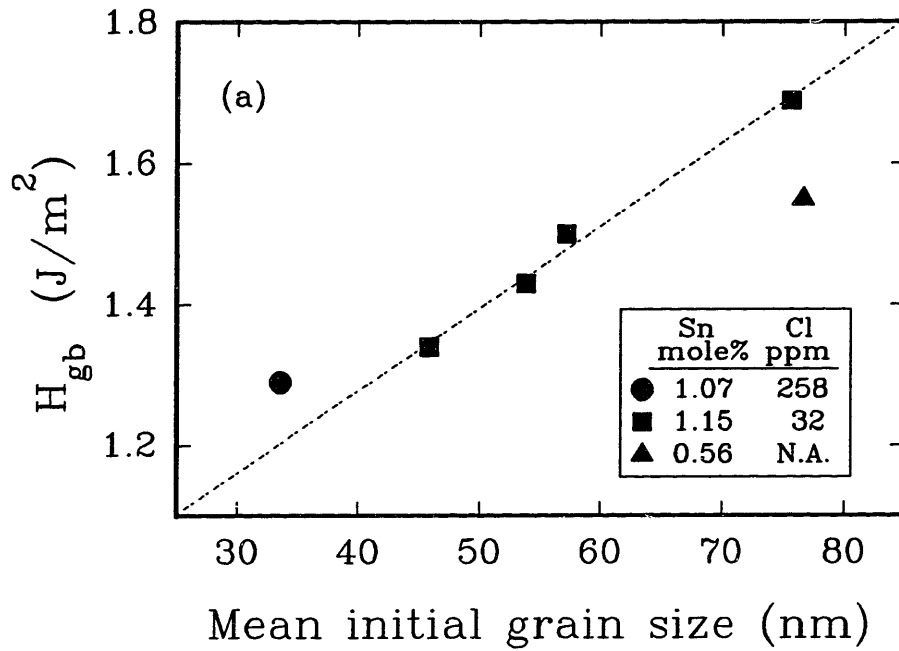
Figure 2.7. Grain boundary enthalpy measured by scanning runs from room temperature to 1300°C, as a function of (a) initial grain size or (b) median temperature of the grain growth exotherm.

area ($H_{gb}=\Delta H_{tot}/\Delta S_V$), this effect seems unable to explain the size- or temperature-dependent H_{gb}. That is, if an excess of defects is to explain the results, this excess must scale with volume rather than grain boundary area (i.e. $\Delta x \propto r^{-3}$ rather than r^{-2}). On the other hand, a reasonable explanation for a size dependence of the excess enthalpy is a size-dependent nonstoichiometry of TiO_2. We now demonstrate qualitatively that the impingement of space charge layers at very fine grain sizes is a plausible explanation for a size-dependent nonstoichiometry of TiO_2, and thus a size/temperature-dependent H_{gb}.

TiO_2 is an intrinsically nonstoichiometric oxide (TiO_{2-x})[16] because of the dual valence states of the titanium ion (Ti^{4+}, Ti^{3+}). Since oxidation of TiO_{2-x} is an exothermic process, were more oxidation to occur (larger Δx) as temperature and grain size increase , H_{gb} would appear to increase correspondingly. The fact that one of our as-prepared samples showed no change in color and no decrease in excess enthalpy after a high pressure oxygen treatment ($500°C \times 24$ h. in 2000-2500 psi of pure oxygen) suggests that the initial stoichiometry has reached an extremely stable, if not equilbrium, value for the initial grain size and temperature. Using an average literature value for the heat of oxidation of TiO_{2-x} (-544 kJ/mole),[36,37] the complete oxidation of an initial nonstoichiometry of $x \sim 0.027$ in a grain boundary region of 1 nm thickness would be sufficient to account for the difference in grain boundary enthalpy (~ 0.5 to 1.3 J/m^2) between an isothermal measurement at $670°C$ and a scanning measurement. Alternatively, a difference in initial and final bulk nonstoichiometry of $x \sim 0.0025$ would account for the difference as well. This level of nonstoichiometry would be much greater than that which occurs in pure, coarse-grained rutile in air at these temperatures.[16]

It is well recognized[38-42] that since grain boundaries in ionic systems are a source and sink of defects, they often have a net charge due to unequal formation

energies of individual defects. In extrinsic materials, the sign and magnitude of the potential is determined by defects due to doping or nonstoichiometry. For overall charge neutrality, space charge layers are formed adjacent to boundaries, comprised of oppositely charged defects from the bulk. The Debye length of the space charge layer is given by:

$$\delta = \left[\frac{\varepsilon \varepsilon_0 kT}{e^2 \sum_i (N_i z_i^2)} \right]^{1/2} \tag{2-6}$$

where ε is the static dielectric constant of TiO_2,[43] ε_0 is the permittivity of free space, e is the elementary charge, and N_i and z_i are the total concentration (cm^{-3}) and effective charge of defect species i. Thus, defect concentrations, which are governed by either intrinsic or extrinsic disorder, are the most influential factors determining the distance that space charge layers extend into the bulk; low defect concentrations yield large Debye lengths.

ICP analysis of our calcined TiO_2 powders (Table II-1) indicates no significant aliovalent impurities above the detection limit (for example, < 100 ppm Al, < 50 ppm Fe). Due to the high purity of this TiO_2, combined with the large amount of grain boundary area acting as a sink for any impurities (see Chapter 4), it is likely that the bulk defect chemistry in these samples is governed by intrinsic disorder. For intrinsic reduction of TiO_2, there is slightly more evidence that titanium interstitials are favored energetically over oxygen vacancies.[42] Assuming this to be the case, a quasi-chemical defect reaction for reduction and oxidation can be written using Kröger-Vink notation as:

$$Ti_{Ti}^{X} + 2O_O^{X} \leftrightarrow Ti_i^{\cdots\cdots} + 4e' + O_2(g) \tag{2-7}$$
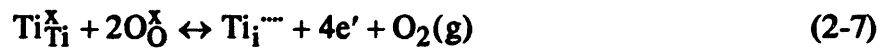
with a mass-action equilibrium constant given by:

$$K = \left[Ti_i^{\cdots}\right]n^4 p_{O_2}. \tag{2-8}$$

Ikeda and Chiang[44] have conducted a review of defect equilibrium constants for TiO_2 from previous literature studies, from which we extrapolate a K of $9.9 \cdot 10^{76}$ and $2.3 \cdot 10^{84}$ atm·cm^{-15} at 800° and 1000°C, respectively. Assuming electrons and titanium interstitials to be the dominant defects, the overall electroneutrality condition is given as $n = 4[Ti_i^{\cdots}]$, and n and $[Ti_i^{\cdots}]$ can be calculated using Eq. 2-8 for a p_{O_2} of 0.21 atm (air). Debye lengths of 165 nm and 33 nm at 800° and 1000°C, respectively, are then calculated using Eq. 2-6. Thus, it is clear that if disorder is governed by intrinsic reduction, space charge layers impinge at the fine grain sizes of the current materials.

Several theoretical and experimental studies have examined space charge effects when the characteristic sample length (usually a thin film) is of the same order as the Debye length.[45-48] Figure 2.8 illustrates the effect schematically for simplified, two-dimensional grains and a Debye length of 33 nm. The charge distribution is sensitive to grain size, and it can be seen that to maintain overall charge neutrality, the grain boundary defect concentration compensating the space charge must scale with grain size. Furthermore, it is apparent that the concentration of grain boundary defects in this size regime does not scale simply with the grain boundary area. As space charge fields impinge, the defect concentration *per unit volume* scales with grain size. Thus, we hypothesize that when the total excess enthalpy due to grain growth and oxidation is normalized to the change in grain boundary area, the volume effect of impinging space charge layers is manifested in a size-dependent H_{gb}.

In an initial experiment to explore the possibility of oxidative weight gain during grain coarsening, an as-prepared sample was coarsened in a Perkin-Elmer
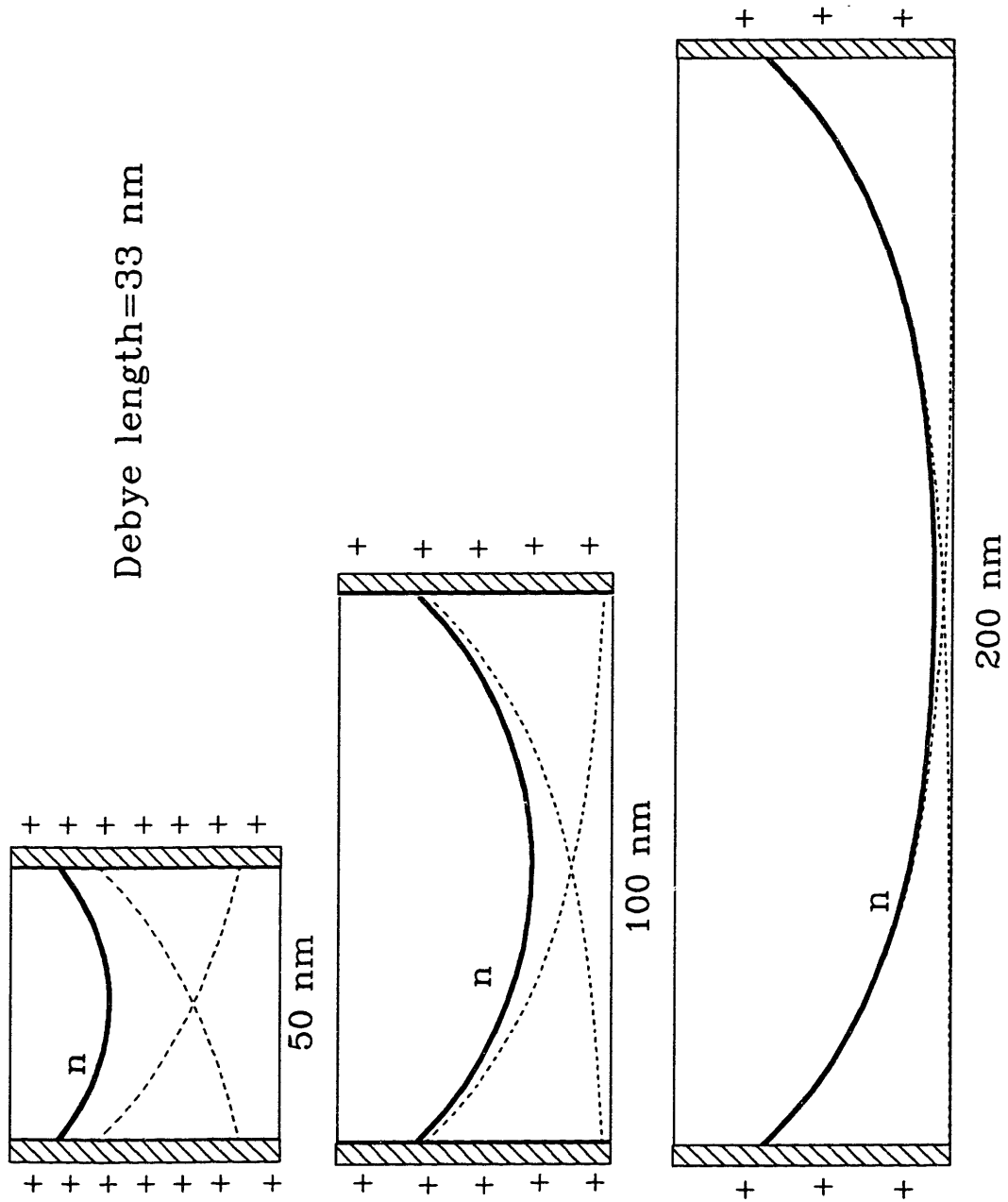
Figure 2.8. Schematic illustration of the effect of impinging space charge layers on defect concentrations within the bulk and at grain boundaries for a grain size of 50, 100, or 200 nm when the Debye length is 33 nm. The defect concentration range of the y-axis is identical for all three cases.

TGA7 using a heating schedule identical to that of a scanning DSC run. No detectable weight gain was observed, but the weight gain associated with the expected amount of oxidation is close to the sensitivity of the instrument. High sensitivity thermogravimetry would help to clarify this issue.

2.5.2 Solute Segregation

One source of size-dependent grain boundary thermodynamic properties in ultrafine-grained materials with a considerable amount of solute is likely to be grain boundary segregation. For TiO_2 doped with 0.34 mole% calcium, we have used STEM microanalysis to show that at grain sizes <200-400 nm, grain boundary coverage (Ca ions/cm^2) increases with grain size and is insensitive to temperature (see Chapter 4). In such a case, a change in grain boundary enthalpy with grain size would not be unexpected. However, STEM microanalysis of our Sn-doped samples indicates negligible interaction between Sn and grain boundaries. The average excess Sn density at grain boundaries was measured as $1.3(\pm2.5) \cdot 10^{13}$ cm^{-2} for a mean grain size of 63 nm and $-5.7(\pm2.0) \cdot 10^{13}$ cm^{-2} for a mean grain size of 587 nm. These coverages/depletions are equivalent to just a few percent of a monolayer (one monolayer=$1.01 \cdot 10^{15}$ cm^{-2} for TiO_2), and as such, a change in grain boundary chemistry can be eliminated as an explanation for the large size or temperature dependence of H_{gb} in Sn-doped TiO_2.

2.5.3 Grain Boundary Structure

Little is known about the temperature dependence of the grain boundary enthalpy. Modeling of grain boundaries at finite temperatures is quite complex, and most experimental methods that have been used to measure grain boundary energy (zero creep, dihedral angles) are limited to temperatures near the melting point.[49] Furthermore, experimental measurements of the change in dihedral angle with

temperature are a reflection of the temperature dependence of the grain boundary free energy, not the grain boundary enthalpy. Recently, Sutton has calculated the thermodynamic properties of a $\Sigma = 13$ (001) twist boundary in Au at 600 and 1200K using temperature-dependent interatomic forces within a molecular statics relaxation algorithm.[50] The results indicate a temperature-dependent enthalpy, entropy, and specific heat. Although the calculated temperature dependence of the enthalpy of this special coincidence boundary in Au was less than what we have measured for TiO_2, it would not be surprising if the enthalpy of a general high angle boundary, with its larger excess volume, exhibits a steeper temperature dependence.

The possibility of an intrinsic size dependence of H_{gb} has been a subject of some interest in the literature. Fecht has made the argument[51] that larger grain boundary enthalpies are to be expected in nanocrystalline materials due to evidence from many vibrational spectroscopy studies that the excess volume of grain boundaries increases as grain size decreases, coupled with computations that show excess volume to be the most important determinant of energy for general high angle grain boundaries.[52] However, this intuitive trend is opposite that indicated by our H_{gb} measurements.

Lu and coworkers have measured interfacial excess enthalpies of Ni-P alloys with different grain sizes, by means of the calorimetric measurement of the amorphous-to-nanocrystalline transformation in their samples.[53] In contrast with Fecht's theoretical work and similar to ours, Lu et al found the excess enthalpy to increase linearly from 2.23 kJ/mole for a grain size of 7 nm to 8.84 kJ/mole for a grain size of 60 nm (where the data have been normalized to moles of grain boundary atoms). Interestingly, Lu et al also use the coupling of excess volume and excess energy to explain their results, since they found evidence by positron annihilation spectroscopy and density measurements that in their samples, the excess

volume of grain boundaries increases with grain size, opposite to what one would expect intuitively. Lu *et al* suggest that an increasing boundary enthalpy with increasing grain size may be a common feature of nanocrystalline materials that would explain their unusual resistance to grain growth (in spite of the large driving force) and abnormal Hall-Petch behavior that has frequently been reported.

2.5.4 Grain Boundary Triple Junctions

At very fine grain sizes, grain boundary triple junctions begin to comprise a significant fraction of the total intercrystalline volume. Modeling grains as regular tetrakaidecahedra and grain boundaries and triple junctions as hexagonal and triangular prisms, respectively, Palumbo and coworkers have shown[54] that at grain sizes ≤10 nm, if properties are observed to be grain size-dependent, the primary contribution is from triple junctions rather than grain boundaries. However, using the relations derived by Palumbo *et al* for a grain size of 30 nm and a grain boundary and triple junction thickness of 1 nm, triple junctions comprise only ~0.3% of the total volume and only ~3% of the total intercrystalline volume (grain boundaries and triple junctions). Thus, the influence of triple junctions is negligible in our experiments and is not likely to be a contributing factor to a size-dependent H_{gb}.

2.6 SUMMARY

Direct measurements of the excess thermodynamic properties of grain boundaries in TiO_2 have been made by calorimetrically monitoring grain growth in ultrafine-grained samples. These measurements indicate a clear size or temperature dependence of the specific grain boundary enthalpy, which increases from ~0.5-1.0 J/m^2 at fine grain sizes and low temperatures (30~200 nm, 600-780°C) to 1.3 - 1.7 J/m^2 when measured over a much larger grain size and temperature range

52

(30 nm ~ 2µm, 600-1300°C). Extraneous heat contributions from the anatase-rutile phase transformation, sintering, and lattice strain have been shown to be negligible. Solute segregation, grain boundary structure, and grain boundary triple junctions have been considered as origins of a size- or temperature-dependent H_{gb}, but the most plausible explanation is shown to be a size-dependent nonstoichiometry of TiO_2 due to the impingement of space charge layers in this grain size and temperature range. Debye lengths of 165 nm and 33 nm are estimated at 800° and 1000°C, respectively, assuming that disorder is governed by intrinsic reduction. It is shown that when space charge layers overlap, the grain boundary defect concentration scales with volume rather than grain boundary area. Oxidation of grain boundaries as grain growth occurs would then result in a size-dependent H_{gb}.

CHAPTER 3

MEASUREMENTS OF THE EXCESS HEAT CAPACITY
OF ULTRAFINE-GRAINED TiO$_2$

3.1 INTRODUCTION

Grain boundaries are expected to have an excess heat capacity due to the wider range of vibrational modes which are available to atoms located in the more open environment of a grain boundary than to atoms confined in a perfect lattice. Experimental measurements or theoretical calculations of grain boundary heat capacity have been rare, and ultrafine-grained materials provide an opportunity to measure this fundamental thermodynamic property for general, high angle grain boundaries. Just as an average grain boundary enthalpy can be measured directly from the heat released during coarsening of a fine-grained material, an average grain boundary heat capacity can be measured from the difference in heat capacity between fine-grained and coarse-grained structures, if the change in grain boundary area is known and if no other structural or chemical changes have occurred simultaneously. This chapter reports on our efforts to measure the excess heat capacity of ultrafine-grained TiO$_2$. For all samples, a positive excess heat capacity has been detected. The results are analyzed by normalizing the excess heat capacity to the change in grain boundary area to allow for comparison between samples, and by comparing the temperature dependence of H$_{gb}$ predicted by these heat capacity measurements with direct measurements of H$_{gb}$ as a function of temperature that were discussed in the previous chapter.

3.2 EXPERIMENTAL METHOD

All ultrafine-grained TiO$_2$ samples were given a 500°C, 24 hour anneal after hot pressing. The excess heat capacity of these samples was measured as follows.

After baseline and sapphire runs, the as-prepared sample was placed in the DSC and heated from room temperature to 400-500°C at 10°/min. This run was then repeated to ensure that no relaxation had occurred during the first run. Because of the prior anneal at 500°C, negligible grain growth occurs during this C_p measurement. The sample was then coarsened in-situ (using either a scan to 1300°C or an isothermal hold at an intermediate temperature), allowed to cool, and the 10°/min scan to 500°C was repeated (now for the coarsened microstructure) without disturbing the sample or furnace. Selected samples were given an additional fourth run, and the C_p-T functions measured by the third and fourth runs were indistinguishable from one another.

Heat capacity is calculated by comparing the DSC signal of the baseline (V_{bl}), the signal of a sapphire standard (V_{saph}) whose C_p-T function is known, and the signal of the sample whose heat capacity is to be determined (V_{sample}). At temperature T, the heat capacity is given as:

$$C_P^{sample}(T) = \frac{M_{saph}}{M_{sample}} \cdot \frac{V_{sample}(T) - V_{bl}(T)}{V_{saph}(T) - V_{bl}(T)} \cdot C_P^{saph}(T) \qquad (3\text{-}1)$$

where M_{saph} and M_{sample} are the mass of the sapphire and sample, respectively. This C_p-T data was then fitted using a least-squares algorithm to the function:

$$C_P = A + BT + CT^{-2} \qquad (3\text{-}2)$$

where A,B, and C are constants and T is in °K. The excess heat capacity of the nanocrystalline structure relative to the coarsened structure was calculated from the least-squares fits of the C_p-T data as:

$$\Delta C_P(T) = C_P^{nano}(T) - C_P^{coarse}(T) \qquad (3\text{-}3)$$

where ΔC_p is in units of $Jg^{-1}K^{-1}$.

3.3 INSTRUMENTAL ERROR

The magnitude of ΔC_p that can be attributed to instrumental error was determined by conducting the identical sequence of measurements and calculations using dense polycrystalline Al_2O_3 (inert over the temperature range of interest) of approximately the same thermal mass as the TiO_2 samples. Figure 3.1 shows the raw data of two consecutive heat capacity measurements of Al_2O_3, along with the least-squares fits to the data. When the second measurement is subtracted from the first, a difference of ~ -0.2-0.05% of the heat capacity is indicated. Thus, ±0.2% is used as an estimate of the precision of two consecutive heat capacity measurements of an inert sample, and only ΔC_p measurements ≥0.4% of the heat capacity should be considered significant.

3.4 RESULTS

The raw data of four heat capacity measurements are shown in Figure 3.2. The mean grain size of the microstructure during each heat capacity measurement is also indicated, along with the change in grain boundary area (ΔS_V) between measurements and the thermal history of the samples. In some cases an excess heat capacity of the ultrafine-grained structure is quite obvious (Fig. 3.2(a),(b)), while in others it is much less so (Fig. 3.2(c),(d)).

Figure 3.3(a) plots ΔC_p ($Jg^{-1}K^{-1}$) as a function of temperature for each of the samples shown in Fig. 3.2. The error bar in Fig.3.3(a) indicates the magnitude of ΔC_p that may be due to instrumental error; it can be seen that some, but not all, of the variation in magnitude and temperature dependence of the excess heat capacity between different TiO_2 samples can be attributed to instrumental error. Particularly noteworthy in Figs.3.2 and 3.3(a) is the small difference in the nanocrystalline and coarsened C_p's of samples (c) and (d), even though the

56
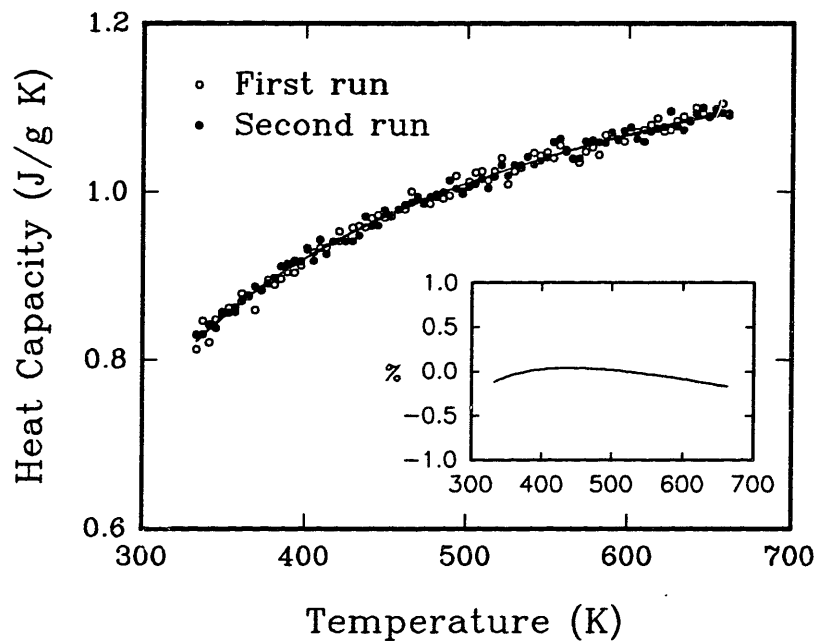
Figure 3.1. Two consecutive heat capacity measurements of dense, polycrystalline Al$_2$O$_3$, which is inert over the temperature range of interest. When the second measurement is subtracted from the first, as is done to determine the excess heat capacity of a nanocrystalline sample, a difference of approximately ±0.2% of the heat capacity is indicated over the temperature range of interest.

57
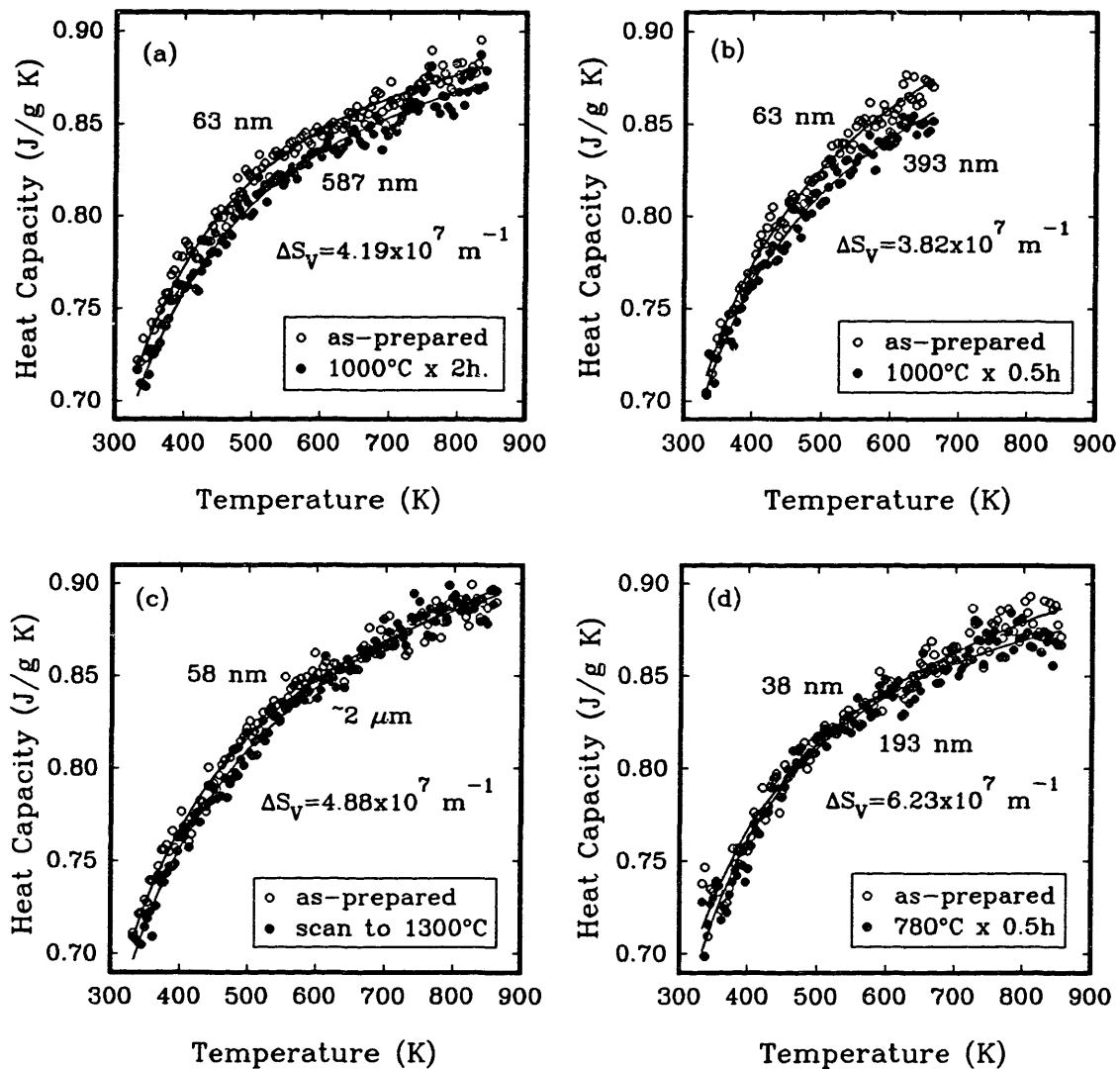
Figure 3.2. Four examples of excess heat capacity measurements of ultrafine-grained TiO_2 samples. The mean grain size of the microstructure during each heat capacity measurement is indicated, along with the change in grain boundary area (ΔS_V) between measurements and the thermal history of the samples.
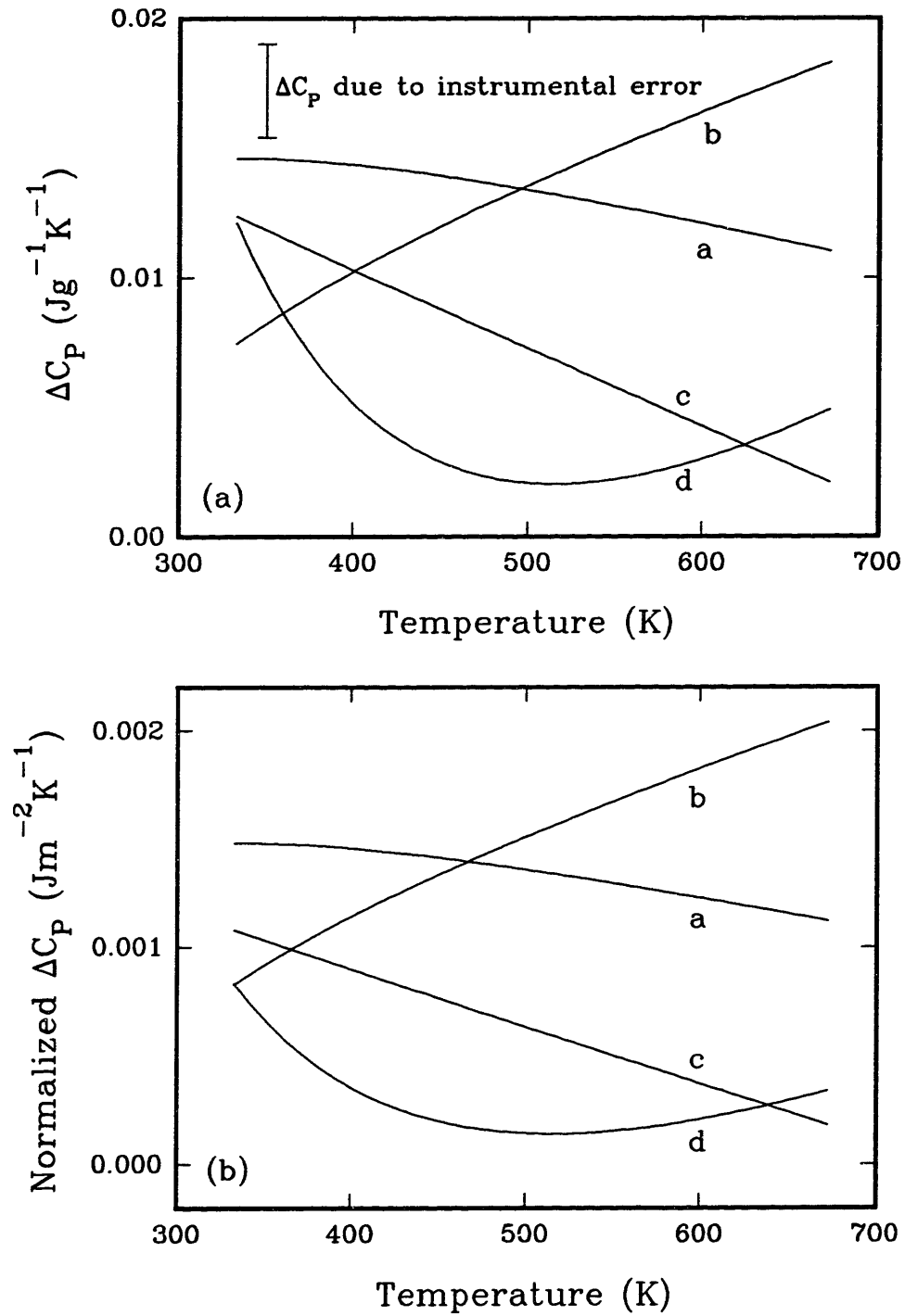
Figure 3.3. (a) Excess heat capacity, C_P^{nano}-C_P^{coarse} in units of $Jg^{-1}K^{-1}$, of the four samples (a,b,c,d) shown in Fig. 3.2(a,b,c,d) respectively. The error bar indicates the magnitude of ΔC_P which may be due to instrumental error. (b) Excess heat capacity of the same four samples, normalized to the change in grain boundary area. Thus, the units of ΔC_P are now $Jm^{-2}K^{-1}$.

difference in grain boundary area between their nanocrystalline and coarsened structures (ΔS_V) is larger than those of samples (a) and (b). Indeed, a more meaningful comparison between samples is made after normalizing for the change in grain boundary area between the first and second heat capacity measurements. The excess heat capacity at a particular temperature is then calculated as:

$$\Delta C_P \ (Jm^{-2}K^{-1}) = \frac{C_P^{nano} - C_P^{coarse}}{S_V^{nano} - S_V^{coarse}} \tag{3-4}$$

where S_V is the grain boundary area (m^2/g) measured by TEM. Figure 3.3(b) replots the ΔC_P data normalized to change in grain boundary area; variation of ΔC_P between samples is still observed.

The excess heat capacity due to grain boundaries can be used to predict the temperature dependence of H_{gb} by applying the fundamental relation:

$$H_{gb}^{T_2} = H_{gb}^{T_1} + \int_{T_1}^{T_2} \Delta C_P(T) \, dT. \tag{3-5}$$

Figure 3.4 compares our direct measurements of H_{gb} as a function of temperature (Chapter 2) with the temperature dependence of H_{gb} predicted by the four measurements of excess heat capacity shown in Fig. 3.2. The measurement of H_{gb} (670°C)$= 0.5$ J/m^2 has been chosen as the reference point, $H_{gb}^{T_1}$ in Eq.3-5. The main point to be made from Fig. 3.4 is that the H_{gb}-T relation predicted by the largest ΔC_P measurement is still not as steep as the temperature dependence indicated by direct measurements of H_{gb}.
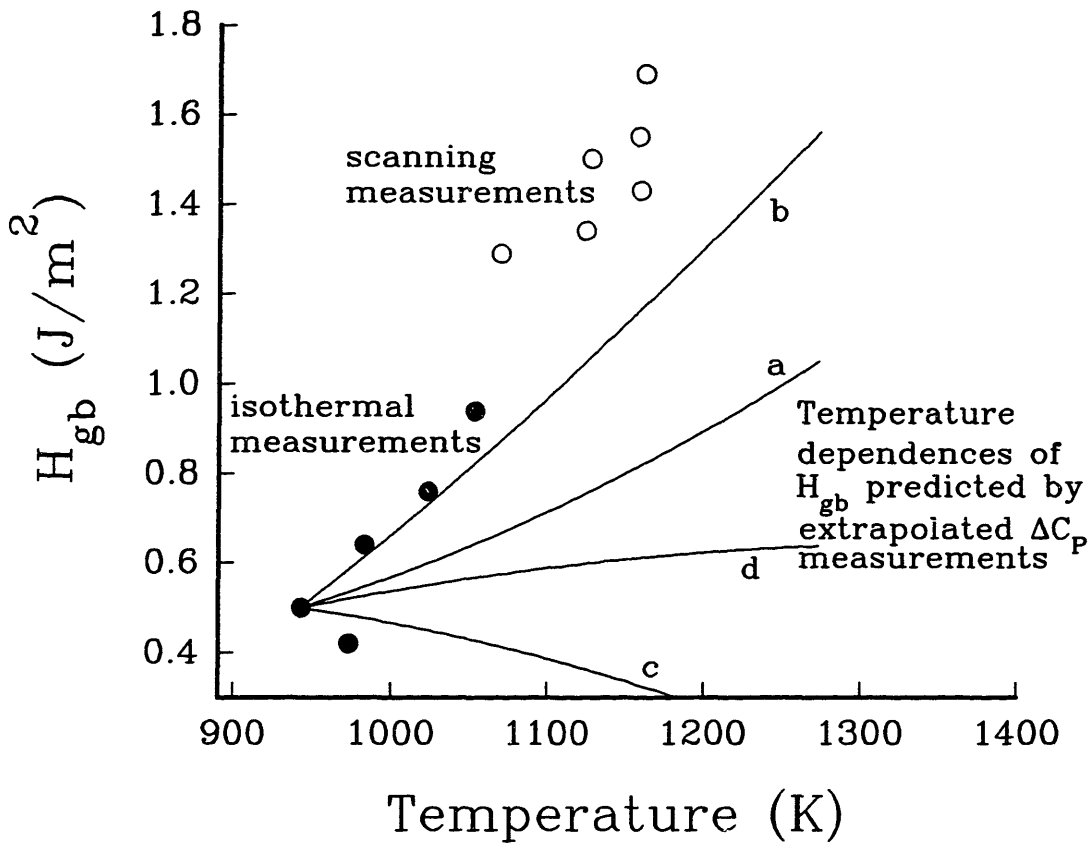
Figure 3.4. Specific grain boundary enthalpy as a function of temperature, as measured directly by isothermal and scanning DSC measurements (●,○), and as predicted by the four measurements of excess heat capacity. A grain boundary enthalpy of 0.5 J/m^2 at 670°C has been chosen as a reference point for the calculations using heat capacity.

3.5 DISCUSSION

First it should be emphasized that, consistently (including a number of samples not shown in Fig. 3.2), a positive excess heat capacity due to grain boundaries has been measured in the 50-400°C temperature range which, in and of itself, indicates a temperature dependence of the grain boundary enthalpy and entropy; these thermodynamic values are often assumed to be invariant with temperature in many different types of studies. But two other observations remain to be discussed: the considerable variation of ΔC_P ($Jm^{-2}K^{-1}$) between samples and the apparent inconsistency, as illustrated in Fig. 3.4, between direct measurements of H_{gb} as a function of temperature (Chapter 2) and the temperature dependence predicted by these ΔC_P measurements.

Regarding the variation in ΔC_P between samples, recall that ΔC_P is the difference in heat capacity measurements of two microstructures; the first measurement is of a 30-60 nm grain size sample that has been equilibrated at 500°C, and the second measurement is of the same sample but with a larger grain size obtained by a scan to 1300°C or an anneal at an intermediate temperature. Thus, ΔC_P at temperature T (50-400°C) can be expressed as:

$$\Delta C_P^T = C_P^T(\overline{D}_1, T_1^* = 500° C) - C_P^T(\overline{D}_2, T_2^*) \tag{3-6}$$

where $\overline{D}_1$ and $\overline{D}_2$ are the sample's mean grain size during the first and second C_P measurements, and T_2^* is the ultimate temperature to which the sample was exposed prior to the second C_P measurement, which varies from 670° to 1300°C. Since the ΔC_P measurements shown in Figure 3.3(b) have already been normalized to the change in grain boundary area, the variation in ΔC_P between samples may very well stem from changes in grain boundary or bulk structure with temperature (T_2^*) or grain size ($\overline{D}_1, \overline{D}_2$). One such change may be due to oxidation, if there is an

intrinsic size-dependent nonstoichiometry of TiO_2, as discussed in Chapter 2. The

extent of oxidation would tend to increase with T_2^*, and the excess heat capacity

(due to contributions from grain boundaries and point defects) would vary

accordingly. Oxidation would increase the *difference* in heat capacity which is

measured here, since the heat capacity of the initial, reduced structure would be

larger due to its higher defect concentration. Alternatively, the contribution of grain

boundaries to the total excess heat capacity may vary with $\bar{D}_1$, $\bar{D}_2$, or T_2^* if there is

an irreversible change in structure of the average grain boundary with grain size or

temperature. **

Regardless of the source of variations in the ΔC_p measurements, the excess

enthalpy and excess heat capacity measurements, ideally, should be self-consistent;

that is, the temperature dependence of H_{gb} predicted by ΔC_p measurements should

correspond to that indicated by direct measurements of H_{gb}. (For example, if

oxidation contributes to the steep temperature dependence of H_{gb}, ΔC_p should

increase correspondingly such that the same temperature dependence is predicted.)

Thus, the fact that the enthalpy and heat capacity measurements are *not* self-

consistent (Fig. 3.4) is noteworthy, and at least two explanations can be postulated.

First, it is possible that any structural or chemical changes responsible for the higher

H_{gb}'s measured in-situ at high temperatures are not preserved upon cooling, and

thus are not reflected in the low temperature heat capacity measurement of the

coarsened microstructure. Second, recall that, of necessity, the heat capacity

measurements were terminated at 400-500°C to avoid the onset of grain growth, yet

the measurements of H_{gb} occurred at temperatures between 670-1300°C. Thus, the

---

** There is a subtle but important distinction to be made between the fundamental variation
in grain boundary heat capacity with temperature due to *reversible* changes in boundary
structure (for example, due to thermal expansion) and the effect that T_2^* may have in
introducing variation in our measured ΔC_p's due to *irreversible* changes in boundary
structure with temperature or grain size.

63

comparison of Fig. 3.4 is based on an extrapolation of the ΔC_P measurements to much higher temperatures than at which they were made. (The potential perils of such extrapolation are illustrated by sample (c) in Fig. 3.4, whose ΔC_P-T function extrapolates to negative values beyond the temperature range of the C_P measurement.) An average grain boundary heat capacity that increases abruptly at temperatures $> 500°C$ would also explain the inconsistency between ΔC_P and H_{gb} measurements illustrated in Fig. 3.4.

In the final analysis, these measurements of excess heat capacity do little to further our understanding of the size/temperature-dependent H_{gb} reported and discussed in Chapter 2, due primarily to the limitations of the ΔC_P measurements just discussed (limited temperature range, unquenched samples). The intrinsic grain boundary heat capacity cannot be separated from a possible contribution due to composition changes. However, the magnitude of the largest ΔC_P's measured renders it unlikely that the intrinsic grain boundary heat capacity was the sole contribution in those samples.

3.6 SUMMARY

An excess heat capacity of ultrafine-grained TiO_2 relative to coarser-grained TiO_2 has been measured in many samples. Much of this excess heat capacity $(Jg^{-1}K^{-1})$ is due to the larger amount of grain boundary area in the ultrafine-grained samples, and its measurement implies a temperature dependence of both the grain boundary enthalpy and entropy. After being normalized for the change in grain boundary area, a variation in the magnitude of ΔC_P $(Jm^{-2}K^{-1})$ between samples remains, which suggests that differences in composition or grain boundary structure between fine and coarse microstructures may also affect the excess heat capacity. Furthermore, the fact that the ΔC_P measurements under-predict the temperature

dependence of H_{gb} reinforces the likelihood of either a change in defect chemistry or boundary structure at high temperatures that is not preserved upon cooling, or of an abrupt change in grain boundary heat capacity at temperatures beyond the 50-500°C range in which it was measured.

CHAPTER 4

SIZE-DEPENDENT SOLUTE SEGREGATION PHENOMENA IN ULTRAFINE POLYCRYSTALS: Ca IN TiO$_2$

4.1 INTRODUCTION

The segregation of solute to grain boundaries in single phase materials and resultant changes in fracture behavior, corrosion, grain growth kinetics, and other transport phenomena are well documented.[1-4] Thus it is not surprising that given the recent interest in nanocrystalline materials,[5,6] solute segregation to internal interfaces is being explored as a means of engineering structure, composition, and properties to a greater extent than is possible in conventional coarse-grained materials. For example, one consequence of the large number of grain boundary sites in fine-grained materials should be an enhancement in total solid solubility due to grain boundary segregation. This effect was discussed many years ago by McLean[7] and has been qualitatively observed in a number of nanocrystalline metals.[8-11] Solute segregation is also being used with some success to stabilize ultrafine-grained structures to higher temperatures.[11-17]

For Gibbsian adsorption of solute at interfaces in coarse-grained materials, temperature and composition are the principal variables influencing the excess solute at the interface. In ultrafine-grained materials, deviation from this conventional behavior is expected since the number of surface or boundary sites is not negligible in comparison to the number of bulk sites.* Using a statistical thermodynamical model which considers the large number of boundary sites in small crystals, Colbourn et al[18] predicted that segregation would deviate from conventional

---

* A rough calculation illustrates this point: if all solute were to segregate to boundaries, only about 100 ppm would be sufficient to fill all grain boundary sites in TiO$_2$ at a grain size of 10 μm, whereas approximately 2 mole% would be required at a grain size of 50 nm.

isotherms and exhibit a size dependence. For ionic systems in which space-charge segregation is also important,[2,3,19,20] deviations from ideality at ultrafine grain sizes are expected not only due to the excess of grain boundary sites and limited aliovalent solute concentrations, but due to the confinement of space-charge fields as well.[21] In this chapter we consider the first of these issues; some of the implications of space charge confinement were discussed in Chapter 2.

Segregation in the fine grain size regime has been studied using Ca-doped TiO_2 and a STEM microanalysis technique, recently developed by Ikeda *et al*,[20,22] which enables the accurate quantification of solute coverage at grain boundaries. This work represents a clear, and possibly first, direct confirmation of size-dependent solute segregation phenomena at ultrafine grain sizes.

4.2 EXPERIMENTAL METHODS

4.2.1 Sample Preparation

TiO_2 powder, co-doped with Sn and Ca, was synthesized using the solution-chemical process described in section 2.2.1. Ca^{2+} was chosen as a dopant due to its large ionic size mismatch with Ti^{4+}, which results in a considerable elastic strain energy driving force for segregation. $CaCl_2 \cdot 6H_2O^*$ was used as the source of Ca^{2+}. Since calcium hydroxides are soluble in water, one modification to the precipitation step of the processing methodology was required. Ammonium oxalate was added to the aqueous solution of 7.4 M ammonium hydroxide, in an amount sufficient to precipitate all the Ca^{2+} in solution. Thus, the precipitates are expected to be an intimate mixture of titanium and tin hydroxides and calcium oxalate. Powders were calcined in air on platinum foil for one hour at 750°C. Chemical analysis of calcined powders was accomplished using inductively-coupled plasma

---

* Johnson-Matthey, Alfa Chemicals, Ward Hill, MA

emission spectroscopy (ICP),[**] the results of which are shown in Table IV-1 for three representative powders. The results reported herein are for samples made from powder batch 1 only (0.34 mole% Ca).

Powders were hot pressed as described in section 2.2.1, using a pressure of ~1.1 GPa and pressing time of 6 hours to achieve a density >95% of the theoretical value. Pellets were then annealed in air for 24 hours at 500°C. The mean grain size after this treatment was generally on the order of 50 nm, and samples were phase-pure rutile by x-ray diffraction.

4.2.2 Characterization of Grain Size and Internal Surface Area

The average grain size of nanocrystalline and coarsened samples was characterized directly from projected grain dimensions on TEM micrographs; a discussion of the details and critical assumptions of this method is contained in section 2.2.3. At the larger grain sizes (400-700 nm) overlap of grains through the

TABLE IV-1. Chemical analysis of (Ca+Sn)-doped TiO_2 powders prepared by co-precipitation of aqueous chloride solutions.

Batch	Composition (mole%)			
	Sn	Ca	Si	Cl
1	1.25	0.34	0.13	↑
2	1.20	1.31	0.12	32 ppm[†]
3	1.14	3.69	0.55	↓

†Measured by ion chromatography for a Sn-doped powder batch prepared identically.

[**] Dr. Walter Zamachek, Union Carbide Corp., Tarrytown, NY

foil thickness was still observed, but due to the possibility that grains were truncated, the maximum projected dimension is likely to underestimate the maximum dimension of the grain. However, due to the inverse grain size dependence of the area to volume ratio (shown below), errors at the larger grain sizes have little impact on our results and conclusions.

A quantitative treatment of size-dependent grain boundary segregation requires knowledge of S_V, the grain boundary area per unit volume, as a function of the grain size. The relation developed in section 2.2.3 is repeated here for clarity:

$$S_V = \frac{\text{grain boundary area}}{\text{total volume}} = \frac{3.5513}{\overline{D}} \exp\left[-2.5(\ln \sigma)^2\right] \qquad (4\text{-}1)$$

where $\overline{D}$ is the average of maximum grain dimensions and $\ln \sigma$ is the standard deviation of normalized grain dimensions, $\ln(D/\overline{D})$. In the Ca-doped samples, the size distribution correction factor was found to decrease from a value of ~ 0.86 at grain sizes on the order of 50 nm to ~ 0.7 at grain sizes of 400-700 nm. To enable smooth modeling of the dependence of segregation on grain size, the experimental data were fit to a continuous function:

$$\exp\left[-2.5(\ln \sigma)^2\right] \cong 0.45 \exp\left(-2.08 \cdot 10^{-2} \overline{D}\right) + 0.7 \qquad (\overline{D} \geq 50\text{nm}) \qquad (4\text{-}2)$$

where $\overline{D}$ is in nm. This function has no particular physical meaning, but describes the experimental grain size distribution data quite well. To model the size regime $\overline{D} < 50$ nm, the limiting value of 0.86 at $\overline{D} = 50$ nm was used. Figure 4.1 shows a TEM micrograph of as-prepared Ca-doped TiO_2, along with its grain size histogram and a cumulative probability plot, the linearity of which is indicative of a lognormal grain size distribution.
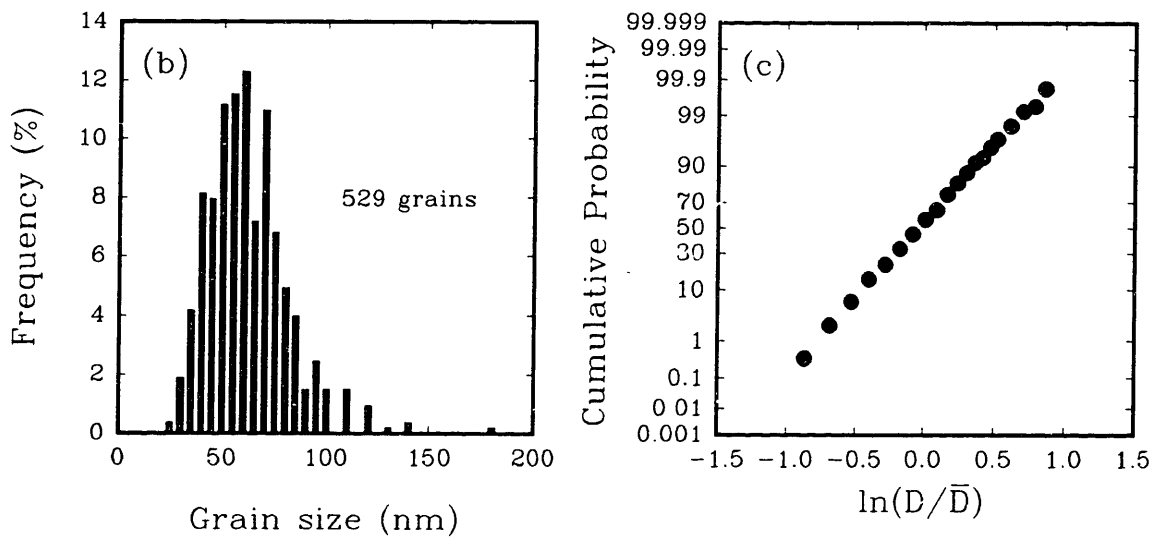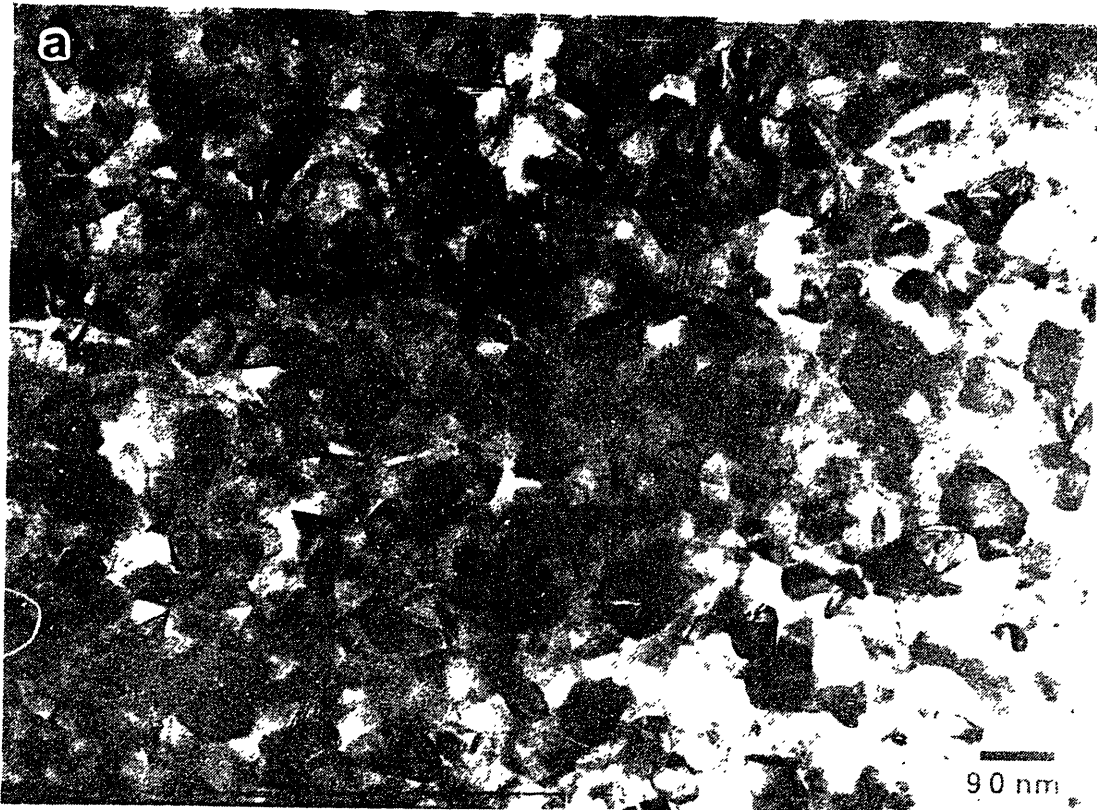
Figure 4.1. Bright field TEM image of an as-prepared Ca-doped TiO$_2$ sample along with its grain size histogram. The linearity of the cumulative probability versus ln(normalized grain size) plot indicates a lognormal distribution.

4.2.3 STEM Microanalysis

A STEM microanalysis technique recently developed by Ikeda *et al*[20,22] was used to quantify the excess solute coverage at grain boundaries for as-prepared samples (grain size ~ 50 nm) and samples coarsened in a calorimeter using the heat treatments listed in Table IV-2. Measurements were made using a Vacuum

TABLE IV-2. Thermal history and resulting mean grain size of samples used for STEM measurements of excess solute coverage.			
Thermal history†			Mean grain size (nm)
Temp. (°C)	Time (hr)	Cooling*	
500	24	FC	51
900	0.5	FC	120
1000	2	FC	383
1000	2	WQ	509
1000	8	FC	477
1050	2	FC	731

†All samples were given an initial 500°C x 24hr anneal.
*FC=furnace cool inside a calorimeter (~ 20°C/min)
   WQ=water quench from a vertical tube furnace

Generators HB5* dedicated scanning transmission electron microscope operating at 100 kV and equipped with a Link Systems** thin window energy dispersive x-ray detector. X-ray spectra were collected in scanning mode from a reduced area raster (170 x 133 Å at a magnification of 2Mx) containing the grain boundary plane (see Figure 4.2). Only grain boundaries that were oriented parallel to the electron beam were selected. To characterize the bulk solute level, x-ray spectra were then collected from the same reduced area positioned at the center of each of the two

---

* Vacuum Generators, East Grinstead, U.K.
** Link Systems, now Oxford Instruments, Oak Ridge, TN.
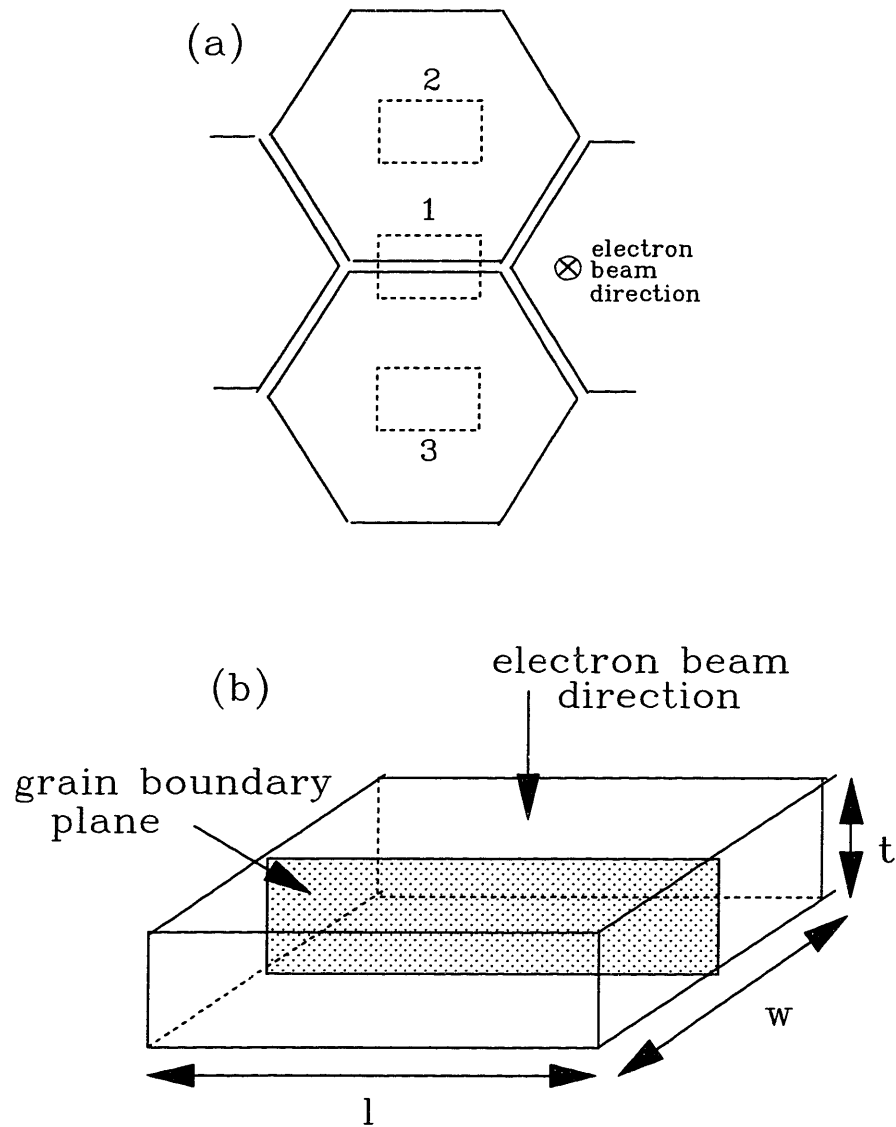
Figure 4.2. Schematic of the STEM microanalysis technique showing (a) location of the reduced area raster for the three x-ray spectra comprising a grain boundary solute coverage measurement, and (b) a cross-sectional view of the volume sampled by the electron beam.

neighboring grains. Spectra from large area scans (50-100kx) containing many grains and boundaries were used as an internal composition standard. To ensure adequate counting statistics, counting times sufficient to acquire 1.3×10^5 to 2×10^5 counts of the $\text{Ti}_{K\alpha}$ line were used. Typical spectra from a grain boundary and grain interior are shown in Figure 4.3.

Solute concentrations were quantified as follows. First, the integrated intensities of the three relevant peaks ($\text{Ti}_{K\alpha}$, $\text{Ca}_{K\alpha}$, $\text{Sn}_{L\alpha}$) were obtained after background stripping and deconvolution of the $\text{Ca}_{K\alpha 1}$ and $\text{Sn}_{L\alpha 2}$ peaks using reference spectra. Conversion of intensities into mole fraction requires knowledge of the "k-factor" for each element referenced to Ti, which can be calculated using the ratio method of Cliff and Lorimer:[23]

$$k_{Ti}^{i} = \frac{\left(\dfrac{C_i}{C_{Ti}}\right)^{ICP}}{\left(\dfrac{I_i}{I_{Ti}}\right)} \tag{4-3}$$

where i is either Ca or Sn, (C_i/C_{Ti}) is the overall composition determined by inductively-coupled plasma emission spectroscopy (Table IV-1), and (I_i/I_{Ti}) is the mean intensity ratio acquired from several large area scans averaging over many grains and boundaries. The mole fraction of solute at a grain boundary or within a grain is then given as:

$$C_i = k_{Ti}^{i} \cdot \frac{I_i}{I_{Ti}} \tag{4-4}$$

and the excess solute coverage at a particular grain boundary (atoms/cm^2) is calculated as:

$$\Gamma_i = \left(C_i^{gb} - C_i^{bulk}\right) \cdot \frac{N \cdot V}{A} \tag{4-5}$$
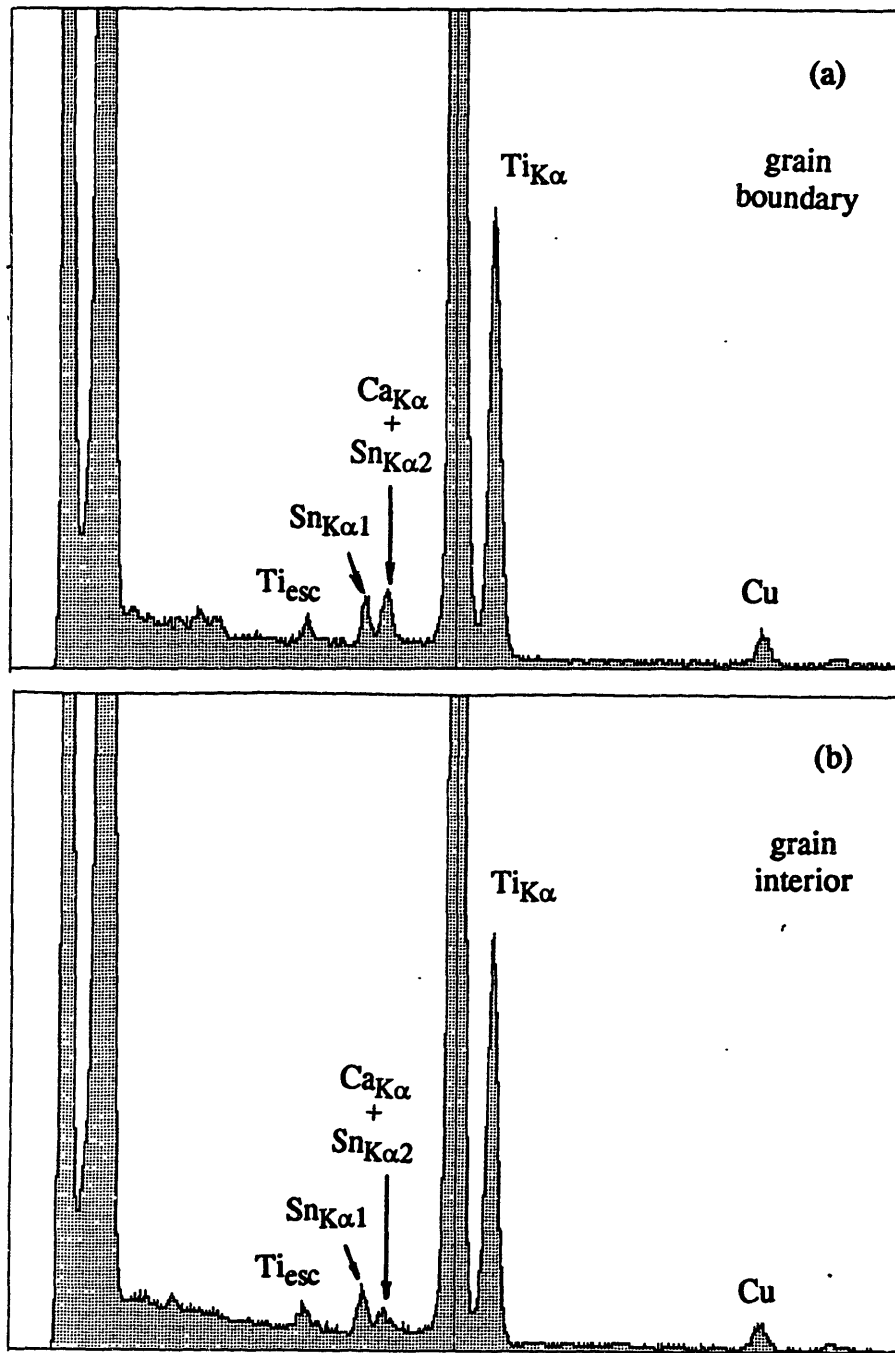
Figure 4.3. Examples of x-ray spectra collected from a) a grain boundary, and b) a grain interior.

where C_i^{bulk} is the average composition of the two neighboring grains, N is the cation site density (3.21×10^{22} cm^{-3} for rutile), V is the volume of material analyzed (l·w·t), and A is the boundary area analyzed (l·t). The thickness, t, of the foil thus drops out of the equation and does not need to be measured. It is shown in Appendix A that x-ray absorption corrections were not necessary for the characteristic lines of interest in the experimental foil thickness range (the thin film limit being ~950 nm). A calculation of the error due to counting statistics is also contained in Appendix A.

4.3 RESULTS

The results from STEM microanalysis are illustrated in Figure 4.4, plotted as mole% Ca in the analyzed volume, as a function of grain size. Quite clearly, calcium segregates strongly to grain boundaries, and the concentration in the grain boundary raster increases with increasing grain size. Furthermore, the bulk concentration of calcium is observed to be much lower than the overall doping level of 0.34 mole%, is frequently undetectable, and does not change significantly over the entire grain size range.

When the results in Figure 4.4 are reduced using Eq. 4-5 to show the coverage of Ca and Sn at grain boundaries (atoms/cm^2) as a function of grain size, Figure 4.5, a clear grain size dependence of calcium segregation is seen. Within the error limits, no segregation or depletion of tin is observed. The variations in solute coverage between different boundaries in the same sample (Fig. 4.4) were found to be within the counting statistics error of one another (see Appendix A), excepting special cases as discussed below. The solute density for each grain size shown in Figure 4.5 is an average of five boundary analyses. The error bars do not indicate the spread in the measurements, but rather, the average value of the 95% confidence

75
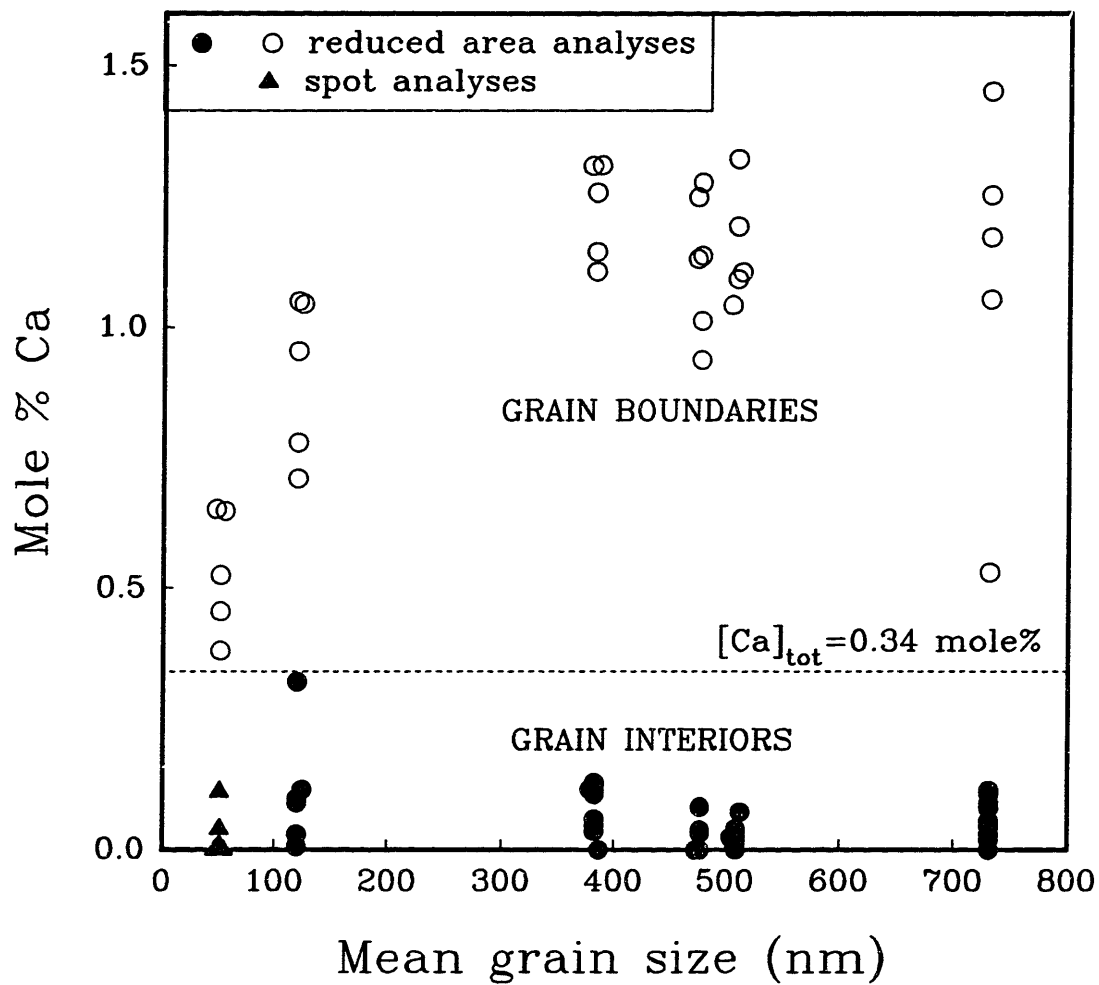
Figure 4.4. Calcium concentration within STEM-analyzed volume containing a grain boundary and within grains as a function of mean grain size. Each point represents the analysis of one boundary or grain. Some points are offset for clarity.
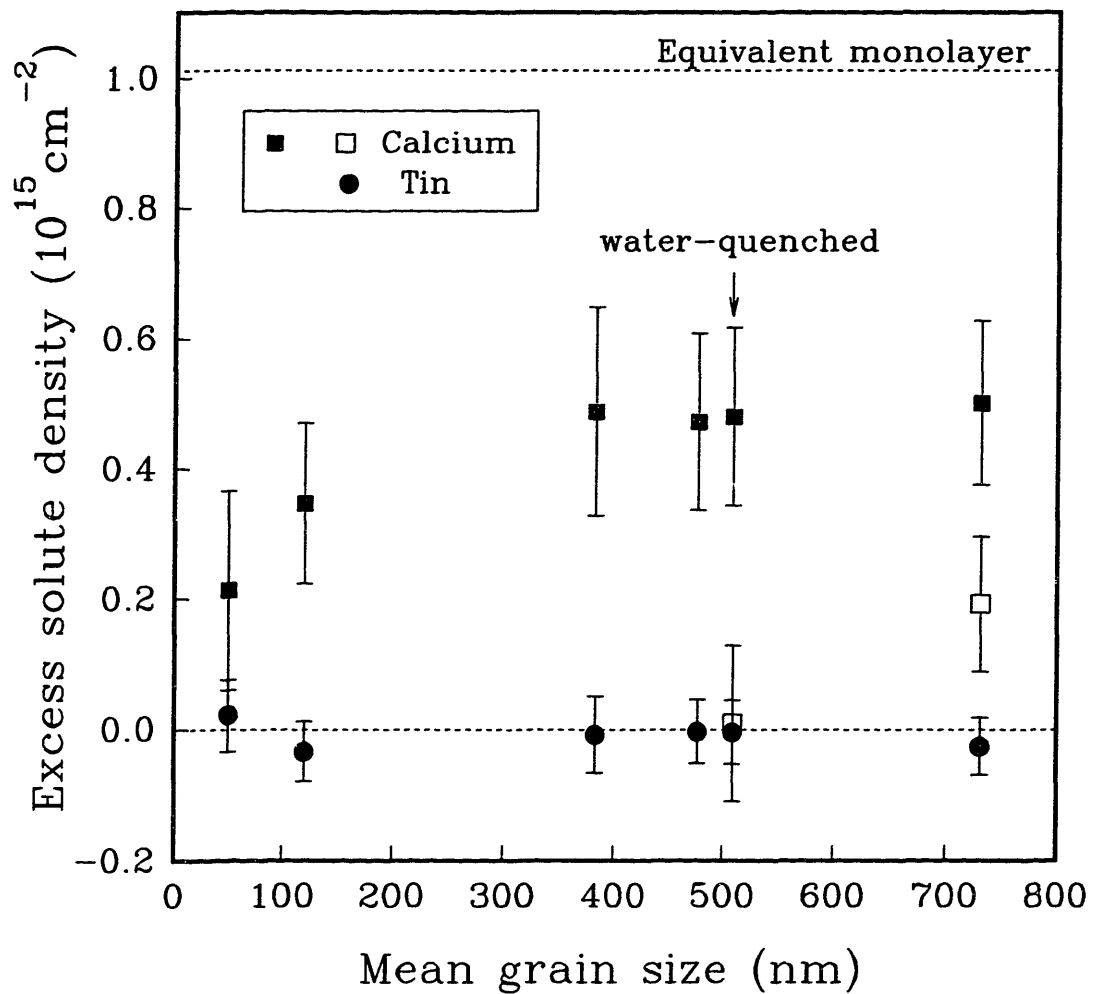
Figure 4.5. Excess solute density of Ca and Sn at grain boundaries in TiO$_2$ as a function of grain size. Each point represents the average of five measurements, with the error bars indicating the average 95% confidence level (see Appendix A). The open square symbols (□) represent two grain boundaries that showed a significantly lower level of calcium segregation.

interval for each datum.

Also included in Figure 4.5 are measurements for two boundaries in coarsened samples that showed a statistically significant lesser degree of calcium segregation. In their study of space charge segregation in coarse-grained (Al or Ga+Nb)-doped TiO_2, Ikeda *et al* found that approximately one in every ten boundaries showed no detectable segregation, and one of these was found to be a twin boundary.[20] Our two observations of anomalously low calcium segregation might also be due to the dependence of segregation on boundary structure. These data points have not been included in the averaged Γ values since they lie many standard deviations outside the others. Not enough boundaries have yet been analyzed to determine accurately the fraction of "special" boundaries (which is perhaps a function of grain size) in these samples. If, however, this fraction is on the order of 10% as measured by Ikeda *et al* in coarser-grained samples of TiO_2, the overall trend of a size-dependent solute coverage would be largely unaffected by including these anomalous points in the average.

A monolayer of cation segregation at grain boundaries, assuming each cation site to be available for substitution by the solute, has an average value given by $N_v^{2/3}$, where N_v is the lattice cation site density. This monolayer level (1.01×10^{15} cm^{-2} for rutile) is shown in Figure 4.5. It is evident that as grain size increases, the excess calcium density not only saturates, but saturates at approximately one-half of an equivalent monolayer.

Unusual microstructural features were observed in one sample at a larger grain size of $\overline{D} = 509$ nm. Isolated $CaTiO_3$ precipitates were identified by STEM, providing clear evidence for exsolution upon coarsening. This result is consistent with a grain size-dependent total solid solubility, as will be discussed later. A second microstructural feature in this sample was the appearance of planar faults

78

within grains, an example of which is shown in Figure 4.6. STEM microanalysis indicated no calcium segregation at the faults. Furthermore, no difference in grain boundary coverage or calcium concentration within grains was observed between highly faulted and fault-free grains in this sample. The identity and formation mechanism of these faults is not presently known. They may be crystallographic shear defects of the type formed to accommodate oxygen deficiency in TiO_{2-x}. While intrinsic reduction would be negligible at these temperatures and in air,[24] Ca doping may provide the necessary defects since Ca in solid solution in TiO_2 must be charge compensated by oxygen vacancies and/or titanium interestitials. The incipient precipitation of $CaTiO_3$ may also help to nucleate these planar defects, whatever their identity.

4.4 DISCUSSION

4.4.1 Theory of Segregation in Fine Crystallites

Statistical thermodynamical methods have been widely used to model interfacial segregation.[7,25,26] Extension of the theory to small crystallites has been treated in the catalysis literature,[27] as well as by Colbourn, Mackrodt, and Tasker[18] whose treatment we follow here. The free energy of a multicomponent polycrystal can be expressed as:

$$G = \sum_i n_i^b g_i^b + \sum_i n_i^{gb} g_i^{gb} - kT \ln \Omega \qquad (4\text{-}6)$$

where k and T have their usual meaning, n_i^b and n_i^{gb} are the number of ions of species i in the bulk and at grain boundaries, respectively, and g_i^b and g_i^{gb} are the corresponding individual free energies of the ions in these positions. Contributions from vibrational entropy are neglected, and all boundary sites are assumed to be equivalent. The configurational entropy is given by:
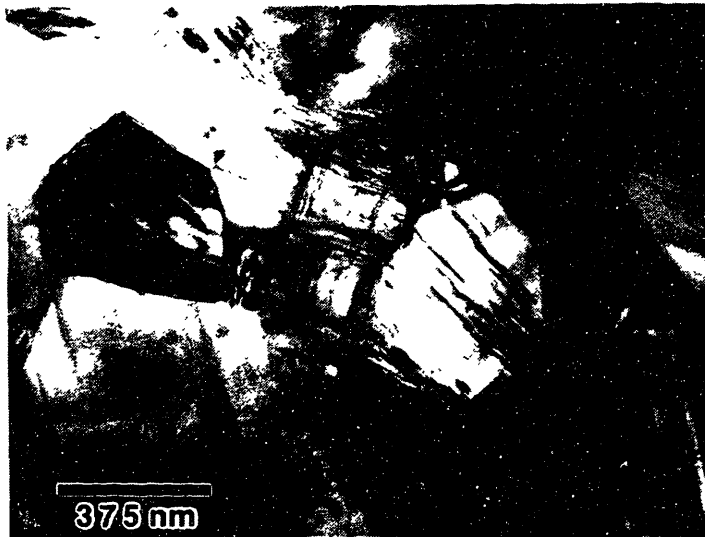
Figure 4.6. Bright-field TEM image of faults in coarse-grained TiO_2 ($\overline{D} = 509$ nm) doped with 0.34 mole% Ca.

$$\Omega = \frac{N_{gb}!}{\prod_i n_i^{gb}!} \cdot \frac{N_b!}{\prod_i n_i^b!} \qquad (4\text{-}7)$$

where N_b and N_{gb} are the total number of bulk and grain boundary sites. When the free energy is minimized subject to the following constraints for site and species conservation,

$$\sum_i n_i^b = N_b = \text{constant}$$

$$\sum_i n_i^{gb} = N_{gb} = \text{constant} \qquad (4\text{-}8)$$

$$n_i^b + n_i^{gb} = n_i = \text{constant}$$

one obtains

$$\frac{n_i^{gb}}{n_i} = \frac{1}{1 + \exp\left(\dfrac{g_i^{gb} - g_i^b - \lambda}{kT}\right)} \qquad (4\text{-}9)$$

where λ is a Lagrange multiplier ensuring site and species conservation, given by

$$\sum_i \frac{n_i}{1 + \exp\left(\dfrac{g_i^{gb} - g_i^b - \lambda}{kT}\right)} = N_{gb}. \qquad (4\text{-}10)$$

For coarse polycrystals, the number of grain boundary sites is small compared to the number of ions of the segregating species ($N_{gb} << n_i$); the bulk composition is largely unaffected by segregation of solute to grain boundaries. Using this simplifying assumption for a two component system (with component 1 as the segregating species), Eqs. 4-9 and 4-10 reduce to the familiar Arrhenius expression:

$$\frac{n_1^{gb}}{n_2^{gb}} = \frac{n_1}{n_2} \exp\left(\frac{-H}{kT}\right) \qquad (4\text{-}11)$$

where H is the heat of segregation given by

$$H \approx \left(g_1^{gb} - g_1^b\right) - \left(g_2^{gb} - g_2^b\right) \qquad (4\text{-}12)$$

81

if changes in vibrational entropy upon segregation can be neglected. Equation 4-11 can be rearranged to solve for the grain boundary concentration:

$$\frac{n_1^{gb}}{N_{gb}} = \frac{(n_1 / n_2) \cdot \exp(-H / kT)}{1 + (n_1 / n_2) \cdot \exp(-H / kT)}. \qquad (4\text{-}13)$$

This equation can be compared directly with the result of McLean:[7]

$$C_{gb} = \frac{C_b \exp(Q / kT)}{1 + C_b \exp(Q / kT)} \qquad (4\text{-}14)$$

where C_{gb} and C_b are the grain boundary and bulk concentrations in mole fraction, and Q is the difference in energy for a solute atom in the bulk versus at a grain boundary.* The derivation of Eq.4-14 includes the assumption that $C_b << 1$. (In our notation, $n_1^{gb}/N_{gb}=C_{gb}$ and $n_1^b/N_b=C_b$.) Thus, it can be seen that the two results are equivalent if $n_1/n_2 \approx n_1^b/N_b$, which is the case for large grain sizes where the number of solute ions segregated to boundaries is negligible compared to those remaining in the bulk.

As grain size decreases, the total number of grain boundary sites increases to where they are no longer negligible in comparison to the available number of segregant ions. Under these conditions, Eqs. 4-9 and 4-10 can be solved explicitly to give grain boundary coverage as a function of grain size. Colbourn et al do so by defining a new variable,

$$y = \exp\left(\frac{g_2^{gb} - g_2^b - \lambda}{kT}\right), \qquad (4\text{-}15)$$

which allows simplication of Eq. 4-11 to

$$\frac{n_1}{1 + y\exp\left(\frac{H}{kT}\right)} + \frac{n_2}{1 + y} = N_{gb}(D). \qquad (4\text{-}16)$$

---

* Note that H and Q as defined by Colbourn et al[18] and McLean,[7] respectively, have opposite sign conventions; a negative H or positive Q indicates enrichment of solute at grain boundaries.

82

Assuming an appropriate model for the variation in $N_{gb}(D)$, the total number of boundary sites as a function of grain size, one can solve Eq. 4-16 for y as a function of grain size. The size-dependence of segregation can then be calculated from Eq. 4-9, now written more simply as:

$$n_I^{gb}(D) = \frac{n_1}{1 + y(D)\exp\left(\dfrac{H}{kT}\right)}.$$ (4-17)

For convenience in the calculations, we now define all sites and species (n_i, n_I^{gb}, N_{gb}) on a per unit volume basis. $N_{gb}(D)$ in Eq.4-16 is thus the total number of grain boundary sites per unit volume as a function of grain size, which we calculate as:

$$N_{gb}(D) \text{ (sites/cm}^3) = S_V(D) \text{ (cm}^2/cm^3) \cdot N_A \text{ (sites/cm}^2)$$ (4-18)

where $S_V(D)$, the grain boundary area per unit volume, is obtained from Eqs. 4-1 and 4-2. The grain boundary site density, N_A, is expressed as $m \cdot N_V^{2/3}$, where $m = 1$ may be considered to represent a full monolayer of adsorption. Size-dependent segregation under conditions where saturation of grain boundaries occurs at less than an equivalent monolayer is therefore modeled using $m < 1$.[*]

From the expression for $n_I^{gb}(D)$ in Eq. 4-17 we can calculate two quantities of interest. Experimentally, we measure the grain boundary solute coverage Γ_1 (cm^{-2}) as a function of grain size, which is equivalent to $n_I^{gb}(D)/S_V$ (D). A second quantity of interest is the fraction of solute ions segregated to grain boundaries, which can be calculated directly from Eq.28 as $n_I^{gb}(D)/n_1$. Figure 4.7(a) plots the

---

[*] A distinction should be made between conditions of saturation where all available boundary sites are occupied, as opposed to saturation where only a fraction of a larger number of available sites can be occupied at one time, for instance due to ion crowding. The present solution treats the former condition. For the latter an exact solution requires that the difference in configurational entropy, which is greater than that given by Eq. 4-7, be accounted for. This type of saturation could possibly also be modeled with a coverage-dependent heat of segregation.[28]
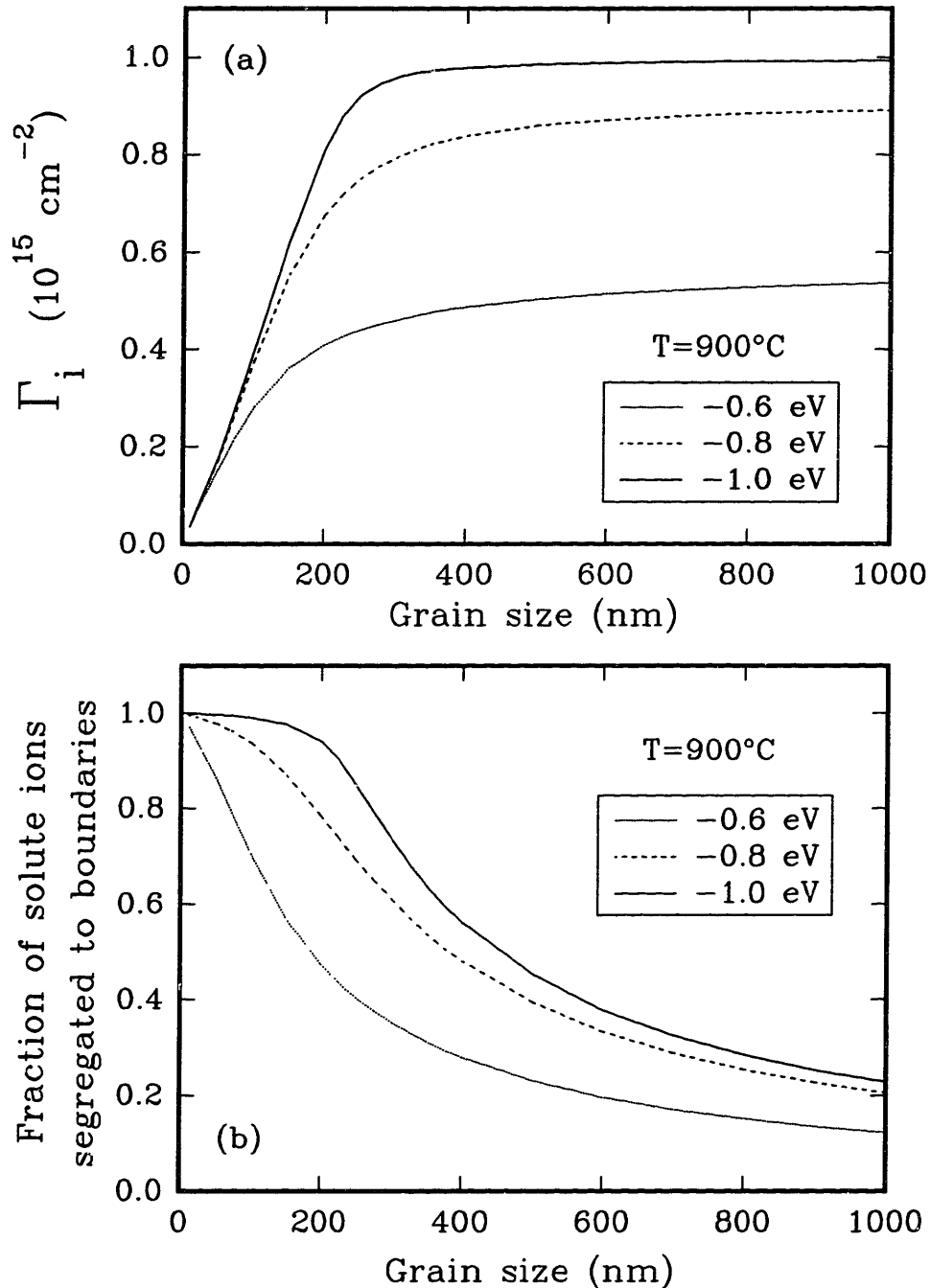
Figure 4.7. Calculations of size-dependent segregation following the theory of Colbourn *et al.* (a) Grain boundary coverage (solute ions/cm^2) as a function of grain size for three heats of segregation at 900°C, assuming the grain boundary site density to be $N_V^{2/3} = 1.01 \cdot 10^{15}$ cm^{-2}. (b) Fraction of the solute ions that are segregated to grain boundaries as a function of grain size. Note the nearly complete depletion of solute from the bulk at very fine grain sizes for all three heats of segregation.

solute coverage Γ_1 as a function of grain size, for various values of the heat of segregation at a constant temperature of 900°C. Figure 4.7(b) shows the corresponding fraction of solute that is located at the grain boundaries (n_i^{gb}/n_1) as a function of grain size. Notice that even for the smallest heat of segregation, theory predicts that the bulk is almost entirely depleted of solute at the finest grain sizes; solute atoms tend to fill the lower energy boundary sites up until saturation. Thus, the increase in Γ_1 with grain size is due to a decrease in boundary area rather than segregation of additional solute atoms to the boundary.

The heat of segregation for Ca in TiO_2 is approximately -1.1 eV, based on a calculation of the elastic strain energy due to cation size mismatch.[29] Figure 4.8 shows Γ_1 and n_i^{gb}/n_1 calculated as a function of grain size for this heat of segregation, our overall doping level of 0.34 mole%, and three of the annealing temperatures used in our experiments. For this relatively large heat of segregation, one sees that the transition from conventional behavior to size-dependent behavior is quite sharp. Below a grain size of ~200 nm, coverage is expected to drop linearly with grain size and the lattice is purged of solute. Figure 4.8 also shows that for a lower grain boundary site density (in this case $0.5N_V^{2/3}$), the boundaries saturate at a finer grain size and at the lower solute coverage.

A common feature of the segregation isotherms in Figs.4.7(a) and 4.8(a) is a threshold grain size below which segregation is size-dependent. This grain size is a function of the H/T ratio, the solute doping level, and the coverage of the boundaries at saturation. Along the plateau there exists a sufficient supply of solute to allow the boundaries to reach the equilibrium coverage predicted by conventional segregation isotherms. Below the threshold grain size, there is an excess of boundary sites relative to the supply of solute. This behavior is shown in a segregation map, Figure 4.9, which gives the threshold grain size as a function of
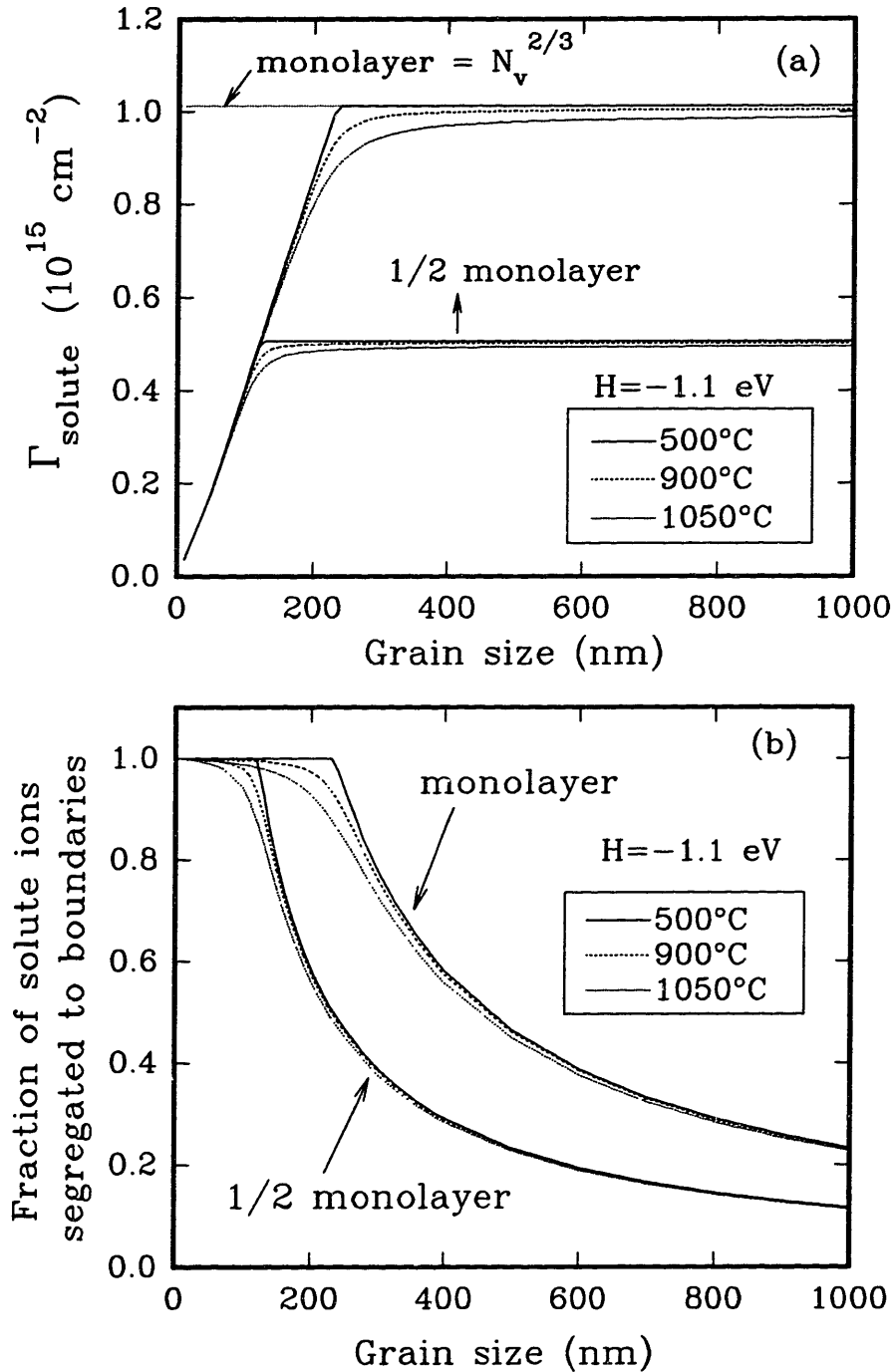
Figure 4.8. (a) Calculation of grain boundary solute density as a function of grain size for a heat of segregation of -1.1 eV and three temperatures. Also shown is the effect of a decrease in the grain boundary site density from $N_V^{2/3}$ to $\frac{1}{2}N_V^{2/3}$, resulting in saturation at half of an equivalent monolayer. (b) Fraction of the segregating species located at grain boundaries as a function of grain size and temperature for two limiting coverages.
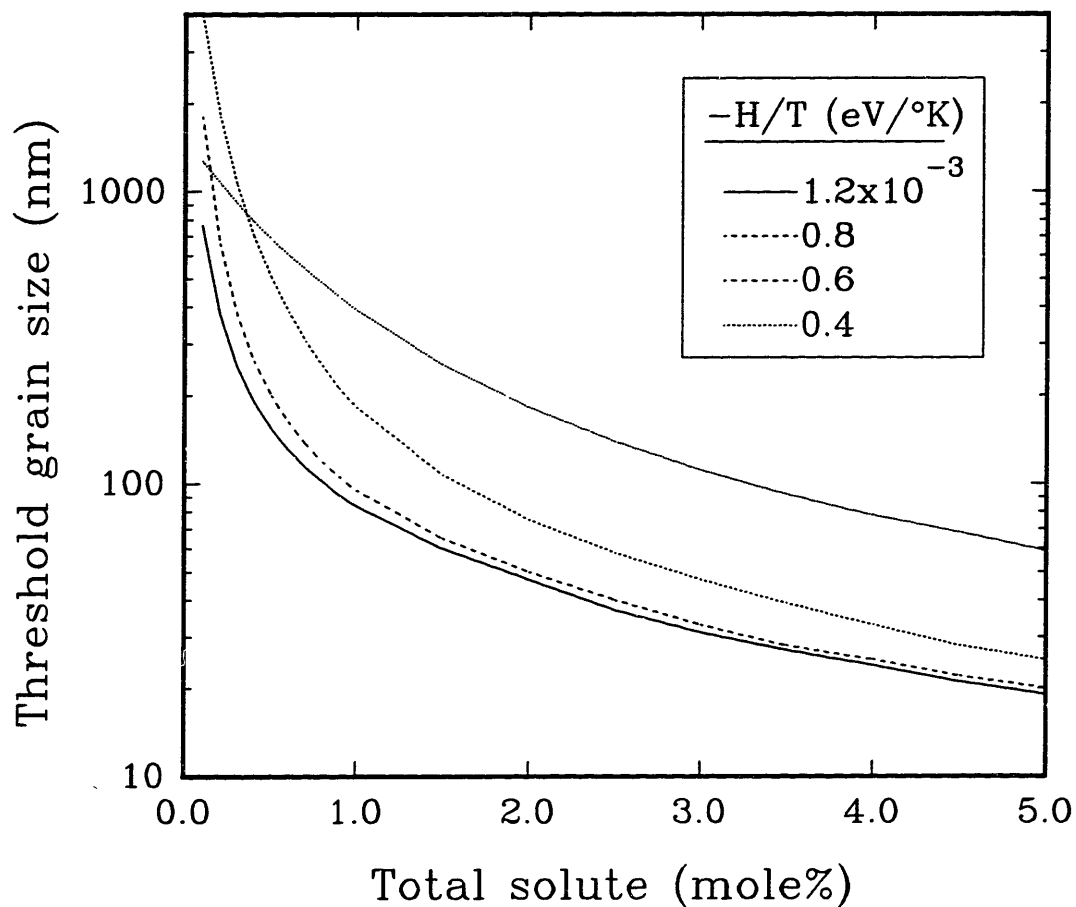
Figure 4.9. Segregation map showing the threshold grain size, below which segregation is size-dependent, as a function of the solute doping level and the ratio of heat of segregation to temperature. The region below each curve corresponds to a size-dependent segregation regime. The curves shown here are for a lattice site density of $3.21 \cdot 10^{22}$ cm^{-3} and a monolayer saturation level ($m=1$). They can be generalized to other site densities and saturation coverages using Eq.4-19 in the text.

doping level and H/T ratio. For the purposes of these calculations, the threshold grain size is defined as the size at which the coverage has reached 95% of the equilibrium value for an infinite crystal at the same H/T and overall doping level. The curves in Fig. 4.9 have been calculated using the lattice cation site density of rutile ($N_V = 3.21 \cdot 10^{22}$ cm^{-3}) and a monolayer saturation level. (Here we assume that the oxygen sublattice is invariant.) The critical grain size at other saturation coverages and in other materials can be calculated from the results in Figure 4.9 using:

$$D_c = D_c^* \cdot m \cdot \left(\frac{N_V (cm^{-3})}{3.21 \cdot 10^{22}} \right)^{-1/3} \tag{4-19}$$

where D_c^* is the threshold grain size in Fig. 4.9 at the doping level and (H/T) of interest, m is the saturation coverage (fraction of a monolayer), and N_V is the lattice site density of the compound of interest.

Figure 4.10 compares our experimental results for the size dependence of the calcium coverage at grain boundaries (Γ_{Ca}) with the above calculations. Saturation in Γ_{Ca} is observed with increasing grain size at slightly less than half of an equivalent monolayer; a grain boundary site density of $0.48 \cdot N_V^{2/3}$ yields the best fit to the data at large grain sizes. The good agreement between experiment and theory emphasizes the key and distinctive feature of grain boundary segregation in the nanocrystalline size range-- that below a threshold grain size, one is in an entirely different regime of behavior in which the effects of grain size can easily overwhelm those of temperature in determining the degree of segregation.

While saturation at a partial monolayer is observed here, it should be pointed out that multilayer Ca segregation is in principle possible if a broader range of Ca activity were accessible. However, even in the instance where $CaTiO_3$ precipitates were seen ($\overline{D} = 509$ nm), and the bulk Ca activity was clearly saturated at the
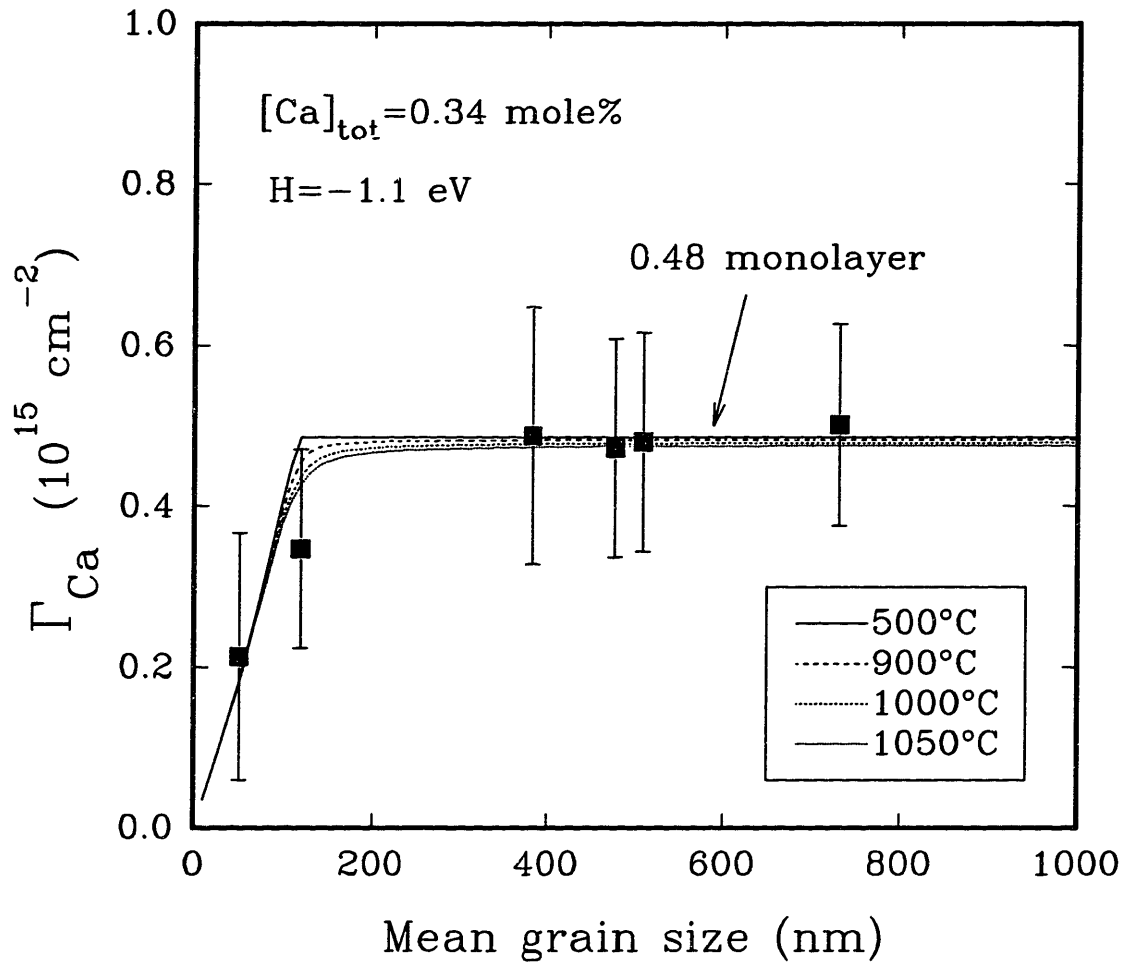
Figure 4.10. Experimental measurements of excess density of calcium at grain boundaries in TiO_2 as a function of grain size, along with the theoretical predictions for a heat of segregation of -1.1 eV and the four annealing temperatures used in our experiments. A grain boundary site density of $0.48 \cdot N_V^{2/3}$ was used in the calculation, consistent with the observed saturation of the boundaries at slightly less than half a monolayer.

phase boundary limit, the same grain boundary coverage (~0.5 monolayer) was observed. This supports the existence of a partial monolayer saturation level for the segregation of Ca in TiO_2, and shows that for the temperature range examined, equilibrium multilayer segregation does not occur for all Ca activities up to the solubility limit.

4.4.2 Thermal History Effects on Segregation

While most samples studied were furnace-cooled (~$20°$/min) from their annealing temperature (Table IV-2), no difference in segregation was observed between a sample that was water-quenched and those that were furnace-cooled. Upon examining the issue of segregation upon cooling, we find that it presents an interesting paradox. Because of the nature of segregation in the nanocrystalline regime, segregation of Ca upon cooling is of no concern at very fine grain sizes, while at "large" grain sizes (still < 1 μm) it is virtually impossible to avoid.

One arrives at the first of these conclusions in the following manner. Figure 4.8 shows that at very fine grain sizes and for large heats of segregation, the temperature dependence of equilibrium segregation is weak, providing little driving force for solute segregation upon cooling. Even so, were one at larger grain sizes, nonequilibrium multilayer segregation and incipient precipitation could occur upon cooling. However, since at fine grain sizes and sizeable heats of segregation virtually all solute ions are located at boundary sites (Figs.4.7(b), 4.8(b)), negligible solute is available within the bulk to segregate upon cooling. Thus, below the threshold grain size for a particular H, T, and doping level, segregation upon cooling does not occur, and the equilibrium distribution of solute is preserved.

At "large" grain sizes (in this case, ~400-700 nm), the effect of thermal history on segregation is entirely different. Figures 4.7(b) and 4.8(b) show that at equilibrium in this size range, a significant concentration of solute ions does exist

90

within the bulk, even for low temperatures and large heats of segregation. The diffusion lengths upon cooling from our annealing temperatures of 1000°C and 1050°C can be approximated using:[30]

$$L^2 \approx \frac{k_B D_a T_a^2}{\alpha Q} \qquad (4\text{-}20)$$

where k_B is Boltzmann's constant, α is the linear cooling rate, and D_a and Q are the diffusion coefficient and activation energy for diffusion of solute in the lattice. For estimation purposes we have used the lattice self-diffusion of Ti in TiO_2,[31] for which $Q=2.9$ eV and $D_a\sim 6.5\cdot\exp(-Q/k_B T_a)$ cm^2/s. These estimated diffusion lengths upon cooling exceed a sizeable fraction of the grain size, even when using a water quench ($\alpha \sim 500°/sec$). Thus, at the larger grain sizes the equilibrium distribution of solute is unquenchable at current cooling rates, and segregation of solute from the bulk upon cooling cannot be avoided. The fact that the calcium concentration measured within the grains (Fig.4.4) does not increase with grain size as predicted by the model (Fig.4.7(b),4.8(b)) is consistent with some segregation upon cooling at the larger grain sizes. A check for mass balance in the coarser samples shows that use of the measured grain boundary coverage Γ (cm^{-2}), the boundary area per unit volume S_V, and the STEM-detected lattice concentration of Ca is insufficient to account for the total Ca concentration of 0.34 mole%, which also indicates exsolution of $CaTiO_3$ upon coarsening.

4.4.3 Enhanced Total Solid Solubility at Fine Grain Sizes

McLean recognized that one implication of solute segregation to internal interfaces should be an increase in the equilibrium total solid solubility above the lattice solubility limit.[7] The present measurements of calcium segregation along with observations of $CaTiO_3$ precipitation upon coarsening support such a mechanism of solubility enhancement. Results in powder batch #3 (Table IV-1),

which contains 3.69 mole% Ca, are additional support for this mechanism of enhanced solubility. $CaTiO_3$ precipitation within this powder was detected by x-ray diffraction after a long grain coarsening anneal at 800°C. Increased solubilities have also been reported for numerous mechanically-alloyed and inert gas-condensed nanocrystalline metal alloys,[8-10] but it is not always clear whether these are equilibrium solubilities. It has been suggested that one possible contribution is grain boundary segregation;[8] however, other mechanisms for solubility enhancement may be operative, for example a size-dependent lattice solubility due to residual strain. Here we restrict discussion to solubility enhancement due to grain boundary segregation, an equilibrium phenomenon which assumes that the lattice solubility does not change in this size range.

The total solid solubility in mole fraction is the sum of the lattice solubility (C_b^*) and the grain boundary solubility, which is a function of the interfacial area/volume ratio (S_V) and the grain boundary site density (N_A), assuming an infinite source of solute:

$$C_{total} = \frac{C_b^* N_V + C_{gb} S_V N_A}{N_V} \qquad (4\text{-}21)$$

where the equilibrium dependence of C_{gb} on C_b is determined by McLean's relation (Eq. 4-14). In the present system the grain boundary coverage is known, but the bulk solubility is not. Thus we have assumed for purposes of illustration a value of 100 ppm at 500°C and 1900 ppm at 1000°C (corresponding to a heat of solution of 0.5 eV). The result is shown in Figure 4.11 for the H=-1.1 eV and the one-half monolayer saturation level of our system. A 500-fold and 25-fold increase in total solubility is predicted upon decreasing grain size from 1 μm to 10 nm at 500°C and 1000°C, respectively. This enhancement would double if a full monolayer of solute segregation were allowed. For this large heat of segregation, the total solid
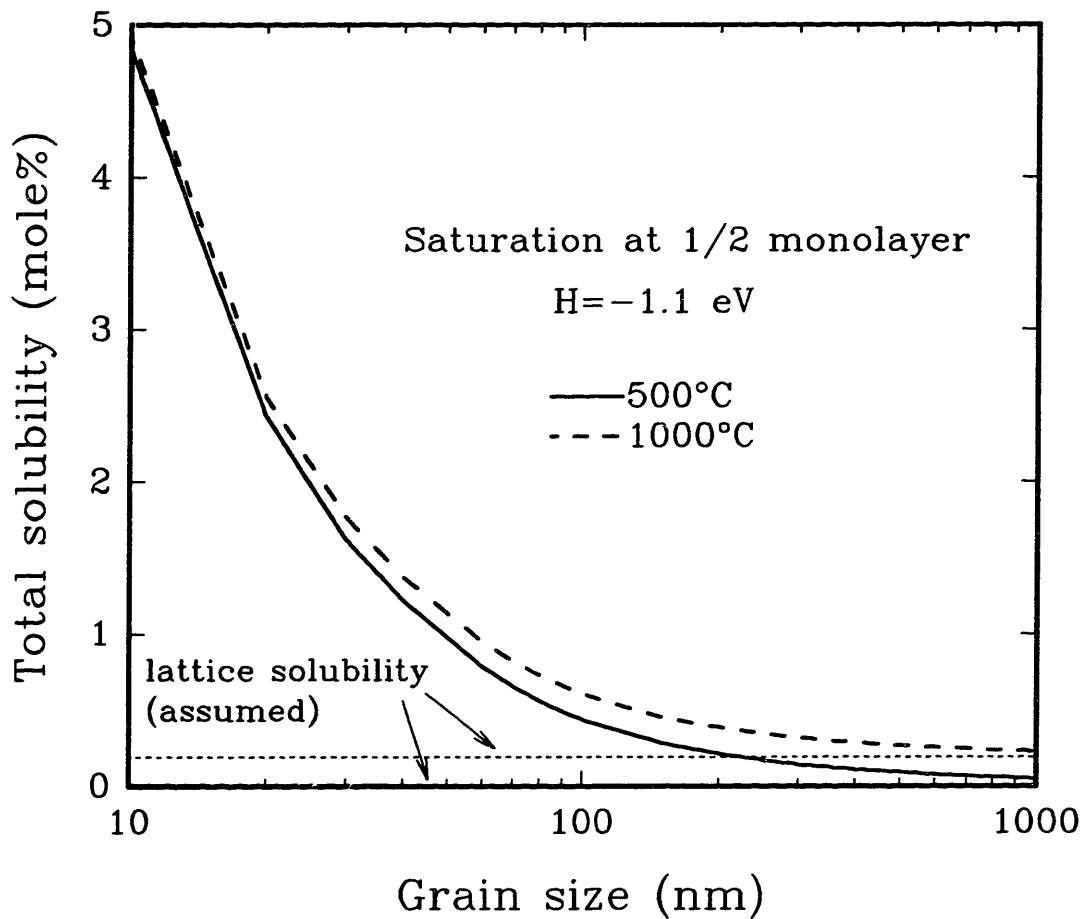
Figure 4.11. Total solubility as a function of grain size at 500 and 1000°C, calculated assuming a lattice solubility of 100 ppm and 1900 ppm, respectively, and grain boundary saturation at one-half of an equivalent monolayer.

solubility is a much stronger function of grain size than of temperature in this grain size range.

As a final comment, the present work shows that size-dependent segregation is an important phenomenon at very fine grain sizes and consequently can be either a boon or a bane for engineering and controlling material properties. On one hand, this phenomenon may be an important factor in development of novel nanocrystalline materials, such as extended solid solutions of normally immiscible elements. However, we have seen that small changes in grain size in the nanocrystalline regime result in quite large changes in solute coverage at grain boundaries for constant overall composition. Many properties, most notably mechanical and electrical, that are sensitive to grain boundary composition will thus be size-dependent in this grain size range. This reality can be viewed as an opportunity to "tune" materials to the needs of specific applications or as a challenge in the attempt to provide materials with predictable and stable properties.

4.5 SUMMARY

A STEM microanalysis technique has been used to make quantitative measurements of excess solute coverage at grain boundaries as a function of grain size in fine-grained Ca-doped TiO_2. Calcium segregates strongly to grain boundaries, and this segregation deviates from conventional behavior below grain sizes of 200-400 nm, exhibiting a strong size dependence. The bulk is almost entirely devoid of calcium in the as-prepared nanocrystalline state (~ 50 nm). With increasing grain size, the excess calcium density at grain boundaries increases, but this is due to a decrease in boundary area rather than the segregation of additional solute from the bulk. At a grain size of ~ 400 nm, the boundaries have become saturated, at approximately half of an equivalent monolayer of Ca, and upon

94

increasing grain size to ~500 nm, a few $CaTiO_3$ precipitates are observed. The experimental observations are modeled using a statistical thermodynamical treatment of grain boundary segregation which accounts for the large number of grain boundary sites in a nanocrystalline material. A generalized segregation map showing the threshold grain size, below which segregation is size-dependent, is calculated as a function of doping level, heat of segregation, temperature, and saturation coverage. The equilibrium enhancement of total solid solubility due to grain boundary segregation is demonstrated. The size-dependent segregation phenomena illustrated herein are expected to have implications for the processing, structure, transport phenomena, and mechanical properties of ultrafine-grained materials.

CHAPTER 5

GRAIN GROWTH INHIBITION FROM CALCIUM ADDITIONS
TO ULTRAFINE-GRAINED TiO$_2$

5.1 INTRODUCTION

The addition of solutes to nanocrystalline materials has become a common strategy among efforts to extend their stability to higher temperatures.[1-8] When success has been achieved, it has been attributed at least in part to conventional solute drag and Zener drag mechanisms, as well as to other factors not directly related to impurity effects, including an additional drag force due to triple junctions,[7-10] and a decrease in interfacial energy with decreasing grain size.[11] One issue that has not often been discussed is the distinctive nature of solute segregation in the nanocrystalline regime. The STEM microanalysis results discussed in Chapter 4 confirm that below a threshold grain size there is a deviation from conventional segregation isotherms due to the excess of grain boundary sites relative to a limited source of solute ions, which results in a size-dependent grain boundary coverage in this size range. One of the primary repercussions of this departure from ideality is expected to be size-dependent grain boundary properties in the nanocrystalline regime. In particular, if grain boundary migration is limited by solute drag, the boundary mobility should decrease with increasing grain size. Size-dependent segregation may be the source of a size-dependent grain boundary energy as well.

This chapter reports on our efforts to inhibit grain growth in ultrafine-grained TiO$_2$ and describes the use of differential scanning calorimetry (DSC) to measure the enthalpy release rates of Ca-doped and Ca-free samples. These grain growth exotherms are analyzed to give information about the kinetics of grain growth, using methods developed by Chen and Spaepen.[12] We then seek to make

qualitative correlations between the results of the DSC measurements and the size-dependent segregation observed by STEM.

5.2 EXPERIMENTAL METHODS

Sn-doped and (Ca+Sn)-doped TiO_2 powders were synthesized and consolidated into pellets as described in sections 2.2.1 and 4.2.1. Grain growth exotherms were measured at heating rates of $10\text{-}40°/min$, using the same procedures outlined in section 2.2.2. As will be described in section 5.4, proper use of the Kissinger analysis to determine activation energy from the shift in peak temperature with heating rate requires that all parameters other than heating rate be identical. Because peak position is sensitive to initial grain size, ideally all DSC runs should be conducted using pieces of the same sample. Since the diameter of the DSC sample pan and our self-imposed requirement for highly dense samples limited pellet mass to < 110 mg, cutting a pellet into four pieces would have resulted in an unacceptably high noise level due to a small DSC signal. Thus, two pellets were prepared using identical conditions of temperature, time, and pressure, and each was divided in half for the Kissinger analysis measurements.

The mean grain size of samples before and after grain growth was characterized by transmission electron microscopy (JEOL 200CX), using the procedure and assumptions described in section 2.2.3. A possible underestimate of the grain size for sizes > 100 nm is considered during analysis of our results and does not affect the overall conclusions.

5.3 GRAIN GROWTH INHIBITION

A comparison of the grain growth exotherms of a Sn-doped and a (Ca+Sn)-doped sample, each with an initial grain size of about 50 nm, is illustrated in

Figure 5.1. While enthalpy release in the two samples begins at approximately the same temperature (that of hot pressing), the onset is more gradual in the Ca-doped sample. In addition, its peak is slightly lower in magnitude and shifted to a higher temperature. These differences indicate that the addition of calcium at the level of 0.34 mole% inhibits grain growth in nanocrystalline TiO_2. This conclusion is reinforced by Figure 5.2, which shows grain growth data in perhaps a more familiar manner; for example, a Sn-doped sample annealed for 30 minutes in the DSC at 780°C had an average final grain size of 193 nm, while a (Ca+Sn)-doped sample annealed for the same time at the higher temperature of 900°C had a smaller final grain size of 120 nm.

Hahn *et al* have prepared nanocrystalline TiO_2 by the inert gas condensation process[13] and found that the addition of 6% Y reduced grain growth and enhanced densification such that samples could be pressureless sintered to >95% of theoretical density while maintaining a grain size <100 nm.[1] However, no pure grain growth data in the Y-TiO_2 system is provided with which we could compare to our own. Höfler and Averback have reported grain growth data for undoped nanocrystalline TiO_2 also prepared by inert gas condensation.[14] Their samples are reported to be 89-94% of theoretical density with a mean grain size of 14 nm. Höfler and Averback fit their data for anneals at 700° and 825°C to an equation of the form:

$$D^2 - D_0^2 = \alpha t^n \exp(-Q/RT) \qquad (5\text{-}1)$$

with $\alpha = 1.05 \cdot 10^{14}$ nm²/s⁻ⁿ, n~0.75, and Q=230 kJ/mole (2.4 eV).[14] This equation is not a conventional grain growth law and should not be the basis for any interpretation. (Note in particular that the "n" in equation 5-1 is not the same as the grain growth exponent in a normal grain growth law, which has a value of 2 for parabolic growth.) We use Eq. 5-1 only as a means of comparing the
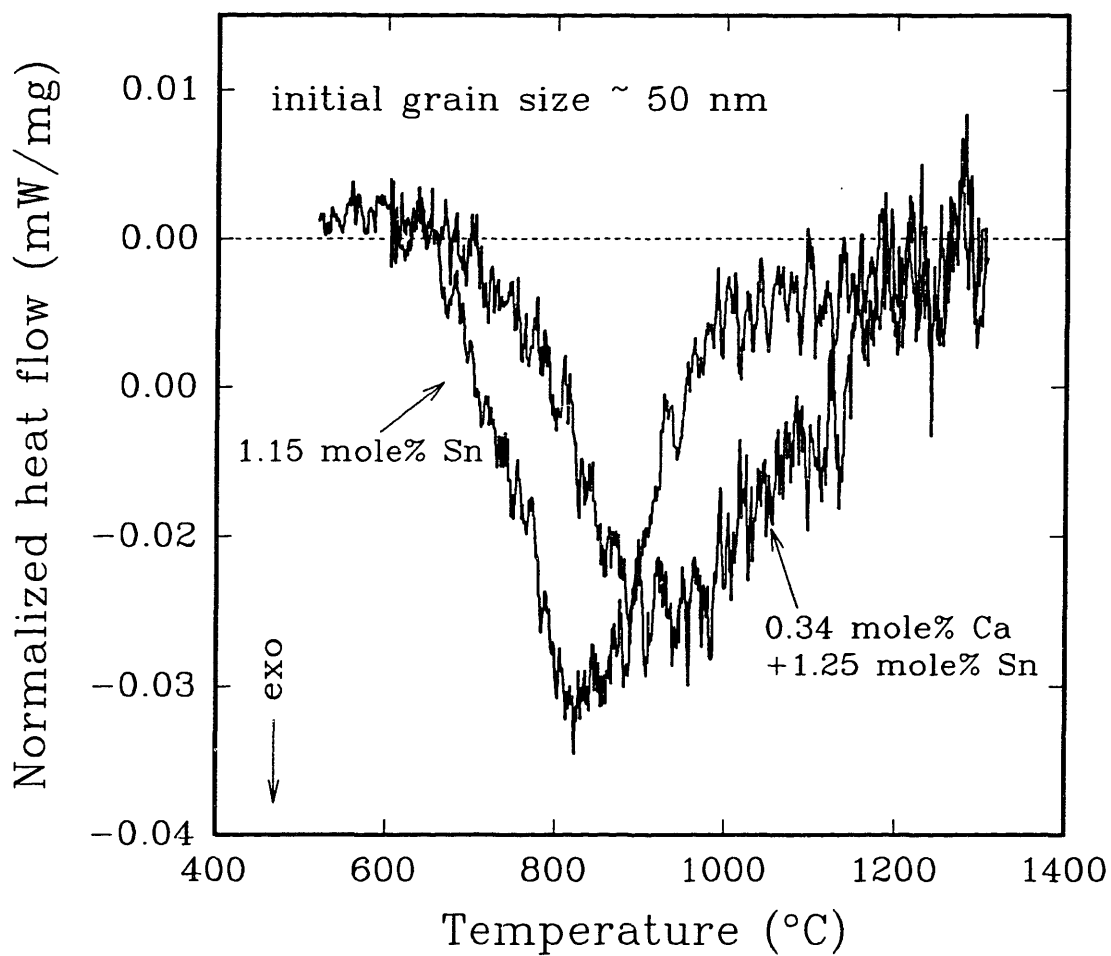
Figure 5.1. Grain growth exotherms (20°/min) of a Sn-doped and a (Ca+Sn)-doped TiO$_2$ sample with approximately the same initial grain size.
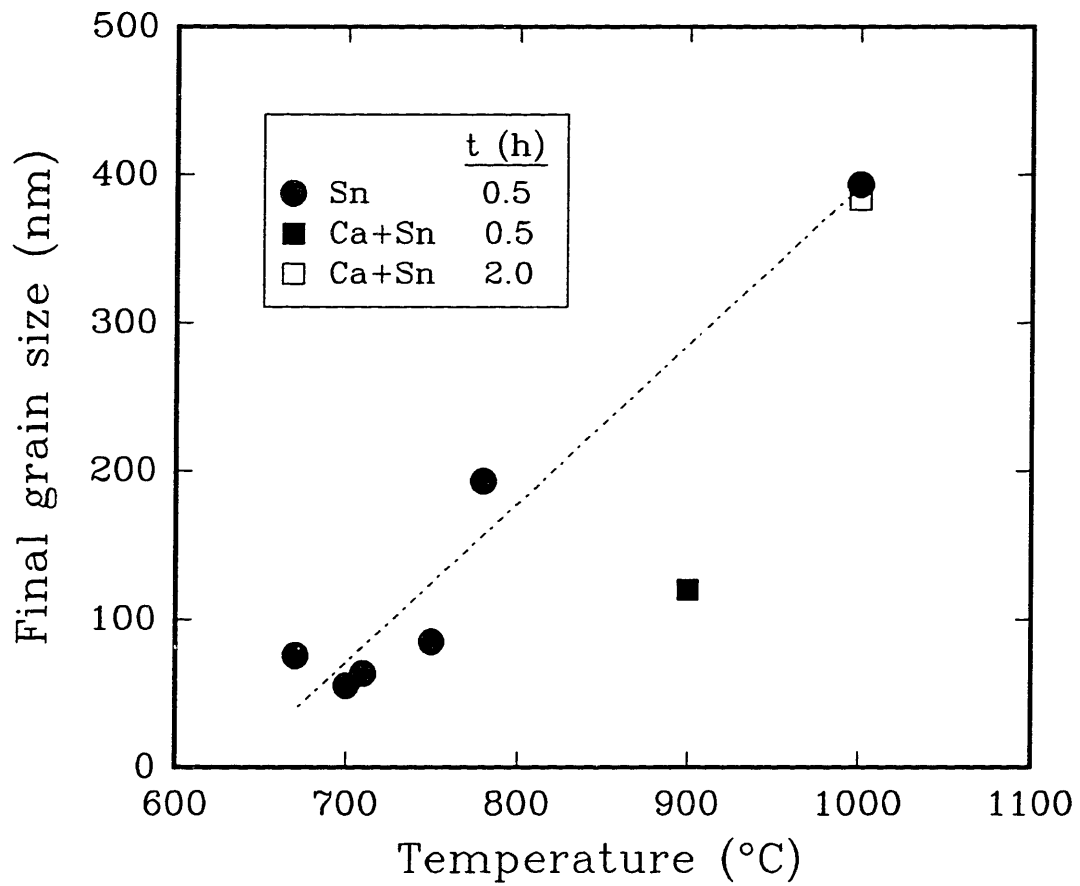
Figure 5.2. Average final grain size of Sn-doped and (Ca+Sn)-doped TiO_2 as a function of temperature for annealing times of 30 minutes and 2 hours.

"macroscopic" grain growth behavior of our materials with that of Höfler and

Averback's inert gas-condensed TiO$_2$. Table V-1 lists the initial grain sizes,

annealing treatments, and final grain sizes of our samples, along with the final grain

size that would be expected using Höfler and Averback's growth law (Eq. 5-1).

Quite clearly, calcium is effective as a grain growth inhibitor, and our chemically-

derived samples have more resistance to grain growth than Höfler and Averback's

inert gas-condensed TiO$_2$.

In Table V-1, our measurement of a mean grain size of 193 nm (780°C

anneal) has the largest error associated with it due to the likelihood that not all

projected grain dimensions were maximum grain dimensions, as discussed

previously. However, even if the TEM foil could be considered a two-dimensional

surface (grain size> >foil thickness), the actual average grain size would be ~1.56

times greater than our measurement,[15] which results in a grain size still less than

that predicted by the growth law in Ref.14. The slower growth kinetics of our Sn-

doped samples are magnified upon consideration that they are less likely to be

limited by pore drag in the early stages of growth due to their higher density.

TABLE V-1. Comparison of our grain size measurements after several different annealing treatments with predictions of final grain size using the growth law for inert gas-condensed nanocrystalline TiO$_2$ measured by Höfler and Averback.[14]

Dopant	Mean initial grain size (nm)	Annealing treatment (°C) t=0.5 h.	Mean final grain size (nm)	Predicted final grain size using growth law of ref.14 (nm)
↑	40	670	75	83
|	35	700	56	120
Sn	35	710	63	137
|	39	750	85	233
↓	38	780	193	336
Ca+Sn	49	900	120	1281

STEM microanalysis (Chapter 4) has indicated strong segregation of Ca to grain boundaries but no significant segregation or depletion of Sn that might explain the slow growth kinetics of our Sn-doped samples relative to Höfler and Averback's. One possibility is that a high concentration of defects due to nonstoichiometry in inert gas-condensed TiO_2[16] results in more rapid transport phenomena. Some support for this explanation is contained in a study of the dissociative adsorption of H_2S over inert gas-condensed nanocrystalline TiO_2,[17] in which it was found that the high activity of the samples was due in part to oxygen deficiency, and specifically, oxygen vacancies. Annealing in oxygen at high temperatures lowered the activity, even after normalizing for the lower surface area of the annealed sample.

5.4 DETERMINATION OF ACTIVATION ENERGY BY A KISSINGER ANALYSIS

Chen and Spaepen[12] have demonstrated that the Kissinger analysis,[18] a common method of determining the activation energy of chemical reactions or of nucleation events, can also be applied to grain growth. Kissinger established that for differential thermal analysis of a single, thermally-activated process, the peak position (T_p) varies with linear heating rate (α) according to the expression:

$$\frac{d\left(\ln\frac{\alpha}{T_P^2}\right)}{d(1/T_P)} = -\frac{Q}{k_B} \tag{5-2}$$

where Q is the activation energy and k_B is Boltzmann's constant. The results of this analysis for samples heated at 10, 20, 30, and 40°/min are shown in Figure 5.3 and indicate an activation energy of 1.45±.07 eV and 1.34±.4 eV for the Ca-doped and Ca-free TiO_2, respectively. The error bars at each point represent the uncertainty in the peak temperature due to noise in the DSC measurements. The uncertainty in the
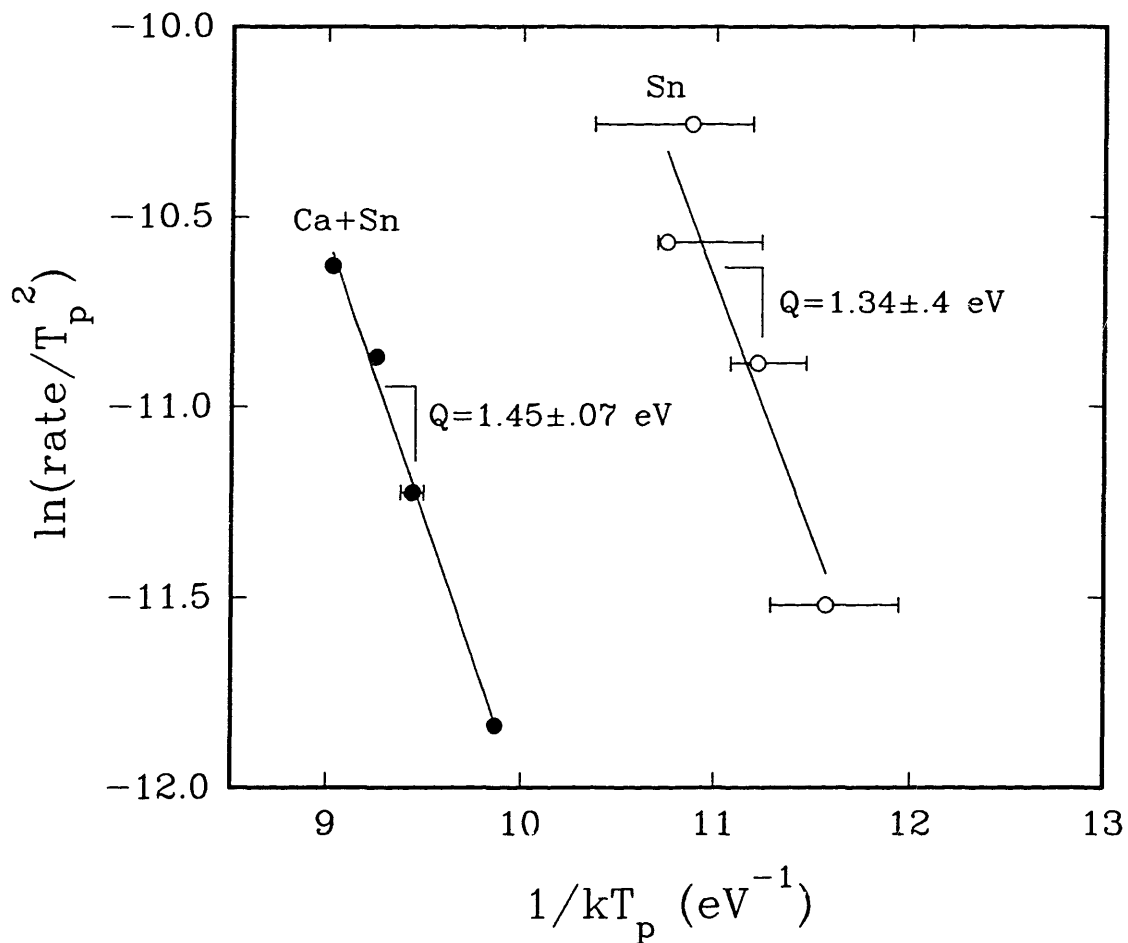
Figure 5.3. Kissinger analysis of the effective activation energy for boundary migration in Sn- and (Ca+Sn)-doped nanocrystalline TiO_2, from the change in peak temperature (T_p) with heating rate. Error bars indicate uncertainty in the peak temperature due to noise in the DSC measurements.

$\ln(\alpha/T_p^2)$ values due to T_p is negligible in comparison to those shown. A definitive conclusion about the relative values of the Ca-doped and Ca-free activation energies is difficult because of the poor fit of the Sn-doped data, but they appear to be close in value.

The activation energies for grain growth obtained by the Kissinger analysis must be viewed as effective or average values over a wide temperature range in which the mechanism of grain growth almost certainly evolves from a process limited by the intrinsic boundary mobility or by solute drag to one limited by pore drag. Nevertheless, we can make two general observations with certainty. First, the magnitude of both effective activation energies is small, about half that for lattice self-diffusion of either species.[19-21] Second, the proximity of the activation energy in the Ca-doped samples to that of the Ca-free samples can be shown to be consistent with either the temperature-*independence* of segregation in the nanocrystalline regime or an approach to intrinsic drag-limited growth at very high boundary velocities. These issues will now be discussed in turn.

Since the diffusion studies in references 19-21 were conducted at high temperatures, their activation energies for lattice self-diffusion include contributions for defect formation and for defect migration. Thus, the activation energy of 1.3-1.5 eV indicated by this work may be for lattice defect migration only, or alternatively, could be interpreted as the activation energy for grain boundary diffusion. Our low activation energies for grain growth contrast with results of the study by Höfler and Averback,[14] who found an activation energy for grain growth in undoped n-TiO$_2$ of ~ 2.4 eV using conventional methods rather than the Kissinger analysis. As previously mentioned, nanocrystalline TiO$_2$ prepared by the inert gas condensation of Ti clusters tends to be oxygen-deficient,[16] and in some cases contains crystallographic shear planes (Magneli phases Ti$_n$O$_{2n-1}$). The oxygen

content is sensitive to details of the oxidation procedure and any post-oxidation anneals, and Höfler and Averback do not completely specify their procedures. However, their grain growth anneals were conducted in pure oxygen, and thus it is possible that the activation energy they measured was a superposition of the individual values for grain growth and oxidation. Since their samples were less dense, it is also possible that grain growth began in a pore drag-limited regime, which is less likely to be the case in our samples.

Regarding the second observation from our Kissinger analysis, there are several possible explanations for the proximity of the effective activation energies of the Sn- and (Ca+Sn)-doped samples. If grain growth is occurring in the low-velocity/low driving force regime[22] and is limited by solute drag, the temperature dependence of boundary migration includes contributions from two thermally-activated processes: solute atom diffusion in the near-boundary region, and solute segregation to the boundary. The apparent activation energy for boundary migration then includes the activation energies of both individual processes. This increase in apparent activation energy for solute drag-limited boundary migration has been observed experimentally in metals.[23] However, we have established (see Chapter 4) that for grain sizes <200-400 nm at this doping level (0.34 mole% Ca), virtually all Ca atoms are located at grain boundaries, and thus very little additional segregation from the bulk can occur. As grain growth begins, the increase in solute coverage at grain boundaries is the result of a decrease in boundary area and is not a reflection of thermally-activated segregation of additional solute. Thus in the early stages of grain growth, little difference in the effective activation energy for boundary migration should be expected between nanocrystalline samples with and without solute if grain growth in the former is limited by solute drag.

Another possible explanation for the proximity of the Sn- and (Ca+Sn)-doped samples' activation energies is not a consequence of size-dependent segregation in the nanocrystalline regime. Grain growth could be in the high velocity, high driving force regime described by Cahn,[22] in which the boundary sweeps through so rapidly that most solute is left behind and the velocity approaches the intrinsic value. In this case, the activation energy is associated primarily with intrinsic drag and is generally on the order of the activation energy for grain boundary self diffusion.[22] The slower growth rate of the Ca-doped samples might still be explained by a lower grain boundary diffusion coefficient of the rate-limiting species. Since the diffusivity is dependent on concentration, if enough calcium ions are still occupying boundary sites but are not rate-limiting, the grain boundary flux of titanium or oxygen could be decreased accordingly due to a decrease in the available sites for migration.

5.5 MODELING OF THE CALORIMETRIC SIGNATURE OF GRAIN GROWTH

Chen and Spaepen have modeled the enthalpy release rate upon grain growth using normal grain growth theory.[12] They show that dH/dt, the quantity measured by a DSC, for a linear heating rate experiment can be written to a good approximation as:

$$\frac{dH}{dT} = -\left(\frac{gH_{gb}V}{n}\right) \cdot \frac{K(T)}{\left[r_0^n + \frac{k_B T^2}{\alpha Q} \cdot K(T)\right]^{\frac{n+1}{n}}} \tag{5-3}$$

where $K(T)$ is a rate constant of the form $(K_0/T)\exp(-Q/k_B T)$, r_0 is the initial grain radius, α is the heating rate, Q is the activation energy, n is the grain growth exponent, H_{gb} is the specific grain boundary enthalpy (J/m^2), V is the sample volume, and g is a geometric constant related to the grain shape and size

106

distribution. Thus, in concept one can model grain growth exotherms if the kinetic parameters and H_{gb} are known, or estimate one or more unknown kinetic parameters from a multiple non-linear regression analysis. The reader is referred to Ref.12 for a full derivation of Eq.5-3.

Reexamining the grain growth exotherms of Ca-doped and Ca-free samples in Fig. 5.1, one can see that the effect of calcium is to decrease the slope of the leading edge of the curve, decrease the magnitude of the peak, shift it to a higher temperature, and broaden the entire curve. Figure 5.4(a) is a simulation calculated using Eq.5-3 which shows that if, indeed, the presence of calcium slightly increases the activation energy for grain growth and all other parameters are unaffected, the grain growth exotherm shifts to a higher temperature and decreases in magnitude. However, the slope and breadth of the peak show little change, and the onset of the exotherm is delayed, which was not observed in our samples.

Many years ago Brook[24] demonstrated theoretically that size-dependent grain boundary and bulk solute concentrations should induce a change from a $t^{1/2}$ ($n=2$) to a $t^{1/3}$ ($n=3$) growth law at fine grain sizes. However, it can be seen from Figure 5.4(b) that, all else being equal, if the Ca-doped samples had a larger n than the Ca-free samples the peak of the former would occur at a lower temperature, which is contrary to what we observe. Therefore, if n increases due to a size-dependent boundary coverage it must be accompanied by changes in other kinetic parameters to explain the change in our grain growth exotherms.

Direct use of Eq. 5-3 for modeling grain growth exotherms assumes kinetic and thermodynamic parameters (n, Q, K_0, H_{gb}) that are constant with temperature and grain size. However, in the early stages of grain growth in a nanocrystalline material in which there is size-dependent solute segregation, a rapidly increasing grain boundary solute coverage will result in size-dependent kinetic parameters if
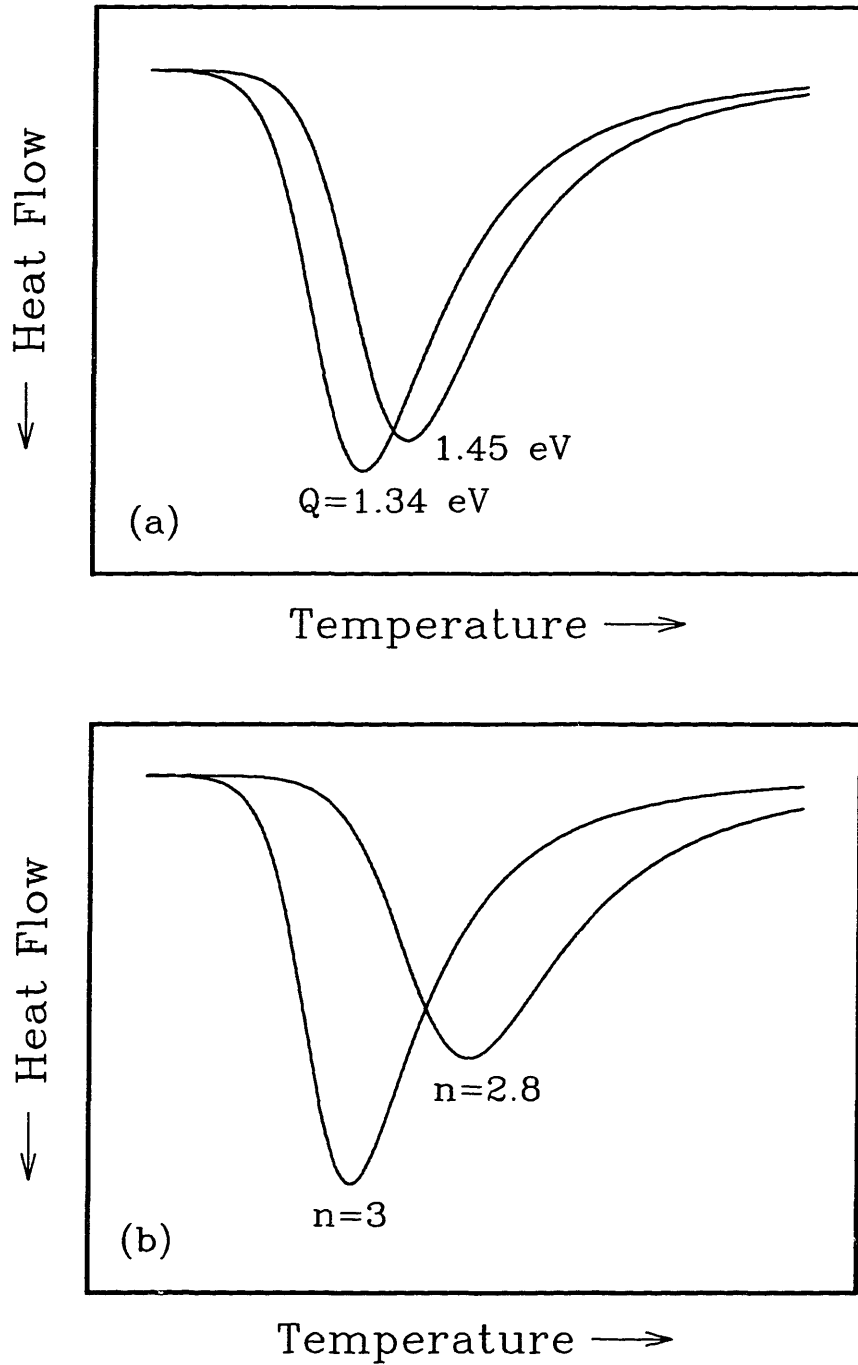
Figure 5.4. Simulations of grain growth exotherms, calculated using Eq.5-3 in the text. (a) Effect of a small change in activation energy. The values of Q are those indicated by the Kissinger analyses of our Sn- and (Ca+Sn)-doped samples. All other parameters remain constant ($n=3$). (b) Effect of a change in the grain growth exponent, n. All other parameters remain constant (Q=1.5 eV).

growth is limited by solute drag. Furthermore, our own measurements of excess enthalpy of grain boundaries in Sn-doped TiO_2 indicate a significant temperature-and/or size-dependence of the specific grain boundary enthalpy, H_{gb} (Chapter 2). Size- and/or temperature-dependences of multiple variables in the expression for dH/dt (Eq. 5-3) make definitive modeling intractable. Nevertheless, introduction of a simple functionality for one parameter at a time is feasible and informative; two examples are shown in Figure 5.5. For convenience only, a sigmoidal function has been chosen to simulate the effect of a one order of magnitude decrease in K_0 over the temperature range (and thus grain size range) of the exotherm. In Figure 5.5(a) the resulting exotherm is compared to one obtained maintaining the initial value of K_0 over the entire temperature range. With all other parameters held constant, this scenario is intended to simulate the effect of a gradual approach to a one order of magnitude difference in the grain boundary mobility of two samples due to a size-dependent grain boundary solute coverage in one of them. Qualitatively, the two exotherms of Figure 5.5(a) show similar features as the exotherms of our Sn-doped and (Ca+Sn)-doped samples in Figure 5.1. Introduction of the temperature/size dependence of H_{gb} that we have measured in separate experiments on Sn-doped samples (Chapter 2) also broadens the exotherm and shifts the peak very slightly (Fig.5.5(b)). The addition of Ca would need to introduce a steeper dependence of the grain boundary enthalpy on size or temperature to be the sole explanation for the exotherm positions in Fig. 5.1. Of course, a combination of some or all of these temperature or size dependences is likely and could only be determined from further study.

109
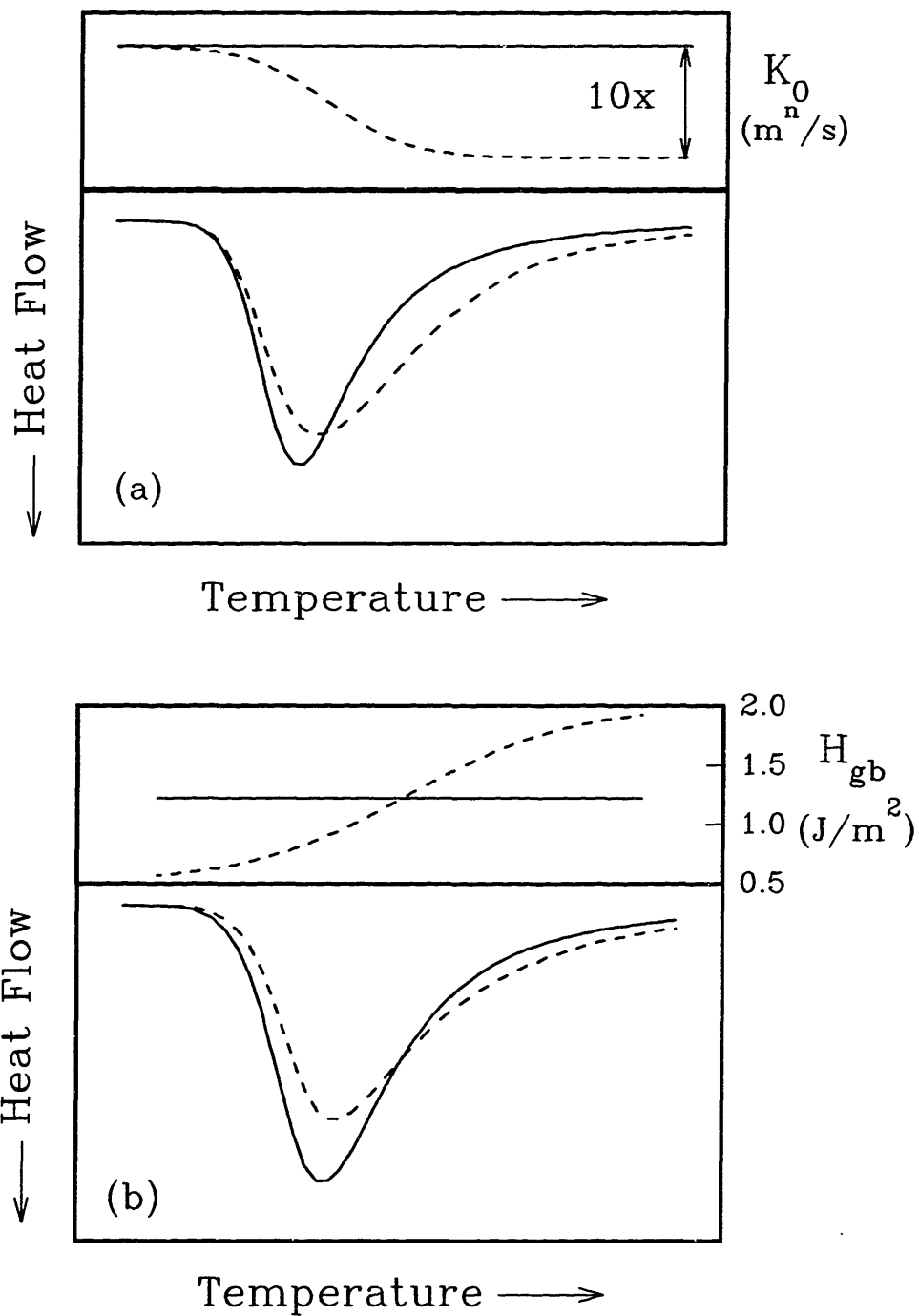
Figure 5.5. Simulations of grain growth exotherms, showing the effect of size- or temperature-dependent kinetic or thermodynamic parameters. (a) Simulation using a constant pre-exponential, K_0 (—) and one that decreases by one order of magnitude over the course of the experiment (– – –). (b) Simulation of a constant grain boundary enthalpy (—) and one that increases from ~ 0.5 J/m^2 to 2 J/m^2 over the course of the experiment (– – –).

110

5.6 SUMMARY

The addition of 0.34 mole% Ca to ultrafine-grained TiO_2 significantly inhibits grain growth. Furthermore, comparison with a report on grain growth kinetics in nanocrystalline TiO_2 prepared by the inert gas condensation process indicates that both our Sn- and (Ca+Sn)-doped samples have more resistance to grain growth. Estimation of the apparent activation energy for grain growth by a Kissinger analysis of grain growth exotherms indicates a value of 1.3-1.5 eV for both Sn- and (Ca+Sn)-doped samples. The relative positions of the grain growth exotherms of Ca-doped and Ca-free samples could be explained by a size-dependent mobility due to size-dependent segregation of Ca, or by a combination of temperature and size dependences of kinetic and thermodynamic parameters of grain growth.

CHAPTER 6

CONCLUSIONS

Excess Thermodynamic Properties of Ultrafine-grained TiO$_2$

(1) There is a clear temperature or grain size dependence of the specific grain boundary enthalpy, H$_{gb}$, of TiO$_2$; the temperature and size effects are inextricably linked. Measured values increase from $\sim$0.5-1 J/m^2 at grain sizes of $\sim$30-200 nm and temperatures of 600-780°C to 1.3-1.7 J/m^2 averaged over a much larger grain size and temperature range (30 nm $\sim$2μm, 600-1300°C).

(2) The increase in H$_{gb}$ with temperature or grain size is not due to experimental artifacts. Extraneous contributions to H$_{gb}$ from the anatase-rutile phase transformation, sintering, and lattice strain have been shown to be negligible.

(3) A positive excess heat capacity of ultrafine-grained TiO$_2$ has been measured and confirms the trend of an increasing H$_{gb}$ with temperature or grain size. The variation between samples of the normalized excess heat capacity (J/m^{2}K) is due to a complex interplay between thermal history, grain size, and (possibly) oxygen content.

(4) The most plausible explanation for a size- or temperature-dependent H$_{gb}$ is a size-dependent nonstoichiometry of rutile due to the impingement of space charge layers in the grain size and temperature range of these experiments. Debye lengths of 165 nm and 33 nm are estimated for intrinsic, reduced TiO$_2$ in air at 800° and 1000°C, respectively. It is shown qualitatively that when space charge layers overlap, the grain boundary defect concentration scales with volume rather than interfacial area, resulting in a size-dependent H$_{gb}$.

Solute Segregation at Ultrafine Grain Sizes

(1) Quantitative measurements of Ca coverage at TiO$_2$ grain boundaries using STEM microanalysis show that for a doping level of 0.34 mole% Ca,

112

segregation deviates from conventional isotherms at grain sizes below 200-400 nm and is as strong a function of grain size as of temperature or composition. The lattice is almost entirely depleted of solute at all grain sizes examined. As grain size increases, solute coverage at grain boundaries increases due to a decrease in boundary area rather than segregation of additional solute from the lattice.

(2) Grain boundaries in TiO_2 become saturated with Ca at approximately one half of an equivalent monolayer.

(3) The experimental results can be modeled with a statistical thermodynamical treatment of segregation that accounts for the excess of grain boundary sites at fine crystal sizes. This theoretical treatment has also been used to calculate a generalized segregation map from which the threshold grain size, below which segregation is size-dependent, can be found as a function of doping level, H/T ratio, and saturation coverage.

(4) An equilibrium size-dependent total solid solubility due to grain boundary segregation has been observed. Evidence for this effect includes the precipitation of $CaTiO_3$ upon coarsening as well as the incorporation of up to 3.69 mole% Ca into ultrafine TiO_2 powders.

Grain Growth Inhibition

(1) The addition of 0.34 mole% Ca inhibits grain growth in ultrafine-grained TiO_2. Furthermore, the Sn-doped TiO_2, in addition to the (Ca+Sn)-doped TiO_2, exhibits more resistance to grain growth than ultrafine-grained TiO_2 prepared by inert gas condensation.

(2) A Kissinger analysis of grain growth exotherms has shown that the effective activation energy for grain growth is between 1.3-1.5 eV for both Sn- and

(Ca+Sn)-doped samples. It is shown that for solute-drag limited grain growth below the threshold grain size (where segregation is independent of temperature), solute will not have the usual effect of increasing the effective activation energy for grain growth.

(3) The presence of calcium at grain boundaries in ultrafine-grained TiO_2 affects the grain growth exotherm measured by differential scanning calorimetry. The shift in position and the broadening of the exotherms of the Ca-doped samples relative to those of Ca-free samples is shown to be consistent with a grain boundary mobility that decreases with increasing grain size, which is expected due to the observed size-dependent Ca coverage if growth is limited by solute drag.

CHAPTER 7

SUGGESTIONS FOR FUTURE WORK

(1) The most intriguing finding of this research is the rather large size and/or temperature dependence of the specific grain boundary enthalpy of TiO_2, and we have hypothesized that this trend is the result of a size-dependent nonstoichiometry of TiO_2 due to impingement of space charge layers. Additional support for this hypothesis could be obtained using high sensitivity thermogravimetry. There are quite interesting implications regardless of the outcome:

    (a) If there is a size-dependent nonstoichiometry of TiO_2 (and by extension, many other nonstoichiometric oxides), one would expect enhanced ionic conduction at very fine grain sizes, which may have important technological implications.

    (b) If no weight gain is detected by high sensitivity thermogravimetry, the suggestion would be a very steep temperature dependence of the average enthalpy of general, high angle boundaries that has not yet been demonstrated by theoretical calculations.

(2) A more rigorous analysis of the effect of impinging space charge layers on grain boundary defect concentrations should be undertaken. In particular, the addition of aliovalent solutes could be modeled and the resulting effect on H_{gb} could be predicted and compared with calorimetric measurements. Measurements of the grain boundary enthalpy of $(Ca+Sn)$-TiO_2 (acceptor-doped) and one measurement of $(Nb+Sn)$-TiO_2 (donor-doped) have indicated a larger H_{gb} due to Ca and a smaller H_{gb} due to Nb, relative to that of Sn-doped samples of comparable initial grain size. It would be interesting to see if this difference is

supported by additional measurements and if it is predicted by modeling of impinging space charge layers.

(3) Low temperature (100-300K) heat capacity measurements might clarify some of the unanswered questions regarding the temperature dependence of H_{gb} and might enable nearly absolute measurements of grain boundary entropy, S_{gb}.

(4) Size-dependent segregation at fine grain sizes suggests several possibilities for future work:

    (a) How is space charge segregation affected by size-dependent coverages? In particular, one might see some interesting effects due to depletion of solute from the bulk; the bulk's defect chemistry will be forced into the intrinsic regime.

    (b) A careful study of the kinetics of grain growth in the size-dependent regime might indicate a self-stabilizing effect as coverage increases toward saturation.

    (c) We now have some level of predictability as to the solute coverage versus grain size curve for a particular material system, doping level, and temperature. This capability to tune grain boundary coverages may allow design of some interesting experiments to test our understanding of segregation effects on fracture mechanisms and grain boundary cohesion.

(5) The primary obstacle for superplastic deformation of fine-grained ceramics is usually dynamic grain growth. We have successfully extended the stability of nanocrystalline grain sizes by doping with Ca or Nb, perhaps enough to allow for diffusional creep measurements at low temperatures with minimal grain growth.

BIBLIOGRAPHY

Chapter 1

1. M.C. Inman and H.R. Tipler, "Interfacial Energy and Composition of Metals and Alloys," *Met. Rev.* **8**, 105-166 (1963).

2. P.J. Goodhew, "The Relationship Between Grain Boundary Structure and Energy," pp. 155-179 in Grain Boundary Structure and Kinetics (ASM, Metals Park, OH, 1980).

3. D.M. Duffy and P.W. Tasker, "Properties of Grain Boundaries in Rock Salt Structured Oxides," pp. 275-289 in Structure and Properties of MgO and Al_2O_3 Ceramics, Ed. W.D. Kingery (Adv. in Ceram. **10**, American Ceramic Society, Columbus, OH, 1984).

4. D. Wolf, "Energy and Structure of (001) Coincident-Site Twist Boundaries and the Free (001) Surface in MgO: A Theoretical Study," *J. Am. Ceram. Soc.* **67**, 1-13 (1984).

5. N.A. Gjostein and F.N. Rhines, "Absolute Interfacial Energies of [001] Tilt and Twist Grain Boundaries in Copper," *Acta Metall.* **7**, 319-330 (1959).

6. D.W. Readey and R.E. Jech, "Energies and Grooving Kinetics of [001] Tilt Boundaries in Nickel Oxide," *J. Am. Ceram. Soc.* **51**, 201-208 (1968).

7. E.N. Hodkin and M.G. Nicholas, "Surface and Interfacial Properties of Stoichiometric Uranium Dioxide," *J. Nucl. Mat.* **47**, 23-30 (1973).

8. G. Dimou and K.T. Aust, "Relative Energies of Grain Boundaries Near A Coincidence Orientation Relationship in High Purity Lead," *Acta Metall.* **22**, 27-32 (1974).

9. G. Achutaramayya and W.D. Scott, "Interfacial Energies of Coherent Twin Boundaries in Alumina," *Acta Metall.* **23**, 1469-1472 (1975).

10. G. Dhalenne, A. Revcolevschi, and A. Gervais, "Grain Boundaries in NiO I. Relative Energies of <001> Tilt Boundaries," *Phys. Stat. Sol.* **56**, 267-276 (1979).

11. C.A. Handwerker, "Sintering and Grain Growth of MgO," Sc.D. Thesis, Massachusetts Institute of Technology, 1983.

12. V. Paidar, J. Gemperlová, P. Lejcek, and V. Vitek, "A Report on Current Research on Grain-Boundary Structure and Chemistry," *Mat. Sci. Eng.* **A154**, 113-123 (1992).

13. H. Gleiter and B. Chalmers, "High-Angle Grain Boundaries," *Prog. Mat. Sci.* **16**, 13-42 (1972).

14. K.L. Kliewer and J.S. Koehler, "Space Charge in Ionic Crystals. I. General Approach with Application to NaCl," *Phys. Rev.* **140**, A1226-A1240 (1965).

15. W.D. Kingery, "Plausible Concepts Necessary and Sufficient for Interpretation of Ceramic Grain-Boundary Phenomena: I, Grain-Boundary Characteristics, Structure, and Electrostatic Potential," *J. Am. Ceram. Soc.* **57**, 1-8 (1974).

16. P. Kofstad, Nonstoichiometry, Diffusion, and Electrical Conductivity in Binary Metal Oxides (Wiley-Interscience, NY, 1972), pp. 137-152.

17. J.A.S. Ikeda, Y.-M. Chiang, A.J. Garratt-Reed, and J.B. VanderSande, "Space Charge Segregation at Grain Boundaries in Titanium Dioxide: II. Model Experiments," accepted for publication in *J. Am. Ceram. Soc.*

18. E.A. Colbourn, W.C. Mackrodt, and P.W. Tasker, "The Segregation of Calcium Ions at the Surface of Magnesium Oxide: Theory and Calculation," *J. Mat. Sci.* **18**, 1917-1924 (1983).

19. C.R. Helms, "Segregation Effects in Small Particles Used in Catalysis," pp. 175-190 in Interfacial Segregation, Eds. W.C. Johnson and J.M. Blakely, ASM, Metals Park, OH, 1979.

20. D. McLean, Grain Boundaries in Metals, Clarendon Press, Oxford, 1957, pp. 116-131.

21. H. Gleiter, "Nanocrystalline Materials," *Prog. Mater. Sci.* **33**, 223-315 (1990).

22. R.W. Siegel, "Cluster Assembly in Nanophase Materials," pp. 583-614 in Processing of Metals and Alloys, Ed. R.W. Cahn (Materials Science and Technology Series, **15**, VCH, Weinheim, 1991).

23. L.C. Chen and F. Spaepen, "Analysis of calorimetric measurements of grain growth," *J. Appl. Phys.* **69**, 679-688 (1991).

Chapter 2

1. H.U. Åström, "Experimental Studies on Grain Growth in Metals," *Arkiv fur Fysik* **13**, 69-80 (1957).

2. L.-C. Chen and F. Spaepen, "Calorimetric evidence for the microquasicrystalline structure of 'amorphous' Al/transition metal alloys," *Nature* **336**, 366-368 (1988).

3. L.-C. Chen and F. Spaepen, "Analysis of calorimetric measurements of grain growth," *J. Appl. Phys.* **69**, 679-688 (1991).

4. J. Eckert, J.C. Holzer, C.E. Krill III, and W.L. Johnson, "Structural and Thermodynamic Properties of Nanocrystalline FCC Metals Prepared by Mechanical Attrition," *J. Mater. Res.* **7**, 1751-1761 (1992).

5. H.J. Fecht, E. Hellstern, Z. Fu, and W.L. Johnson, "Nanocrystalline Metals Prepared by High-Energy Ball Milling," *Met. Trans. A* **21A**, 2333-2337.

6. A. Tschöpe, R. Birringer, and H. Gleiter, "Calorimetric measurements of the thermal relaxation in nanocrystalline platinum," *J. Appl. Phys.* **71**, 5391-5394 (1992).

7. K. Lu, W.D. Wei, and J.T. Wang, "Grain growth kinetics and interfacial energies in nanocrystalline Ni-P alloys," *J. Appl. Phys.* **69**, 7345-7347 (1991).

8. R.W. Siegel, S. Ramasamy, H. Hahn, L. Zongquan, L. Ting, and R. Gronsky, "Synthesis, Characterization, and Properties of Nanophase TiO_2," *J. Mater. Res.* **3**, 1367-1372 (1988).

9. J.A. Eastman, Y.X. Liao, A. Narayanasamy, and R.W. Siegel, "Processing and Properties of Nanophase Oxides," pp. 255-266 in Processing Science of Advanced Ceramics, Eds. I.A. Aksay, G.L. McVay, D.R. Ulrich (Mat. Res. Soc. Symp. Proc. **155**, Materials Research Society, Pittsburgh, PA, 1989).

10. C.S. Smith and L. Guttman, "Measurement of Internal Boundaries in Three-Dimensional Structures by Random Sectioning," *J. Metals (Trans. AIME)* **5**, 81-87 (1953).

11. E.E. Underwood, Quantititative Stereology (Addison-Wesley, Reading, MA, 1970).

12. M.I. Mendelson, "Average Grain Size in Polycrystalline Ceramics," *J. Am. Ceram. Soc.* **52**, 443-446 (1969).

13. H.V. Atkinson, "Theories of Normal Grain Growth in Pure Single Phase Systems," *Acta Metall.* **36**, 469-491 (1988).

14. C.D. Terwilliger, Y.-M. Chiang, J.A. Eastman, and Y. Liao, "Measurement of Thermodynamic and Kinetic Properties of Grain Boundaries Using High Temperature Calorimetry," pp. 325-332 in Point Defects and Related Properties of Ceramics, Eds. T.O. Mason and J.L. Routbort (Ceram. Trans. **24**, American Ceramic Society, Westerville, OH, 1991).

15. Y.-M. Chiang, I.P. Smyth, C.D. Terwilliger, W. Petuskey, and J.A. Eastman, "Measurement of Grain Boundary Properties in Nanocrystalline Ceramics," *Nanostructured Materials* **1**, 235-240 (1992).

16. P. Kofstad, Nonstoichiometry, Diffusion, and Electrical Conductivity in Binary Metal Oxides (Wiley-Interscience, NY, 1972), pp. 137-152.

17. A. Navrotsky and O.J. Kleppa, "Enthalpy of the Anatase-Rutile Transformation," *J. Am. Ceram. Soc.* **50**, 626 (1967).

18. H.P. Klug and L. Alexander, X-ray Diffraction Procedures for Polycrystalline and Amorphous Materials, 2nd. ed. (John Wiley, NY, 1974), pp. 661-665.

19. W.A. Rachinger, "A Correction for the $\alpha_1 \alpha_2$ Doublet in the Measurement of Widths of X-ray Diffraction Lines," *J. Sci. Instrum.* **25**, 254-255 (1948).

119

20. E. Hellstern, H.J. Fecht, Z. Fu, and W.L. Johnson, "Structural and Thermodynamic Properties of Heavily Mechanically Deformed Ru and AlRu," *J. Appl. Phys.* **65**, 305-310 (1989).

21. C.C. Koch, "The Synthesis and Structure of Nanocrystalline Materials Produced by Mechanical Attrition: A Review," *Nanostructured Materials* **2**, 109-129 (1993).

22. G. Simmons and H. Wang, Single Crystal Elastic Constants and Calculated Aggregate Properties, 2nd ed. (MIT Press, Cambridge, MA, 1971), p. 299.

23. J.C. Parker and R.W. Siegel, "Calibration of the Raman spectrum to the oxygen stoichiometry of nanophase TiO_2," *Appl. Phys. Lett.* **57**, 943-945 (1990).

24. Z. Li, S. Ramasamy, H. Hahn, and R.W. Siegel, "Fractographic Study of Sintered Nanophase TiO_2," *Mater. Lett.* **6**, 195-201 (1988).

25. D.D. Beck and R.W. Siegel, "The dissociative adsorption of hydrogen sulfide over nanophase titanium dioxide," *J. Mater. Res.* **7**, 2840-2845 (1992).

26. C.D. Terwilliger and Y.-M. Chiang, "Characterization of Chemically-and Physically-Derived Nanophase Titanium Dioxide," *Nanostructured Materials* **2**, 37-45 (1993).

27. J.S. Anderson and R.J.D. Tilley, "Crystallographic Shear in Oxygen-Deficient Rutile: An Electron Microscope Study," *J. Solid St. Chem.* **2**, 472-482 (1970).

28. J. Rupp and R. Birringer, "Enhanced Specific Heat Capacity (C_p) Measurements (150-300K) of Nanometer-sized Crystalline Materials," *Phys. Rev. B* **36**, 7888-7890 (1987).

29. D. Korn, A. Morsch, R. Birringer, W. Arnold, and H. Gleiter, "Measurements of the Elastic Constants, the Specific Heat, and the Entropy of Grain Boundaries by Means of Ultra-fine Grained Materials," *J. de Phys.* **C5**, 769-779 (1988).

30. A. Tschöpe, personal communication.

31. S. Ram and G.P. Johari, "Glass-liquid transition in hyperquenched metal alloys," *Phil. Mag. B* **61**, 299-310 (1990).

32. L.-C. Chen and F. Spaepen, "A comment on the use of calorimetry for the determination of the structure of amorphous materials," *Phil. Mag. B* **63**, 585-586 (1991).

33. D.M. Duffy and P.W. Tasker, "A calculation of the formation energies of intrinsic defects near grain boundaries in NiO," *Phil. Mag. A* **50**, 143-154 (1984).

34. D. Wolf, "Formation Energy of Point Defects in Free Surfaces and Grain Boundaries in MgO," *Rad. Effects* **75**, 203-209 (1983).

35. J.H. Harding, "Computer simulation of defects in ionic solids," *Rep. Prog. Phys.* **53**, 1403-1466 (1990).

36. P. Kofstad, "Thermogravimetric Studies of the Defect Structure of Rutile (TiO_2)," *J. Phys. Chem. Solids* **23**, 1579-1586 (1962).

37. K.S. Forland, "The Defect Structure of Rutile," *Acta Chem. Scand.* **18**, 16-24 (1964).

38. J. Frenkel, Kinetic Theory of Liquids, Oxford University Press, New York, 1946.

39. K.L. Kliewer and J.S. Koehler, "Space Charge in Ionic Crystals. I. General Approach with Application to NaCl," *Phys. Rev.* **140**, A1226-A1240 (1965).

40. W.D. Kingery, "Plausible Concepts Necessary and Sufficient for Interpretation of Ceramic Grain-Boundary Phenomena: I, Grain-Boundary Characteristics, Structure, and Electrostatic Potential," *J. Am. Ceram. Soc.* **57**, 1-8 (1974).

41. Y.-M. Chiang, A.F. Henriksen, W.D. Kingery, and D. Finello, "Characterization of Grain Boundary Segregation in MgO," *J. Am. Ceram. Soc.* **64**, 385- (1981).

42. J.A.S. Ikeda, Y.-M. Chiang, A.J. Garratt-Reed, and J.B. VanderSande, "Space Charge Segregation at Grain Boundaries in Titanium Dioxide: II. Model Experiments," accepted for publication in *J. Am. Ceram. Soc.*

43. C.R.A. Catlow and R. James, "Disorder in TiO_{2-x}," *Proc. R. Soc. Lond. A* **384**, 157-173 (1982).

44. J.A.S. Ikeda and Y.-M. Chiang, "Space Charge Segregation at Grain Boundaries in Titanium Dioxide: I. Relationship Between Lattice Defect Chemistry and Space Charge Potential," accepted for publication in *J. Am. Ceram. Soc.*

45. Y.T. Tan and H.A. Hoyen, Jr., "A Model of Surface Spage Charge in Thin Films of AgBr," *Surf. Sci.* **36**, 242-252 (1973).

46. M.E. Van Hulle, "Surface Space Charge Potential in Thin Silver Halides," *Surf. Sci.* **52**, 513-520 (1975).

47. J. Maier, "Defect Chemistry and Ionic Conductivity in Thin Films," *Solid St. Ionics* **23**, 59-67 (1987).

48. J. Maier, S. Prill, and B. Reichert, "Space Charge Effects in Polycrystalline, Micropolycrystalline, and Thin Film Samples: Application to AgCl and AgBr," *Solid St. Ionics* **28-30**, 1465-1469 (1988).

49. H. Gleiter and B. Chalmers, "High-Angle Grain Boundaries," *Prog. Mat. Sci.* **16**, 13-42 (1972).

50. A.P. Sutton, "Temperature-dependent interatomic forces," *Phil. Mag. A* **60**, 147-159 (1989).

51. H.J. Fecht, "Intrinsic Instability and Entropy Stabilization of Grain Boundaries," *Phys. Rev. Lett.* **65**, 610-613 (1990).

52. D. Wolf, "Correlation Between Energy and Volume Expansion for Grain Boundaries in FCC Metals," *Scripta Metall.* **23**, 1913-1918 (1989).

53. K.Lu, R. Lück, and B. Predel, "The Interfacial Excess Energy in Nanocrystalline Ni-P Materials with Different Grain Sizes," accepted for publication in *Scripta Metall.*

54. G. Palumbo, S.J. Thorpe, and K.T. Aust, "On the Contribution of Triple Junctions to the Structure and Properties of Nanocrystalline Materials," *Scripta Metall.* **24**, 1347-1350 (1990).

Chapter 4

1. J.H. Westbrook, "Segregation at Grain Boundaries," *Met. Rev.* **9**, 415-471 (1964).

2. W.D. Kingery, "Plausible Concepts Necessary and Sufficient for Interpretation of Ceramic Grain-Boundary Phenomena: I, Grain-Boundary Characteristics, Structure, and Electrostatic Potential," *J. Am. Ceram. Soc.* **57**, 1-8 (1974).

3. W.D. Kingery, "Plausible Concepts Necessary and Sufficient for Interpretation of Ceramic Grain-Boundary Phenomena: II, Solute Segregation, Grain-Boundary Diffusion, and General Discussion," *J. Am. Ceram. Soc.* **57**, 74-83 (1974).

4. D.F. Stein and L.A. Heldt, "Grain Boundary Segregation and Materials Properties," pp. 239-260 in Interfacial Segregation, Eds. W.C. Johnson and J.M. Blakely, ASM, Metals Park, OH, 1979.

5. H. Gleiter, "Nanocrystalline Materials," *Prog. Mater. Sci.* **33**, 223-315 (1990).

6. R.W. Siegel, "Cluster Assembly in Nanophase Materials," pp. 583-614 in Processing of Metals and Alloys, Ed. R.W. Cahn (Materials Science and Technology Series, 15, VCH, Weinheim, 1991).

7. D. McLean, Grain Boundaries in Metals, Clarendon Press, Oxford, 1957, pp. 116-131.

8. C.C. Koch, "The Synthesis and Structure of Nanocrystalline Materials Produced by Mechanical Attrition: A Review," *Nanostructured Materials* **2**, 109-129 (1993).

9. J. Eckert, J.C. Holzer, and W.L. Johnson, "Thermal stability and grain growth behavior of mechanically alloyed nanocrystalline Fe-Cu alloys," *J. Appl. Phys.* **73**, 131-141 (1993).

10. R. Birringer, H. Hahn, H.J. Höfler, J. Karch, and H. Gleiter, "Diffusion and Low Temperature Deformation by Diffusional Creep of Nanocrystalline Materials," *Defect and Diffusion Forum* **59**, 17-31 (1988).

11. J. Weissmüller, W. Krauss, T. Haubold, R. Birringer, and H. Gleiter, "Atomic Structure and Thermal Stability of Nanostructured Y-Fe Alloys," *Nanostructured Materials* **1**, 439-447 (1992).

12. H. Hahn, R.S. Averback, H.J. Hofler, and J. Logas, "Sintering and Deformation of Nanocrystalline Ceramics," pp. 569-580 in Clusters and Cluster-Assembled Materials (Mat. Res. Soc. Symp. Proc. 206), Eds. R.S. Averback, J. Bernholc, D.L. Nelson, Materials Research Society, Pittsburgh, PA, 1991.

13. P. Knauth, A. Charaï, and P. Gas, "Grain Growth of Pure Nickel and of a Ni-Si Solid Solution Studied by Differential Scanning Calorimetry on Nanometer-Sized Crystals," *Scripta Metall.* **28**, 325-330 (1993).

14. K. Lu, J.T. Wang, and W.D. Wei, "Comparison of Properties of Nanocrystalline and Amorphous Ni-P Alloys," *J. Phys. D: Appl. Phys.* **25**, 808-812 (1992).

15. K. Boylan, D. Ostrander, U. Erb, G. Palumbo, and K.T. Aust, "An In-Situ TEM Study of the Thermal Stability of Nanocrystalline Ni-P," *Scripta Metall.* **25**, 2711-2716 (1991).

16. T. Haubold, "EXAFS Studies of Bismuth Doped Nanocrystalline Copper," *Acta Metall.* **41**, 1769-1772 (1993).

17. C.D. Terwilliger and Y.-M. Chiang, "Grain Growth Inhibition from Calcium Additions to Nanocrystalline TiO$_2$," submitted to

18. E.A. Colbourn, W.C. Mackrodt, and P.W. Tasker, "The Segregation of Calcium Ions at the Surface of Magnesium Oxide: Theory and Calculation," *J. Mat. Sci.* **18**, 1917-1924 (1983).

19. Y.-M. Chiang, A.F. Henriksen, W.D. Kingery, and D. Finello, "Characterization of Grain Boundary Segregation in MgO," *J. Am. Ceram. Soc.* **64**, 385- (1981).

20. J.A.S. Ikeda, Y.-M. Chiang, A.J. Garratt-Reed, and J.B. VanderSande, "Space Charge Segregation at Grain Boundaries in Titanium Dioxide: II. Model Experiments," accepted for publication in *J. Am. Ceram. Soc.*

21. K.L. Kliewer and J.S. Koehler, "Space Charge in Ionic Crystals. I. General Approach with Application to NaCl," *Phys. Rev.* **140**, A1226-A1240 (1965).

22. J.A.S. Ikeda, Y.-M. Chiang, and A.J. Garratt-Reed, "Quantification of Grain Boundary Segregation in TiO_2 by STEM," to appear in the Proceedings of the XIII International Conference on X-ray Optics and Microanalysis, Manchester, U.K., August 31-September 4, 1992.

23. G. Cliff and G.W. Lorimer, "The Quantitative Analysis of Thin Specimens," *J. Micros.* 103, 203-207 (1975).

24. P. Kofstad, Nonstoichiometry, Diffusion, and Electrical Conductivity in Binary Metal Oxides, Wiley-Interscience, NY, 1972, pp. 137-152.

25. E.D. Hondros and M.P. Seah, "The Theory of Grain Boundary Segregation in Terms of Surface Adsorption Analogues," *Met. Trans.* 8A, 1363-1371 (1977).

26. P. Wynblatt and R.C. Ku, "Surface Segregation in Alloys," pp. 115-136 in Interfacial Segregation, Eds. W.C. Johnson and J.M. Blakely, ASM, Metals Park, OH, 1979.

27. C.R. Helms, "Segregation Effects in Small Particles Used in Catalysis," pp. 175-190 in Interfacial Segregation, Eds. W.C. Johnson and J.M. Blakely, ASM, Metals Park, OH, 1979.

28. P.W. Tasker, E.A. Colbourn, and W.C. Mackrodt, "Segregation of Isovalent Impurity Cations at the Surfaces of MgO and CaO," *J. Am. Ceram. Soc.* 68, 74-80 (1985).

29. M.F. Yan and W.W. Rhodes, "Effects of Solutes on the Grain Boundary Mobility of TiO_2," pp. 519-532 in Ceramic Microstructures '86: Role of Interfaces, Eds. J.A. Pask and A.G. Evans (Mat. Sci. Res. 21, Plenum Press, New York, 1987).

30. W.D. Kingery, H.K. Bowen, and D.R. Uhlmann, Introduction to Ceramics, 2nd ed., John Wiley and Sons, New York, 1976, pp. 440-443.

31. K. Hoshino, N.L. Peterson, and C.L. Wiley, "Diffusion and Point Defects in TiO_{2-x}," *J. Phys. Chem. Solids* 46, 1397-1411 (1985).

Chapter 5

1. H. Hahn, R.S. Averback, H.J. Höfler, and J. Logas, "Sintering and Deformation of Nanocrystalline Ceramics," pp. 569-580 in Clusters and Cluster-Assembled Materials, eds. R.S. Averback, J. Bernholc, D.L. Nelson (Mat. Res. Soc. Symp. Proc. 206, Materials Research Society, Pittsburgh, PA, 1991).

2. K. Lu, "Grain Growth Processes in Nanocrystalline Materials Studied by Differential Scanning Calorimetry," *Scripta Metall.* 25, 2047-2052 (1991).

3. P. Knauth, A. Charaï, and P. Gas, "Grain Growth of Pure Nickel and of a Ni-Si Solid Solution Studied by Differential Scanning Calorimetry on Nanometer-Sized Crystals," *Scripta Metall.* **28**, 325-330 (1993).

4. J. Weissmüller, W. Krauss, T. Haubold, R. Birringer, and H. Gleiter, "Atomic Structure and Thermal Stability of Nanostructured Y-Fe Alloys," *Nanostructured Materials* **1**, 439-447 (1992).

5. T. Haubold, "EXAFS Studies of Bismuth Doped Nanocrystalline Copper," *Acta Metall.* **41**, 1769-1772 (1993).

6. J. Eckert, J.C. Holzer, and W.L. Johnson, "Thermal stability and grain growth of mechanically alloyed nanocrystalline Fe-Cu alloys," *J. Appl. Phys.* **73**, 131-141 (1993).

7. A.M. El-Sherik, K. Boylan, U, Erb, G. Palumbo, and K.T. Aust, "Grain Growth Behavior of Nanocrystalline Nickel," pp. 727-732 in Structure and Properties of Interfaces in Materials, Eds. W.A.T. Clark, U. Dahmen, C.L. Briant (Mat. Res. Soc. Symp. Proc. **238**, Materials Research Society, Pittsburgh, PA, 1992).

8. K. Boylan, D. Ostrander, U. Erb, G. Palumbo, and K.T. Aust, "An In-Situ TEM Study of the Thermal Stability of Nanocrystalline Ni-P," *Scripta Metall.* **25**, 2711-2716 (1991).

9. G. Palumbo, S.J. Thorpe, and K.T. Aust, "On the Contribution of Triple Junctions to the Structure and Properties of Nanocrystalline Materials," *Scripta Metall.* **24**, 1347-1350 (1990).

10. A.V. Galina, V.YE. Fradkov, and L.S. Shvindlerman, "Influence of Mobility of Triple Grain Junctions on Boundary Migration," *Phys. Met. Metall.* **63**, 165-168 (1987).

11. K. Lu, R. Lück, and B. Predel, "The Interfacial Excess Energy in Nanocrystalline Ni-P Materials with Different Grain Sizes," to be published in *Scripta Metall.*

12. L.-C. Chen and F. Spaepen, "Analysis of Calorimetric Measurements of Grain Growth," *J. Appl. Phys.* **69**, 679-688 (1991).

13. R.W. Siegel, S. Ramasamy, H. Hahn, L. Zongquan, L. Ting, and R. Gronsky, "Synthesis, characterization, and properties of nanophase TiO_2," *J. Mater. Res.* **3**, 1367-1372 (1988).

14. H.J. Höfler and R.S. Averback, "Grain Growth in Nanocrystalline TiO_2 and Its Relation to Vickers Hardness and Fracture Toughness," *Scripta Metall.* **24**, 2401-2406 (1990).

15. M.I. Mendelson, "Average Grain Size in Polycrystalline Ceramics," *J. Am. Ceram. Soc.* **52**, 443-446 (1969).

16. J.C. Parker and R.W. Siegel, "Calibration of the Raman Spectrum to the Oxygen Stoichiometry of Nanophase TiO_2," *Appl. Phys. Lett.* **57**, 943-945 (1990).

17. D.D. Beck and R.W. Siegel, "The dissociative adsorption of hydrogen sulfide over nanophase titanium dioxide," *J. Mater. Res.* **7**. 2840 (1992).

18. H.E. Kissinger, "Reaction Kinetics in Differential Thermal Analysis," *Anal. Chem.* **29**, 1702-1706 (1957).

19. K. Hoshino, N.L. Peterson, and C.L. Wiley, "Diffusion and Point Defects in TiO_{2-x}," *J. Phys. Chem. Solids* **46**, 1397-1411 (1985).

20. M. Arita, M. Hosoya, M. Kobayashi, and M. Someno, "Depth Profile Measurement by Secondary Ion Mass Spectrometry for Determining the Tracer Diffusivity of Oxygen in Rutile," *J. Am. Ceram. Soc.* **62**, 443-446 (1979).

21. D.J. Derry, D.G. Lees, and J.M. Calvert, "A Study of Oxygen Self-Diffusion in the C-Direction of Rutile Using a Nuclear Technique," *J. Phys. Chem. Solids* **42**, 57-64 (1981).

22. J.W. Cahn, "The Impurity Drag Effect in Grain Boundary Motion," *Acta Metall.* **10**, 789-798 (1962).

23. K.T. Aust and J.W. Rutter, "Temperature Dependence of Grain Migration in High-Purity Lead Containing Small Additions of Tin," *Trans. AIME* **215**, 820-831 (1959).

24. R.J. Brook, "The Impurity-Drag Effect and Grain Growth Kinetics," *Scripta Metall.* **2**, 375-378 (1968).

Appendix A

1. J.A.S. Ikeda, Y.-M. Chiang, A.J. Garratt-Reed, and J.B. VanderSande, "Space Charge Segregation at Grain Boundaries in Titanium Dioxide: II. Model Experiments," accepted for publication in *J. Am. Ceram. Soc.*

2. J.A.S. Ikeda, Y.-M. Chiang, and A.J. Garratt-Reed, "Quantification of Grain Boundary Segregation in TiO_2 by STEM," to appear in the Proceedings of the XIII International Conference on X-ray Optics and Microanalysis, Manchester, U.K., August 31-September 4, 1992.

3. J.A.S. Ikeda, Ph.D. Thesis, Massachusetts Institute of Technology, June 1992.

4. W. Furdanowicz, Ph.D. Thesis, Massachusetts Institute of Technology, February 1991.

5. P.R. Bevington and D.K. Robinson, Data Reduction and Error Analysis for the Physical Sciences, 2nd ed. (NY: McGraw-Hill, 1992), pp. 41-50.

126

6. J.I. Goldstein, "Principles of Thin Film X-ray Microanalysis," pp. 83-120 in Introduction to Analytical Electron Microscopy, Eds. J.J. Hren, J.I. Goldstein, and D.C. Joy (Plenum Press, NY, 1979).

Appendix B

1. J.A.S. Ikeda, Ph.D. Thesis, Massachusetts Institute of Technology, June 1992.

2. R.D. Shannon and J.A. Pask, "Kinetics of the Anatase-Rutile Transformation," *J. Am. Ceram. Soc.* **48**, 391-398 (1965).

3. Y. Iida and S. Ozaki, "Grain Growth and Phase Transformation of Titanium Oxide During Calcination," *J. Am. Ceram. Soc.* **44**, 120-127 (1961).

4. E.F. Heald and C.W. Weiss, "Kinetics and Mechanism of the Anatase/Rutile Transformation, As Catalyzed by Ferric Oxide and Reducing Conditions," *Amer. Mineral.* **57**, 10-23 (1972).

5. R.D. Shannon, "Phase Transformation Studies in TiO_2 Supporting Different Defect Mechanisms in Vacuum-Reduced and Hydrogen-Reduced Rutile," *J. Appl. Phys.* **35**, 3414-3416 (1964).

6. K.J.D. MacKenzie, "The Calcination of Titania: VI. The Effect of Reaction Atmosphere and Electric Fields on the Anatase-Rutile Transformation," *Trans. J. Brit. Ceram. Soc.* **74**, 121-125 (1975).

7. C.N.R. Rao, A. Turner, and J.M. Honig, "Some Observations Concerning the Effect of Impurities on the Anatase-Rutile Transition," *J. Phys. Chem. Solids* **11**, 173-175 (1959).

8. J.A. Gamboa and D.M. Pasquevich, "Effect of Chlorine Atmosphere on the Anatase-Rutile Transformation," *J .Am. Ceram. Soc.* **75**, 2934-2938 (1992).

9. R.A. Spurr and H. Myers, "Quantitative Analysis of Anatase-Rutile Mixtures with an X-ray Diffractometer," *Anal. Chem.* **29**, 760-762 (1957).

10. S. Wilska, "An X-ray Diffraction Study to Determine the Effect of the Method of Preparation Upon the Crystal Structure of TiO_2," *Acta Chem. Scand.* **8**, 1796-1801 (1954).

11. H.B. Weiser and W.O. Milligan, "X-ray Studies on the Hydrous Oxides. IV Titanium Dioxide," *J. Phys. Chem.* **38**, 513-519 (1934).

12. H.B. Weiser, W.O. Milligan, and E.L. Cook, "X-ray Studies on the Hydrous Oxides. X Anatase and Rutile Modifications of Titania," *J. Phys. Chem.* **45**, 1227-1234 (1941).

13. P. Jackson and G.D. Parfitt, "Infra-red Study of the Surface Properties of Rutile-- Water and Surface Hydroxyl Species," *Trans. Farad. Soc.* **67**, 2469-2483 (1971).

14. M. Ciftcioglu and M.J. Mayo, "Processing of Nanocrystalline Ceramics," pp. 77-86 in Superplasticity in Metals, Ceramics, and Intermetallics, Eds. M.J. Mayo, M. Kobayashi, J. Wadsworth (Mat. Res. Soc. Symp. Proc. 196, 1990).

APPENDIX A

Errors Associated with the Measurement of Excess Solute Density

Error in the quantitative STEM measurement of excess solute density at grain boundaries is due primarily to counting statistics. Possible errors due to x-ray absorption are also briefly discussed. A more detailed analysis of each of these issues appears in references 1,2, and 3.

Standard Error due to Counting Statistics

Furdanowicz has calculated the standard deviation due to propagation of errors when composition is computed as a fraction of the total:[4]

$$S_i = \frac{\sqrt{c_i^2\left(\delta_j^2 + \delta_k^2\right) + \delta_i^2\left(c_j + c_k\right)^2}}{\left(c_i + c_j + c_k\right)^2} \tag{A1}$$

where $c_i = I_i k_{Ti}^i / A_i$ and $\delta_i = I_i^c k_{Ti}^i / A_i$.

S_i is the standard deviation in mole fraction for element i (Ca or Sn), I_i is the integrated peak intensity for characteristic emission for element i, I_i^c is the standard error in I_i, k_{Ti}^i is the "k-factor" for element i, and A_i is its atomic weight. The standard deviation associated with each measurement of excess solute density Γ (see Equation 4-5 in section 4.2.3) is then:[5]

$$S_i^\Gamma = N \cdot w \cdot \sqrt{\left(S_i^{gb}\right)^2 + \tfrac{1}{4}\left[\left(S_i^{g1}\right)^2 + \left(S_i^{g2}\right)^2\right]}$$

where i is Ca or Sn, S_i^{gb} is the standard deviation in composition of i at the grain boundary from equation A1, S_i^{g1} and S_i^{g2} are the standard deviations in composition of i in each of the neighboring grains, N is the cation site density of rutile, and w is the width of the reduced area scan.

129

The results of this error analysis are shown in Figures A1-A6, where the error bars indicate the 95% confidence level ($\pm 2S_i^{\Gamma}$) for each measurement of Γ. With the exception of two data believed to be from "special" boundaries (data point 6 in Fig. A5 and data point 3 in Fig. A6), the variation in Γ between grain boundaries within the same sample is statistically insignificant. However, the trend of an increasing solute density with grain size *is* statistically significant.

Errors due to X-ray Absorption

Errors in quantitative x-ray microanalysis due to absorption of x-rays in thick samples or in samples with large variations in thickness or composition can be corrected for, in the Cliff-Lorimer equation (Eq. 4-3 in section 4.2.3), by a multiplying factor:[6]

$$\frac{f(\chi_i)}{f(\chi_{Ti})} = \left[\frac{1 - \exp\left(\frac{-\mu}{\rho} \Big|_{TiO_2}^{Ti} \cdot \csc\alpha \cdot \rho t \right)}{1 - \exp\left(\frac{-\mu}{\rho} \Big|_{TiO_2}^{i} \cdot \csc\alpha \cdot \rho t \right)} \right] \cdot \left[\frac{\frac{\mu}{\rho} \Big|_{TiO_2}^{i}}{\frac{\mu}{\rho} \Big|_{TiO_2}^{Ti}} \right] \tag{A3}$$

where α is the detector takeoff angle ($12°$), ρ is the sample density, t is the foil thickness, and $(\mu/\rho|_{TiO_2}^{i}$ is the overall mass absorption coefficient (cm^2/g) for element i in TiO_2, calculated from elemental mass absorption coefficients:

$$\frac{\mu}{\rho} \Big|_{TiO_2}^{i} = \frac{\mu}{\rho} \Big|_{Ti}^{i} \cdot X_{Ti} + \frac{\mu}{\rho} \Big|_{O}^{i} \cdot X_O \tag{A4}$$

where $(\mu/\rho|_{Ti}^{i}$ is the mass absorption coefficient of Ti for the i line (in our case, either CaKα, SnLα, or TiKα) and X is the weight fraction of titanium or oxygen in TiO_2.

In sufficiently thin samples absorption corrections are not necessary. The "thin film criterion" is often applied, which states that below a particular foil

thickness, absorption is negligible in that it will not alter the true ratio of I_A/I_B more

than 5-10%.[6] This criterion for two elements A and B is:

$$t < \frac{0.2}{\left(\Delta\left.\frac{\mu}{\rho}\right|_{TiO_2}\right)\csc\alpha\cdot\rho} \tag{A5}$$

where $\Delta\mu\left./\rho\right|_{TiO_2}$ is the difference in mass absorption coefficients for elements A

and B in TiO_2.

Applying Eq. A5 to the worst case (largest differential absorption) of the

elements Sn ($\mu\left./\rho\right|_{TiO_2}^{SnL_\alpha}\approx194$ cm^2/g) and Ti ($\mu\left./\rho\right|_{TiO_2}^{TiK_\alpha}\approx90$ cm^2/g), a thin film limit

of 9430 Å is calculated for x-ray analysis of cations in this material system. This

thickness is well above the electron transparency limit for 100 kV electrons. Thus,

errors due to x-ray absorption are negligible in comparison to the error from

counting statistics.
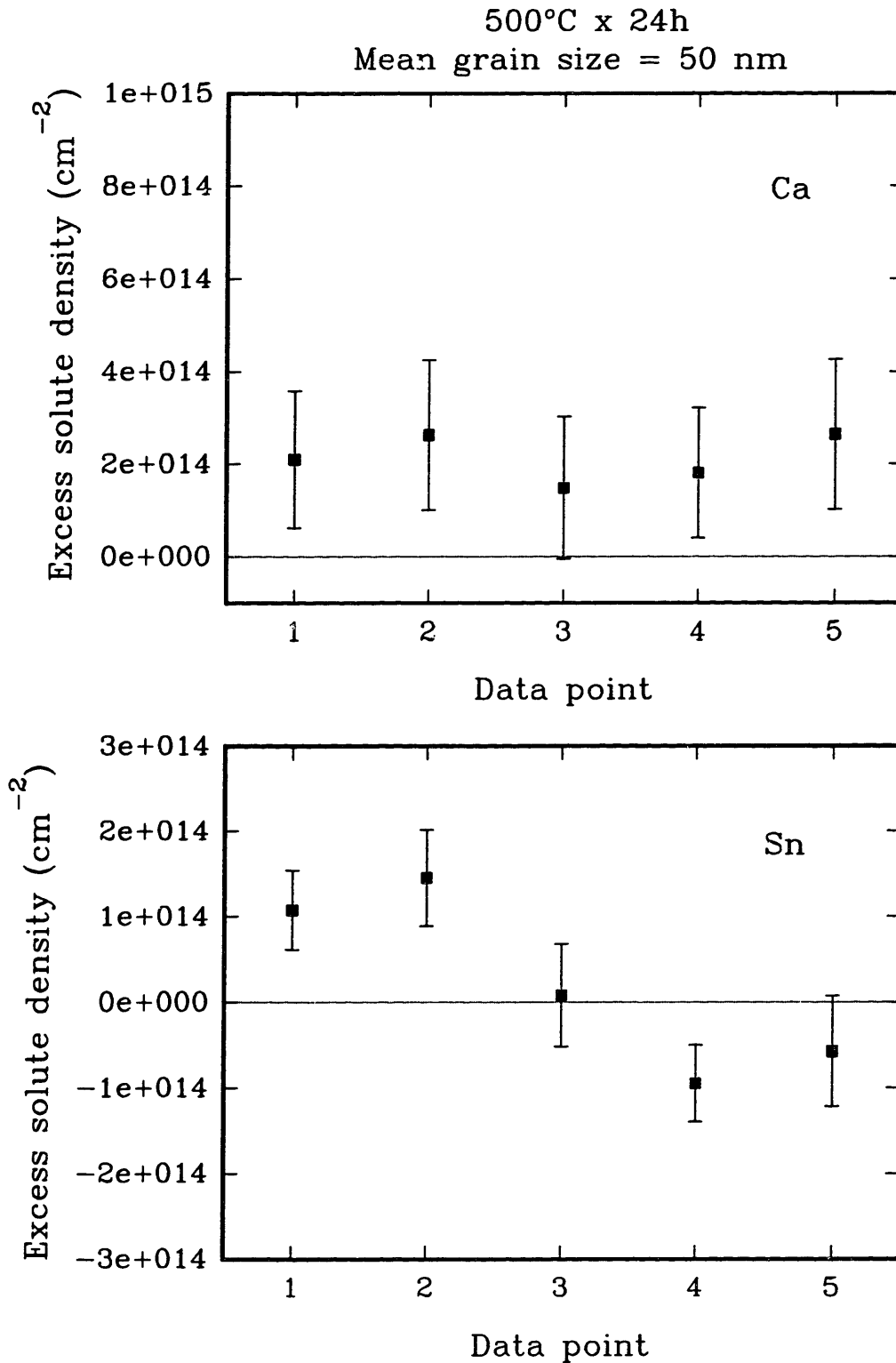
Figure A1. Measurement of excess calcium and tin density at five grain boundaries in TiO_2 with a mean grain size of 51 nm. Error bars indicate a 95% confidence level.
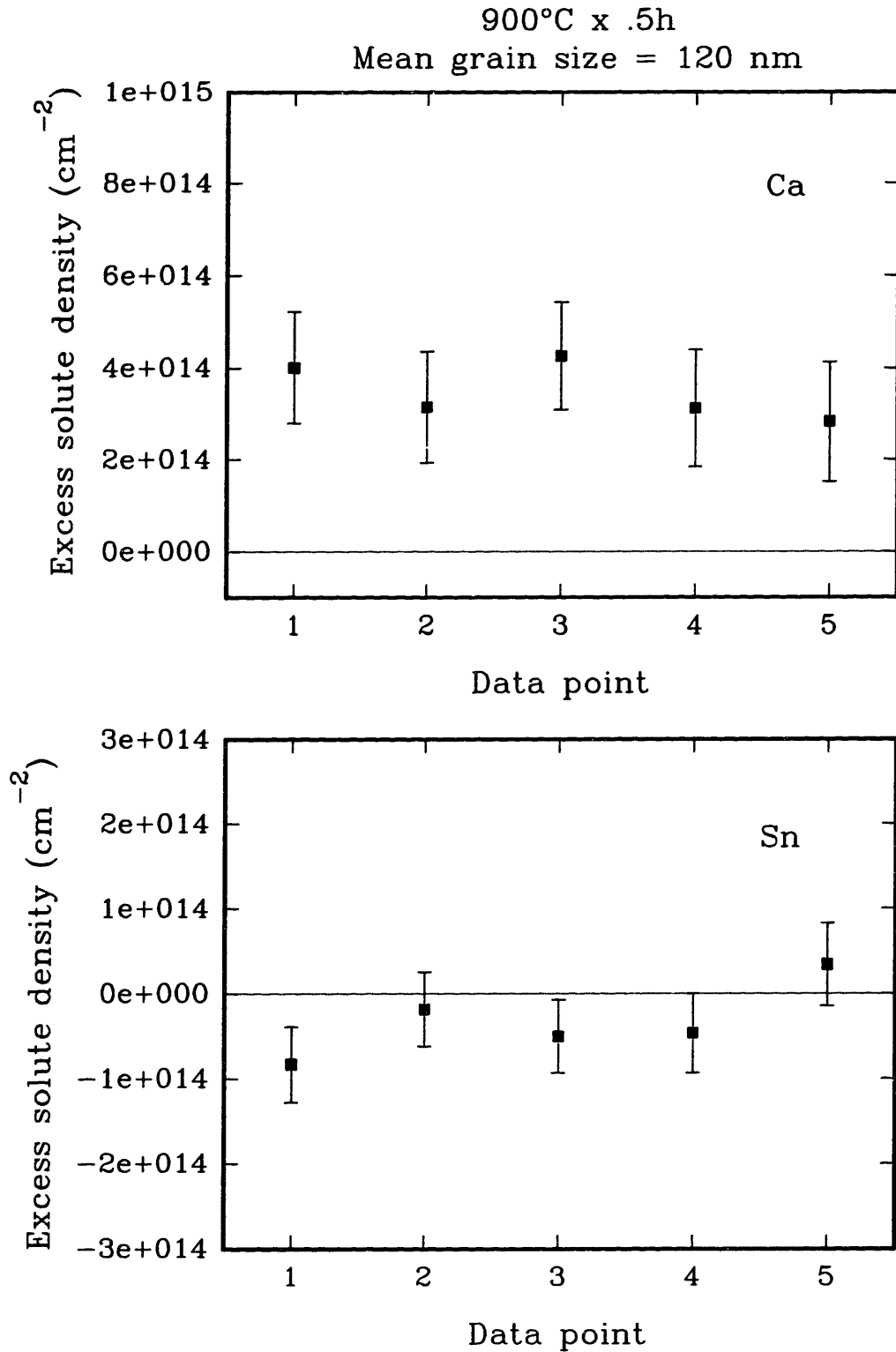
Figure A2. Measurement of excess calcium and tin density at five grain boundaries in TiO_2 with a mean grain size of 120 nm. Error bars indicate a 95% confidence level.
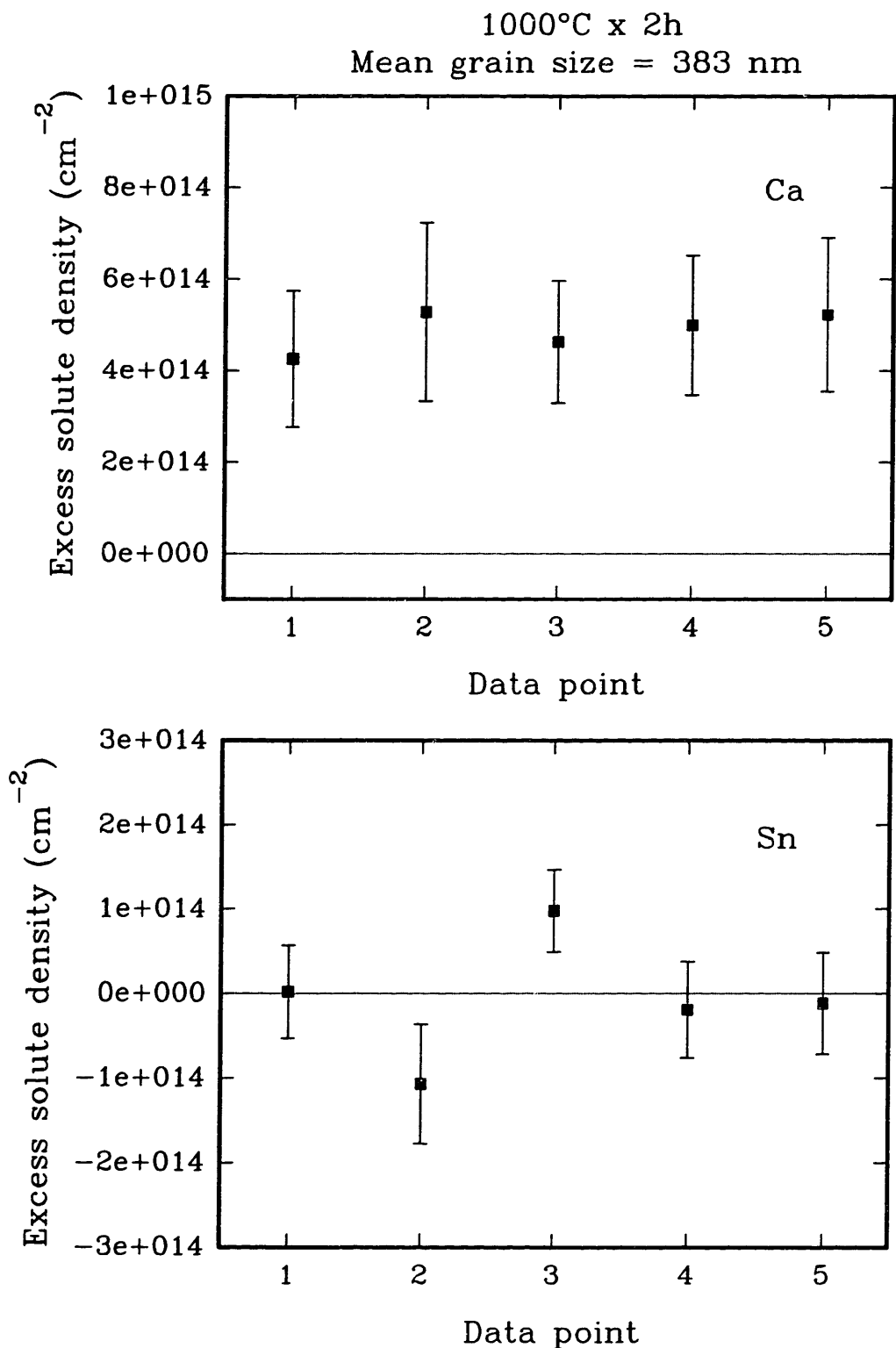
Figure A3. Measurement of excess calcium and tin density at five grain boundaries in TiO_2 with a mean grain size of 383 nm. Error bars indicate a 95% confidence level.

Figure A4. Measurement of excess calcium and tin density at six grain boundaries in TiO_2 with a mean grain size of 477 nm. Error bars indicate a 95% confidence level.

Figure A5. Measurement of excess calcium and tin density at six grain boundaries in TiO_2 with a mean grain size of 509 nm. Error bars indicate a 95% confidence level.
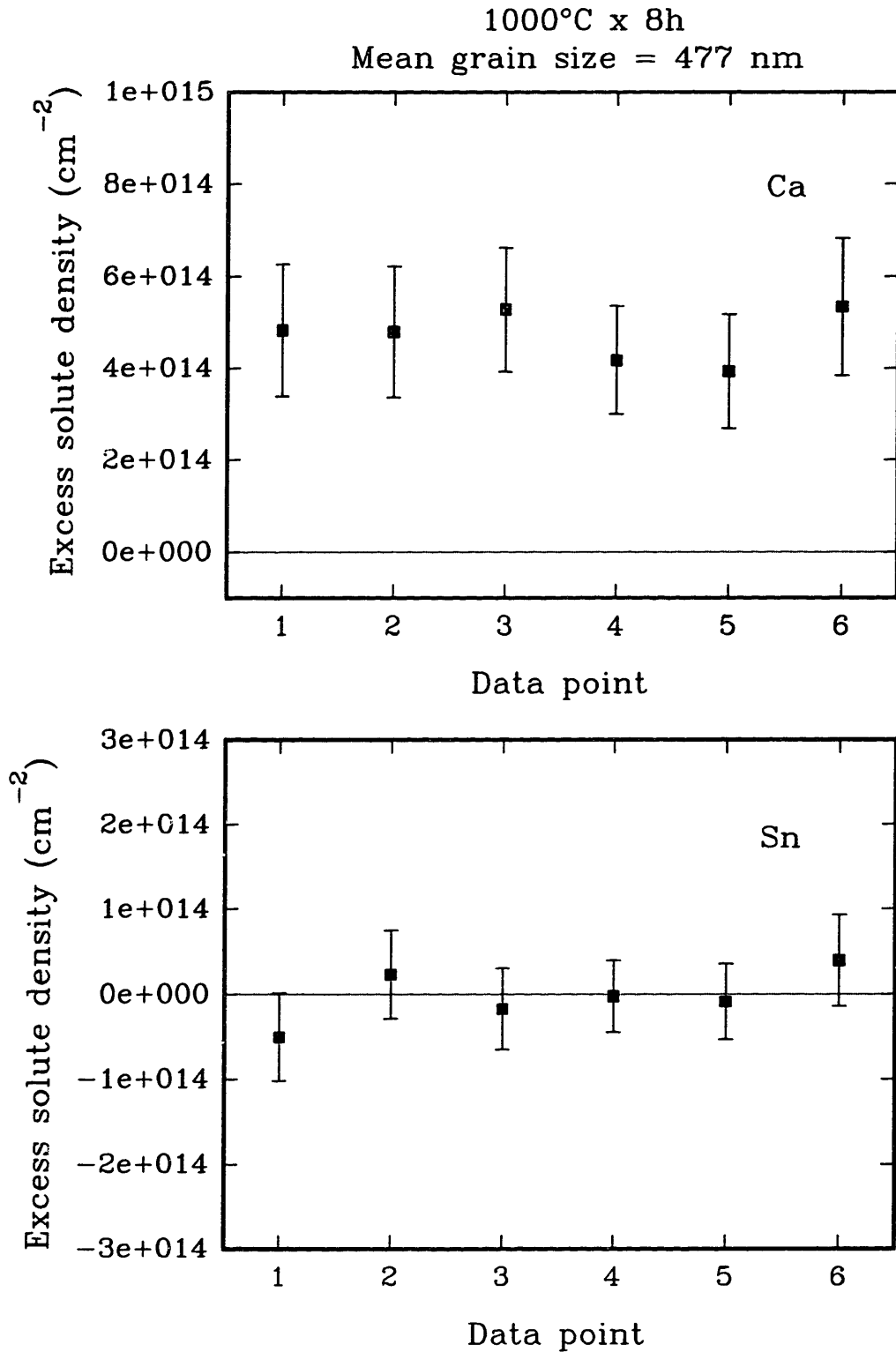
Figure A6. Measurement of excess calcium and tin density at five grain boundaries in TiO_2 with a mean grain size of 731 nm. Error bars indicate a 95% confidence level.
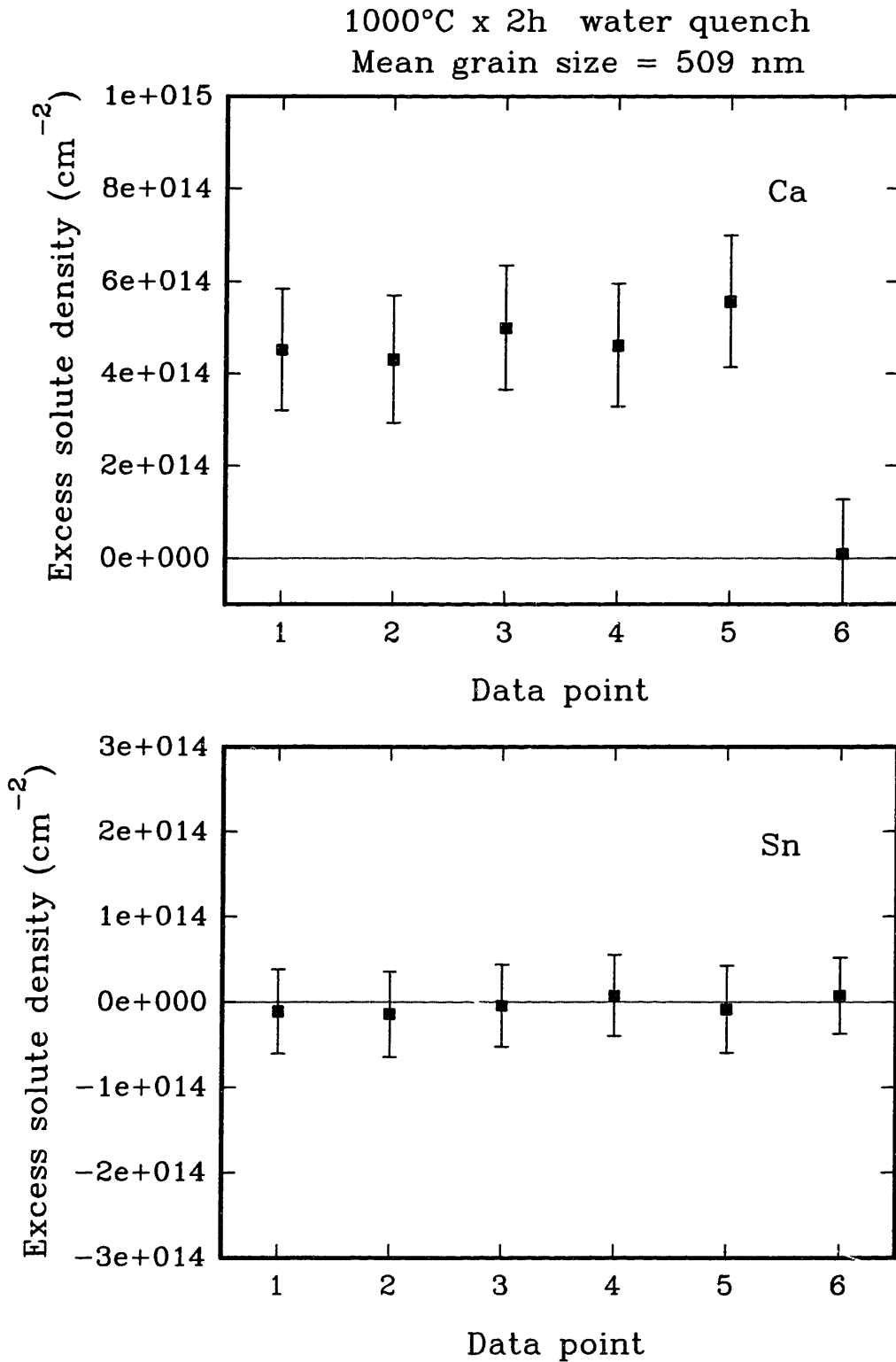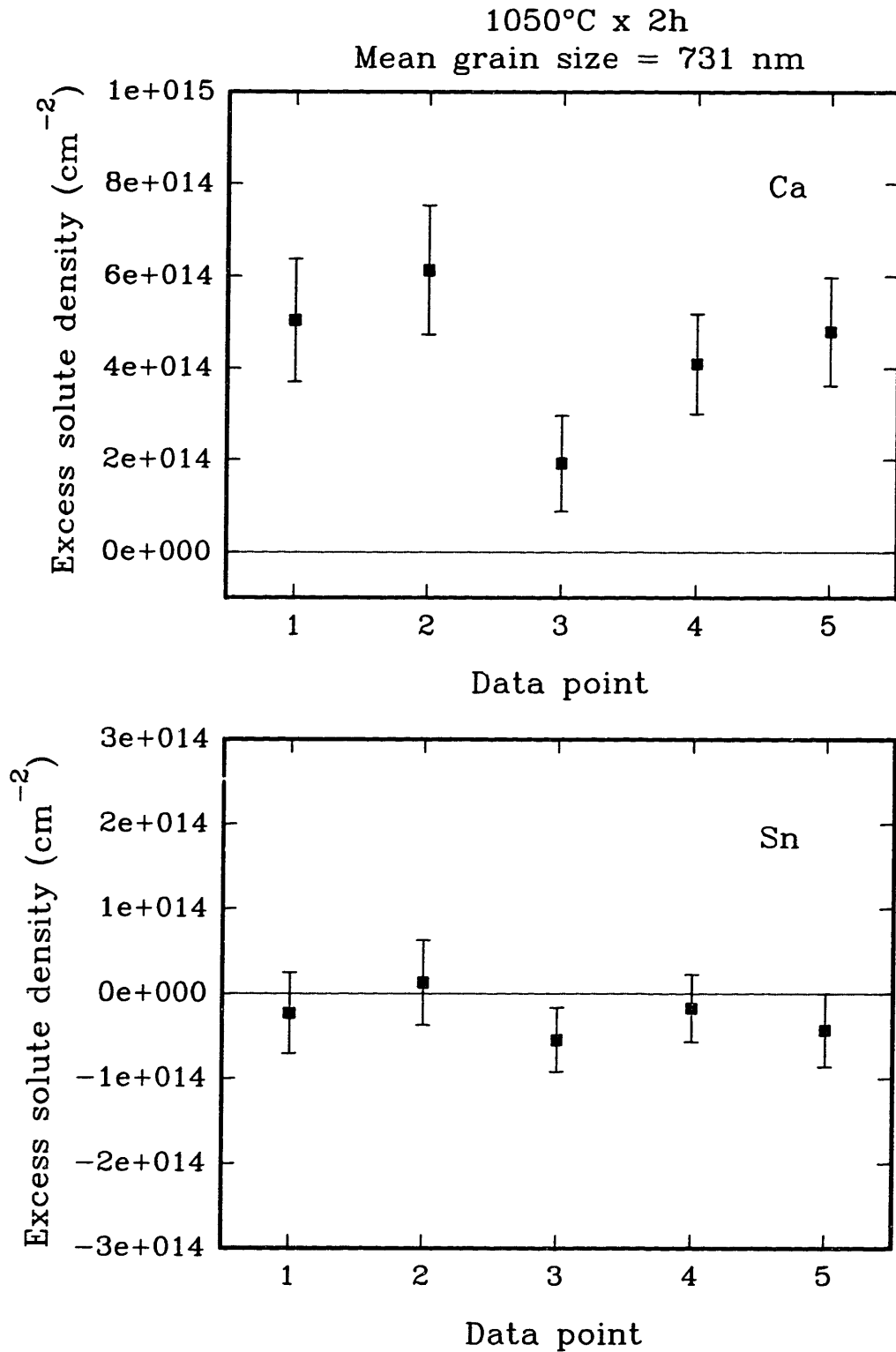
APPENDIX B

Observations on the Effect of Dopants and Preparation Method
on the Anatase-Rutile Phase Transformation

As it became apparent that physically-derived nanocrystalline TiO_2 was not suitable for calorimetric measurement of excess grain boundary properties, much effort was diverted into working with a solution chemical method that had been used in our laboratory for several years to synthesize TiO_2 powders homogeneously doped with Al and Nb.[1] Preliminary experiments showed that these powders (in particular, a batch doped with ~0.2 mole% Nb) could be hot pressed into dense pellets with an average grain size between 30 to 50 nm. However, these pellets contained both the anatase and rutile phases. Modifications in the calcining treatment of the Nb-doped powder (higher temperature, reducing atmosphere) resulted in modest increases in the rutile content of the powders, but always with a concomitant increase in the particle size. It seemed obvious that further improvements could be made only by making changes in the dopant chemistry or processing methodology.

The effects of various impurities and atmospheres on the anatase-rutile transformation have been reported rather extensively in the literature. A review by Shannon and Pask[2] summarizes the work of many researchers and offers the hypothesis that the effect of a particular dopant or atmosphere hinges on whether its introduction is accompanied by the creation of oxygen vacancies. Since the transformation involves a shrinkage or collapse of the oxygen sublattice in anatase and cooperative rearrangement of Ti^{4+} and O^{2-} ions, oxygen vacancies would provide additional space for this collapse to occur, whereas intersititals would be a barrier. Additions of CuO,[2,3] Fe_2O_3,[3,4] NiO, CoO, and MnO_2[3] have been reported to promote the anatase-rutile transformation. These are all acceptor

dopants and might be expected to substitute for Ti^{4+} ions with the creation of oxygen vacancies for electroneutrality. Similarly, reducing atmospheres have been observed to accelerate the transformation,[2-6] again by the introduction of oxygen vacancies or perhaps by reduction to a Ti_nO_{2n-1} Magneli phase which could act as a nucleation agent.[2] The presence of S^{6+}, W^{6+}, or P^{5+} ions inhibits the transformation,[2,3,7] as might be expected since substitution for Ti^{4+} would reduce the number of oxygen vacancies.

The effect of dopants is still not entirely clear, however. Rao and coworkers reported that Zn^{2+} and Al^{3+} ions, both acceptors, stabilize the anatase structure.[7] Rao also reported that Cl^- impurities stabilize anatase, whereas Gamboa and Pasquevich found that a Cl_2 atmosphere or to a lesser extent, adsorbed Cl^-, greatly accelerates the phase transformation.[8] One reason for the confusion is that none of these studies on the effect of dopants on the phase transformation has been accompanied by experiments (or even much discussion) to shed light on how they are incorporated into the structure. In addition, some of the contradictions about the effect of dopants on the transformation may be rooted in the observation of Iida and Ozaki that the method of preparation plays an important role in the transformation.[3] In their work, the transformation temperature during calcination seemed to correlate with the "crystallinity" of the prepared titanium hydroxide. Titanium hydroxide that was well crystallized had the highest transformation temperature, whereas poorly crystallized hydroxide had the lowest.

Effect of Dopants

The x-ray diffraction patterns shown in Figure B-1 illustrate the effect of Sn, Ca, Al, and Nb dopants on the phase content of TiO_2 powders after a 600°C x 1 hour calcining treatment. It should be noted that a strict comparison can be made
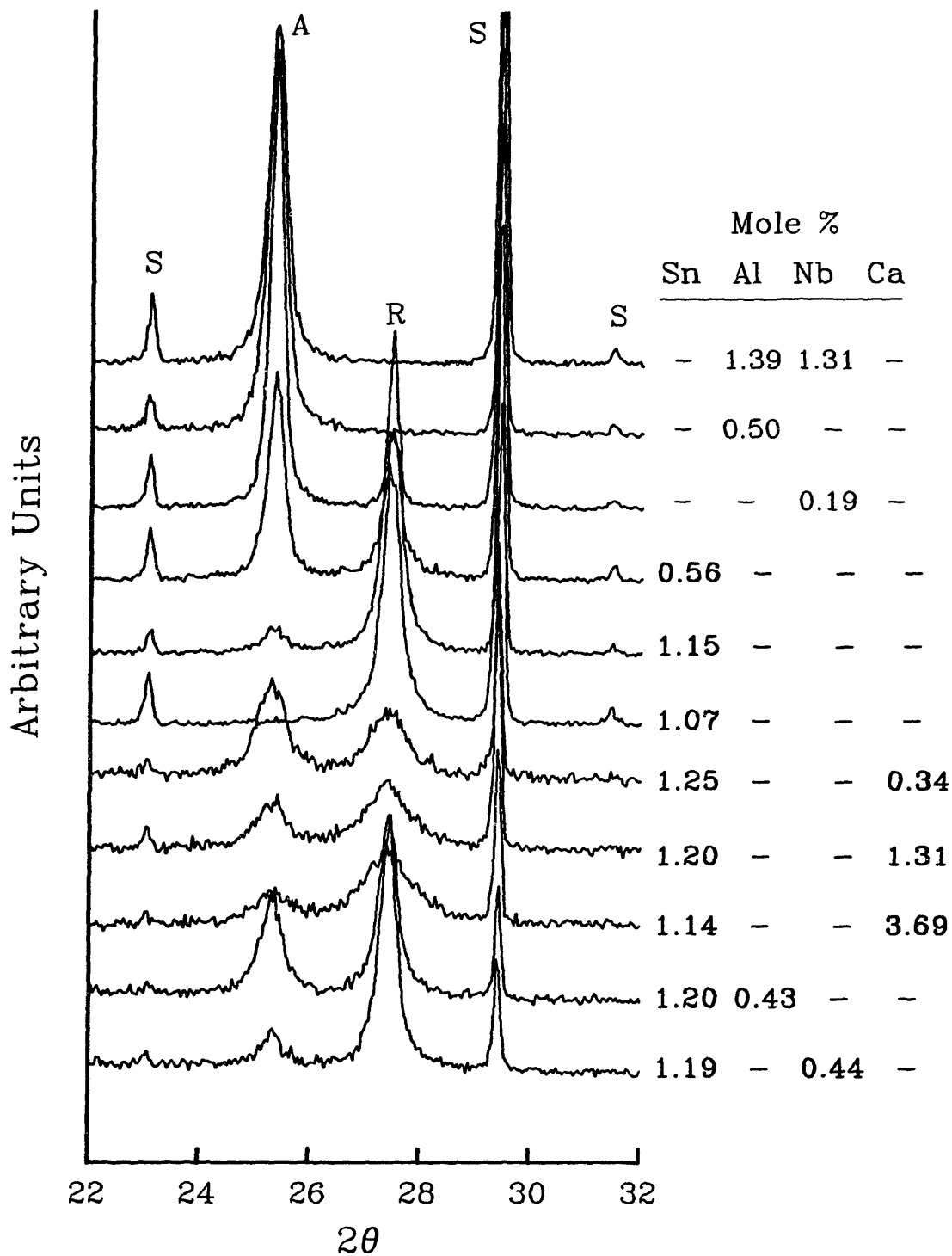
Figure B-1. Powder x-ray diffraction patterns of doped TiO_2 powders given a 600°C x 1 hour calcination in static air. (R) indicates the (110) rutile reflection, (A) indicates the (101) anatase reflection, and (S) the reflection of the internal standard.

only for those powder batches shown in bold print, since they were all synthesized using my own "baseline" method (described in section 2.2.1). The other batches were synthesized by colleagues in my research group using, nominally, the same process; however, details of solution formation, precipitation, washing, and freeze drying may differ enough to affect phase content and particle size.

Table B.1 summarizes weight % rutile and crystallite size of these same calcined powders. Phase content was quantified using the ratio of the rutile (110) and anatase (101) peak intensities and the calibration formula given in reference 9. Crystallite size was estimated using the Scherrer equation, after correcting for instrumental broadening using the line width of a coarse internal standard. It can be seen that Sn, particularly at the level of ~ 1 mole %, is quite effective in

TABLE B.1 Effect of dopants on phase development and particle size of chemically-derived powders.

| Batch | Mole % (ICP) | | | | 600°C x 1 hour calcine | |
	Sn	Ca	Al	Nb	Weight % Rutile	Particle size (nm)
S1	0.56	-	-	-	49	30
S2	1.15	-	-	-	89	26
SC3	1.25	0.34	-	-	48	12
SC1	1.20	1.31	-	-	63	9
SC2	1.14	3.69	-	-	75	8
TSA1	1.20	-	0.43	-	72	23
TSN1	1.19	-	-	0.44	84	25
T1	-	-	1.39	1.31	0	23
T2	-	-	0.50	-	0	24
T3	-	-	1.32	1.43	0	20
0.1 Nb	-	-	-	0.19	19	33

Note: Gray area indicates powder batches that were prepared using the identical "baseline" method. Remaining batches were prepared by other researchers.

accelerating the formation of rutile. Powder batches with no Sn developed from zero to ~20 weight % rutile during this calcining treatment. Dr. Howard Jacobsen of E.I. DuPont de Nemours suggested the addition of Sn. With the benefit of hindsight, tin is a natural candidate to promote the transformation since SnO_2 is isostructural with rutile and does not have an anatase analogue.

The addition of Al, Nb, or Ca on top of Sn lessens tin's effectiveness in promoting the phase transformation. Of these three, calcium had the largest retarding effect on the phase transformation, perhaps because of its comparatively large ionic radius. Calcium was also quite effective as a barrier to grain coarsening. Comparison of batches TSA1 and TSN1 show that, in our case, Al doping inhibits the phase transformation more than niobium doping. If both are incorporated substitutionally into the titanium sublattice, the interpretation of the phase transformation by Shannon and Pask[2] suggests that Al-doping should promote the transformation since oxygen vacancies must be introduced for charge compensation. Possible explanations for this discrepancy are that their interpretation is incorrect or, more likely, that at least at the relatively low calcination temperature of 600°C, the solubility of aluminum in TiO_2 is minimal, and thus it is not incorporated substitutionally. (Therefore, it might be segregated at free surfaces and interfaces or, less likely, incorporated into the lattice as interstitials.) Comparison of batches S2 and TSN1 shows that niobium has only a very small deleterious effect on the phase transformation.

The preceding discussion is, of course, based on the phase transformation during only one heat treatment (600°C x 1 hour). For example, of the three calcium-doped batches, the one with the least calcium (SC3) had the lowest rutile content after the 600°C x 1 hour calcine, yet it required the shortest time at 750°C to transform almost completely to rutile (1 hour versus 4 hours for batch SC1). A

142

real understanding about the effect of these dopants would require a kinetic analysis of the transformation as well as analysis of the surface versus bulk chemistry of the developing powders.

Effect of Preparation Method

The literature contains some guidance, albeit mostly anecdotal, about the effect of preparation method on the phase of TiO_2.[3,10-12] As was already mentioned, Iida and Ozaki found that when titanium hydroxide is the precursor to TiO_2, its crystallinity has a large effect on the onset of the phase transformation.[3] It is well known that TiO_2 produced by precipitation of titanium sulfate solutions is usually anatase that is stable up to 800°C, presumably because of the presence of residual sulfate ions.

Three alternative preparation methods were attempted in this work, and the results are summarized in Table B.2. In the first, the only step that was changed from the "baseline" method was the rate of addition of the NH_4OH. Rather than adding at the controlled rate of a burette ($t \sim 30$ sec), an amount calculated to bring the solution to its equivalence point was added rapidly to the $TiCl_4$ solution ($t < 3$ sec). The idea here was to "shock" supersaturate the solution so that many more nuclei would be formed prior to the onset of growth. This batch was called "S3," and as can be seen in Table B.2, this powder did contain more rutile and with a finer particle size than the powder produced using the baseline method (batch S2). Use of x-ray diffraction at increments in the calcining treatment indicated that, although anatase was the first phase to nucleate in both batches, rutile began to form in the S3 batch about 100°C earlier. However, it is not at all likely that this success was due to the intended "shock nucleation" effect; qualitative observations suggest that the rapid addition of NH_4OH changed the surface chemistry of the solution.

TABLE B.2. Effect of Preparation Method on Phase Development and Particle Size of Chemically-Derived TiO_2 Powders.

Batch	Preparation Method	Mole% SnO_2	ppm Cl^-	Phase Development	600°C x 1 hr calcine		Comments
					Weight% Rutile	Particle size (nm)	
S2	Baseline	1.15	32	Anatase. Rutile begins by ~400°C	89	26	pH 6 during rinsing
S3	Rapid addition of NH_4OH	1.07	258	Anatase. Rutile begins by ~300°C	100	21	pH 3-4 during rinsing. Powder has large specific volume.
S4	NaOH used instead of NH_4OH†	N.A.*	N.A.*	Direct (?) formation of rutile by 428°C	100	15	Incomplete rinsing of residual NaCl. Since NaCl does not decompose, powder likely has significant levels of Na^+ and Cl^-.
S5	Aqueous $(Ti+Sn)Cl_4$ added to deionized H_2O at ~100°C‡	N.A.*	N.A.*	N.A.	100	19	Supernatant became very cloudy after final rinse. Brown patches in freeze-dried powder. Extremely large specific volume; extremely light and fluffy powder.

*Chemical analyses not available for these batches; however, nominal compositions were intended to be the same for batches S2-S5.

†Following rough description given by Wilska (Ref. 10): "Alkaline precipitation, 10% aqueous HCl-acid solution of $TiCl_4$ added to a 20% NaOH solution. Room temp."

‡Following rough description given by Wilska (Ref. 10): "Hydrolysis by adding a 10% aqueous HCl-acid solution of $TiCl_4$ to a large volume of boiling water."

144

First, the pH of the supernatant of this batch was between 3-4 for the entire rinsing process, compared to a pH of 6-7 for the "baseline" batch S2. The supernatant was also cloudy rather than the usual clear, suggesting that more very fine particles were dispersed. Furthermore, chromatographic analysis (Union Carbide Corp., Tarrytown, NY) indicated a significantly larger residual Cl^- content in the S3 batch— 258 ppm compared to 32 ppm in the baseline S2 batch. An infra-red study of rutile surfaces has shown that a surface chloride concentration of $>\sim 150$ ppm changes the characteristic spectrum of a sample at room temperature.[13] Furthermore, in light of evidence that the anatase-rutile transformation is sensitive to both adsorbed chlorine and chlorine in the atmosphere,[8] it is possible that the higher chlorine content detected in batch S3 is the primary factor in its earlier transformation, and thus finer particle size. A more effective means of increasing the nucleation rate may be to add the cation solution to the NH_4OH solution.[14] Precipitation should be instantaneous and, for multicomponent solutions, atomic-scale mixing should be more closely approached since the solubility limit of both components would be exceeded at the same time.

The second alternative preparation method was to use NaOH as the precipitant rather than NH_4OH, following a rough description given by Wilska[10] who reported that TiO_2 prepared by this method contained 72% rutile and 28% anatase after 1 hour at 300°C. Figure B-2 shows x-ray diffraction patterns at increments in the calcination of our powder batch S4 which was prepared by this method. It can be seen that by 428°C, either rutile nucleates so rapidly on the first-formed anatase as to make detection of anatase difficult, or rutile forms directly from the amorphous phase. Table B.2 shows that this batch of powder was entirely rutile with a crystallite size of ~ 15 nm after a 600°C x 1 hour calcine. Although this batch was the best in terms of particle size and rutile content, it was not used in
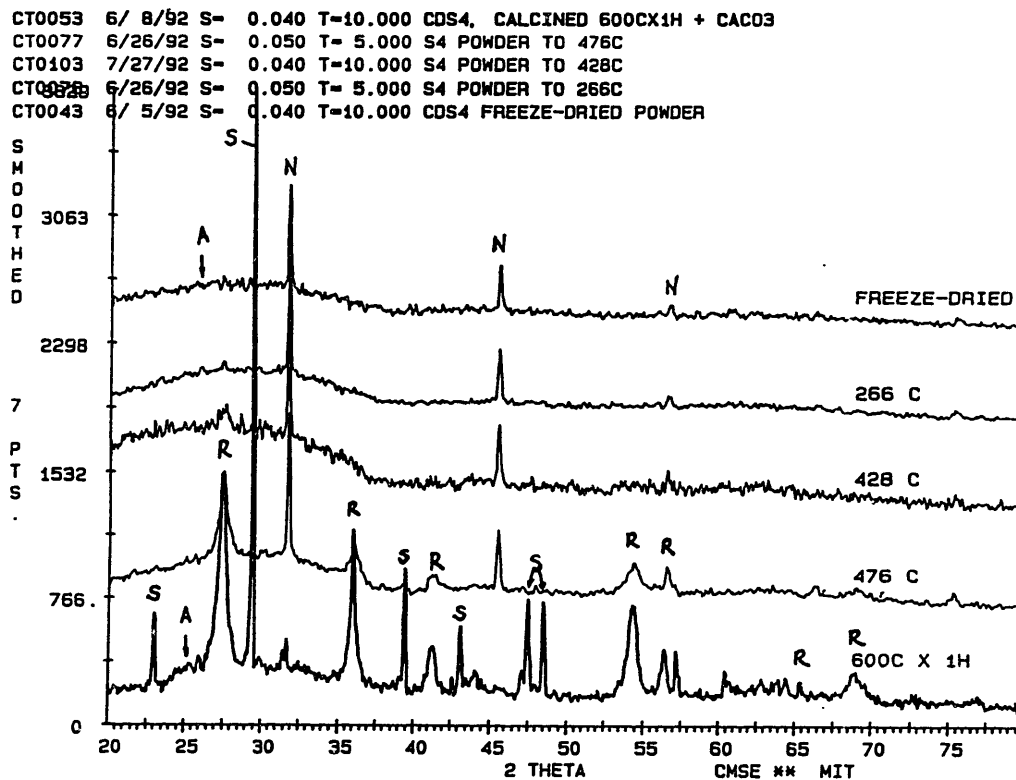
Figure B-2. Powder x-ray diffraction patterns of batch S4 at increments during calcination. Powder was heated at 10°/min to the temperature indicated and then furnace-cooled. (R) indicates rutile reflections, (A) anatase positions, (N) NaCl reflections, and (S) reflections of the internal standard (which was present in the 600°C x 1 hour powder only).

146

this work because of the residual NaCl that was detected by x-ray diffraction (see Figure B-2). Unlike residual NH_4Cl that can sometimes be detected in freeze-dried baseline-prepared powders if rinsing is inadequate, NaCl does not decompose prior to melting. Therefore, this powder probably has significant amounts of Na^+ and Cl^- impurities, although this has not been confirmed by ICP. This preparation method could hold promise if the rinsing step can be improved such that NaCl is dissolved more completely unless the extremely rapid transformation is due solely to a high Cl^- content in the powder.

Wilska describes a preparation method "hydrolysis by adding a 10% aqueous HCl-acid solution to a large volume of boiling water" as producing rutile by $500°C.$[10] This was attempted as the third alternative preparation method, but was by far the least successful. Precipitation could not be detected after several hours at $\sim 100°C$. Thus, the solution was cooled slightly and 7.4 M NH_4OH was added to precipitate the solution. Although this batch at a first glance seems to be an improvement over the baseline method in terms of rutile content and crystallite size (see Table B.2), other observations indicated that it was not suitable for powder preparation. There was an aging process in which the supernatant of this batch became very cloudy after the final rinse (even though the pH was 6-7), so much so that the sediment layer in the beaker was difficult to detect. (A sol-gel process may have occurred.) There were brown patches in the freeze-dried powder, and it had such a large specific volume and was so light and fluffy that it could easily blow away in the natural air currents of our laboratory.

In summary, modifications were made in the powder preparation method that proved to be successful in producing rutile at low enough temperatures such that the particle size remained approximately ≤ 20 nm. By far the most effective change was

the addition of ~ 1 mole% SnO_2. However, the powder processing has certainly not been optimized. Further improvements can almost certainly be made after a more methodical and rigorous study of the precipitation and rinsing steps of the process.

BIOGRAPHICAL NOTE

The author was born in 1966 in Carmel, CA, second of three daughters of Sally W. (Weidlein) Demetry, a modern dance instructor and preschool teacher, and James S. Demetry, a professor of electrical engineering. In 1971 her family moved from Monterey to Holden, MA, where she attended Holden public schools and graduated from Wachusett Regional High School in 1984. An interest in the mechanical behavior of materials somehow arose during high school, where she was active in the Science Seminar program and completed now somewhat amusing projects entitled "The Strength of Ice Composites" and "The Effect of the Interfacial Bond on Plaster Composites."

She received a B.S. in Mechanical Engineering from Worcester Polytechnic Institute in 1988. Research topics there included the effect of various heat treatments on the grindability of tool steels (with Norton Co.) and high temperature deformation of Al/SiC metal matrix composites (with Alcan International). Her first exposure to ceramics came in the summer of 1987, working in MIT's Ceramics Processing Research Laboratory on the pressureless sintering of Al_2O_3/SiC whisker composites. While at WPI she was active on the crew team and as a student representative on faculty committees. She was awarded membership in Tau Beta Pi, Pi Tau Sigma, and Sigma Xi. She also met her future husband, Peter Terwilliger, and they were married in the summer of 1989.

She began work toward a Ph.D. in ceramics at MIT in the summer of 1988, in the research group of Professor Yet-Ming Chiang. She was awarded an Office of Naval Research Graduate Fellowship (1988-1991), and received the Materials Science and Engineering Department's John Wulff Award for Excellence in Teaching (1990) and a Materials Research Society Graduate Student Award (1992). She is a member of the American Ceramic Society, Materials Research Society, and American Society for Engineering Education. She is the author or co-author of 11 scientific papers.

In the fall of 1993 she will be rejoining the materials group within the Mechanical Engineering department at WPI as a tenure-track assistant professor. If a career in academia doesn't pan out, she can always start her own pie baking business. Other interests include gardening and landscaping, playing the piano, hiking, and quilting.